Long Term Stability and Permeability of Mixed Ion Conducting Membranes under Oxyfuel Conditions

Xiaoyu Li

JÜLICH
FORSCHUNGSZENTRUM

Member of the Helmholtz Association

Schriften des Forschungszentrums Jülich
Reihe Energie & Umwelt / Energy & Environment Band / Volume 194

Forschungszentrum Jülich GmbH
Institute of Energy and Climate Research (IEK)
Microstructure and Properties of Materials (IEK-2)

Long Term Stability and Permeability of Mixed Ion Conducting Membranes under Oxyfuel Conditions

Xiaoyu Li

Schriften des Forschungszentrums Jülich
Reihe Energie & Umwelt / Energy & Environment Band / Volume 194

ISSN 1866-1793 ISBN 978-3-89336-916-4

Bibliographic information published by the Deutsche Nationalbibliothek.
The Deutsche Nationalbibliothek lists this publication in the Deutsche
Nationalbibliografie; detailed bibliographic data are available in the
Internet at http://dnb.d-nb.de.

Publisher and Distributor: Forschungszentrum Jülich GmbH
Zentralbibliothek
52425 Jülich
Tel: +49 2461 61-5368
Fax: +49 2461 61-6103
Email: zb-publikation@fz-juelich.de
www.fz-juelich.de/zb

Cover Design: Grafische Medien, Forschungszentrum Jülich GmbH

Printer: Grafische Medien, Forschungszentrum Jülich GmbH

Schriften des Forschungszentrums Jülich
Reihe Energie & Umwelt / Energy & Environment, Band / Volume 194

D 82 (Diss., RWTH Aachen, University, 2013)

ISSN 1866-1793
ISBN 978-3-89336-916-4

Kurzfassung

Im Rahmen der vorliegenden Arbeit wurden die thermochemischen Eigenschaften von mischionenleitenden Membranmaterialien zur Abtrennung von Sauerstoff aus Luft untersucht. Zur Gruppe der sauerstoffdurchlässigen Membranmaterialien gehören unter anderem perowskitische Oxide, die eine auffallend hohe Permeationsleistung aufweisen. Im Rahmen der hier vorliegenden Arbeit sind umfangreiche Untersuchungen über den Abfall der Langzeitstabilität der Perowskitmembranen bei mittleren Temperaturen (500-800 °C) unternommen worden. Der Abfall der Membraneigenschaften, der durch thermodynamische Zersetzung verursacht wird, ist ein großer Nachteil für ihren Einsatz in kohlegefeuerten Kraftwerken. Außerdem müssen mischionenleitende Membranmaterialien einen relativ niedrigen Ausdehnungskoeffizient aufweisen.

Die perowskitstrukturierten Materialien $Ba_xSr_{1-x}Co_yFe_{1-y}O_{3-\delta}$ (BSCF), wobei x und y im Rahmen der Dissertation variiert wurden, sind mit Hilfe der Festköperreaktion hergestellt worden. Vor der Herstellung der gasdichten Membranen wurde das Sinterverhalten untersucht. Zur Bewertung dieser Membranmaterialien bezüglich ihres zukünftigen Einsatzpotentials wurden ihre Eigenschaften, wie Schmelztemperatur, Änderung der Sauerstoffstöchiometrie und thermisches Ausdehnungsverhalten in synthetischer Luft entsprechend experimentell bestimmt. Weiterhin wurde der Zusammenhang zwischen den thermochemischen Eigenschaften der Membranmaterialien und der Änderung der Zusammensetzungen durch Dotierungen in BSCF untersucht.

Darüber hinaus wurde die Degradation der Membranmaterialien während des Langzeitbetriebs in Oxyfuel-Prozess ähnlichen Bedingungen betrachtet. Die Variation des Sauerstoffsflusses durch BSCF Membranen unter einem Luft/He Druckgradienten wurde aufgezeichnet. Eine langsame exponentielle Abnahme des Flusses wurde bei 800 °C beobachtet, verglichen mit der stabilen Permeationsleistung der Membranen bei höheren Temperaturen. Der Grund für den Abfall der Membranpermeabilität wird hauptsächlich in der Zersetzung der kubischen Phase in hexagonale Polymorphe gesehen. Bei 850 °C wurde eine Erhöhung des gemessenen Sauerstoffflusses der $Ba_{0.4}Sr_{0.6}Co_{0.2}Fe_{0.8}O_{3-\delta}$ Membran nachgewissen, obwohl eine kinetische Zersetzung in diesem Material auftritt. Untersuchungen der BSCF-Membranen während zyklischer Permeationsversuche zeigen, dass die kubisch-hexagonale Phasenumwandlung reversibel ist und die Membranleistung durch die periodische Variation der Temperatur oberhalb 850 °C relaxiert. Die Kinetik für die kubisch-hexagonale Phasenumwandlung wurde gemäß der Langzeit-Auslagerungsversuche in dieser Studie diskutiert. Zusammenfassend wird die Sauerstoffdurchlässigkeit und Stabilität der Membranen und deren starke Abhängigkeit von der Temperatur, dem Partialdruck des Sauerstoffs und der chemischen Zusammensetzung, insbesondere hinsichtlich des Kobaltgehalts untersucht.

Abstract

The thermochemical properties, especially the long-term behaviour of mixed electron-ion conducting materials for oxygen separation, were investigated under oxyfuel condition in this thesis. Amongst those oxygen-permeable materials, perovskite-type oxides demonstrate remarkably high oxygen fluxes. Nevertheless, great effort has been put into the investigation of the long-term sustainable problem occurring in the intermediate temperature (IT) range of 500-800 °C in some perovskite membranes, which is caused by thermodynamic decomposition. This decay of membrane properties during operation becomes a serious obstacle for applications in coal-fired power plants. Besides, a relatively low expansion coefficient of membrane materials is also suggested to avoid compatibility issues.

Perovskite-structured $Ba_xSr_{1-x}Co_yFe_{1-y}O_{3-\delta}$ (BSCF) materials were synthesized by the method of solid state reaction. The sintering behaviour of BSCF powders was studied prior to the production of the gastight membranes. In view of future application, characteristic membrane properties like melting temperature, oxygen nonstoichiometry and thermal expansion behaviour were measured in synthetic air accordingly. The association between the thermochemical properties and the doping compositions of BSCF materials as well as temperature effect was investigated.

Moreover, the degradation process in BSCF membranes during long-term operation was studied under oxyfuel condition. In the case of oxygen permeation measurements, the variation of oxygen flux through the membranes under the air/He pressure gradient was recorded. A slow exponential decay of the permeate flux was observed at 800 °C compared to the more stabilized oxygen permeability of membranes at higher temperatures. The reason for the deterioration of membrane permeability is mainly ascribed to the phase decomposition from cubic into hexagonal polymorph. Unexpectedly, an increment of oxygen flux was found in the $Ba_{0.4}Sr_{0.6}Co_{0.2}Fe_{0.8}O_{3-\delta}$ membrane measured at 850 ℃, though kinetic decomposition still occurs in this material. Based on the permeation behaviour of BSCF membranes during cyclic permeation tests, it is confirmed that the cubic-hexagonal phase transition is reversible and membrane performance could be retrieved by the periodical variation of temperatures above 850 °C. The driving force as well as kinetics for the phase transition is discussed in this study according to the long-term annealing measurements. In conclusion, the oxygen permeability and stability of membranes are proven to be strongly dependent on temperature, oxygen partial pressure and chemical composition, most notably concerning the cobalt content.

Content

1 Introduction

The global primary energy demand, declared by the international Energy Agency, has rebounded strongly by 5% in 2010 [1], along with a growth of global CO_2 emission at a rate of 5.9% to reach 33.5 $Gtyr^{-1}$ [2], pushing the environmental warming issues to a more serious condition. Electric power generation remains the single largest source of CO_2 emissions and over 50% of the European electricity comes from fossil-fuelled power plants [3]. In the meanwhile, despite of new policies proposed each year to promote the deployment of unconventional energy resources with the aim of reducing CO_2 emission, fossil fuels will still dominate the supply of primary energy till at least the middle of this century [4]. Amongst the fossil sources, coal contributes to almost half of the increase in global energy demand over the last decades and its consumption would rise by a further 65% by 2035, overtaking oil as the largest fuel in the global energy mix [1]. It all means the exploration of more efficient energy technologies as well as future power plant designs with minimized CO_2 emission, especially those for coal-fired plants, is urgently called for to satisfy both the boosting economy and climate requirements.

Under this condition, the importance of carbon capture and storage (CCS) technologies rises and CCS comes to one of the viable options for emission reduction at commercial scale. It involves a three stage technology where CO_2 is separated from large industrial and energy-related sources, transported to storage sites and then injected into underground geologic formations for long-term entrapment. For the capture step in fossil-fuelled power plants, separation technologies can be used to collect high purity CO_2 after combustion or to decarbonize the fuel before combustion. The captured CO_2 could be typically compressed into high density to facilitate the transport to locations with access to suitable CO_2 storage. A power plant equipped with a CCS system has the capability to reduce CO_2 emission to the atmosphere by approximately 80-90% compared to a plant without CCS [4]. However, CCS technologies are yet too costly for large scale application in conjunction with other potential barriers, particularly the possible leaking risks during transport or storage timescale that may further inhibit the CCS deployment. Even though various possibilities can be considered to reduce the high cost, technological progress seems to be the main concern for CCS implementation, especially in the field of CO_2 capture where the major cost stems from.

The present work deals with oxygen separation materials for the oxyfuel process, one of the principal technologies for CO_2 capture. Suitable materials to extract oxygen from air are required to possess proper thermal expansion coefficient, high oxygen permeability and adequate long-term sustainability. In this study, the thermochemical behaviour of the selected materials, especially the degradation of membranes during long-term operation at intermediate temperatures, was investigated to assess their suitability for future application in coal-fired power plants.

2 Scope of work

The main aim of this study is to characterize the mixed ionic and electronic conducting (MIEC) oxides that are potentially interesting materials for applications in the field of oxygen separation in the oxyfuel process. According to the published literature, promising membrane materials were selected and the solid-state reaction method was chosen for powder synthesis. The powder products were analyzed in terms of phase composition, particle size distribution as well as the sintering behaviour.

Moreover, the thermochemical properties of membrane materials play an important role in the practical applications. For example, high thermochemical expansion coefficient of membrane materials may cause thermal mismatch with other components during operation at high temperatures and thus induce technical failure in the power plant. In addition, the variation of oxygen stoichiometry in the perovskite oxides has a significant effect on the oxygen permeability of membranes. Therefore, both factors were determined for each membrane material at intermediate temperatures in synthetic air.

Considering the working conditions in power plants, particular interest lies in the long-term behaviour of MIEC membranes with respect to their sustainability of producing a continuous and sufficient oxygen permeation flux. First of all, the structural stability of the perovskite-type membrane materials was predicted by Goldschmidt tolerance factor as a function of the cation concentration as well as oxygen nonstoichiometry. Secondly, long-term permeation measurements were performed in a tubular furnace for 2000 h under the air/He partial pressure gradient. Various factors, such as temperature, membrane thickness, cations concentration, were evaluated regarding their impacts on the long-term permeation stability of the membranes. Further studies were focused on the change of membrane performance through periodical variation of temperature in the cyclic permeation tests. In order to trace the phase decomposition occurring during long-term operation, BSCF samples were annealed at intermediate temperatures for different periods. Accordingly, the driving force for kinetic decomposition and the growth kinetics of hexagonal phase in the membrane materials were clarified.

3 Fundamentals

3.1 CO_2 capture and storage technologies

Currently, most of the CO_2 removed from industrial gas stream is emitted directly to the atmosphere; while only in a few cases, the capture process has been used for storage purposes. Therefore, in future fossil-fuelled power plant designs, large-scale application of CO_2 capture and storage (CSS) technologies to control carbon emission with the aim of staving environmental change becomes absolutely necessary. The purpose of CO_2 capture is to produce a highly concentrated gas stream of CO_2 that can be practically and economically transported to a storage site. There are three main approaches: pre-combustion, post-combustion and oxyfuel combustion to CO_2 capture in the power plants.

3.1.1 Pre-combustion process

As carbon dioxide is certainly not available for capture before combustion, the term of pre-combustion capture is somehow an oxymoron. Pre-combustion processes subsume the gasification of the primary fuels in a reactor with sub-stoichiometric amounts of air or oxygen at elevated pressures to produce a synthesis gas mixture composed principally of CO and H_2. Then additional steam is supplied and the mixture is passed through a series of catalyst beds in a water-gas shift reactor for the conversion of CO with steam:

The produced CO_2 gas is separated afterwards from the resulting mixture to leave a hydrogen-rich fuel gas, which is a carbon-free energy input for combustion to generate power or heat. Therefore, the pre-combustion process is commonly applied at power plants that employ integrated gasification combined cycle (IGCC) technology. The schematic diagram of the pre-combustion process is shown in **Fig. 3.1**.

Most CO_2 separation technologies in the pre-combustion process are based on the use of solvents. There are two major types of solvents available for this procedure: chemical solvents and physical ones [5]. All these solvents can accomplish more than 90% removal of the CO_2 gas. However, physical solvents are typically used for this separation procedure. In this case, the CO_2 product is dissolved in the solvent at high pressure in the first step and then released by changing the conditions around the rich sorbent (e.g., by heating the sorbent or decreasing the pressure). The reason for the common use of physical solvents is that no additional energy is required for the regeneration of the solvent. The captured CO_2 can be easily released just after a pressure decrease, leading to 2/3 of the energy penalty compared to that in post-combustion [6]. Amongst these solvents, the methanol-based process was found to show the best performances in terms of the energy penalty [7], the cost of electricity per kWh and the removal cost of CO_2 per ton. In addition to the use of solvents for CO_2 capture, membrane systems are addressed to be more economical when the CO_2 concentration in natural gas is high [4]. Amelio et al. compared the classical CO_2 adsorption removal with innovative membrane separation technologies in the pre-combustion process [8]. Several options of membrane technologies considering CO_2/H_2 separation with amine-containing membranes [9], membranes containing potassium carbonate-glycerol [10], dendrimer-containing membranes [11] etc., are described.

However, the pre-combustion systems have to incur high production costs and additional efficiency losses for the shift reaction as well as for the capture process. Despite of these disadvantages, the pre-combustion process produces high concentration and also high pressure of CO_2 (typically 15 to 60% by volume on a dry basis [4]) that are favorable for CO_2 separation.

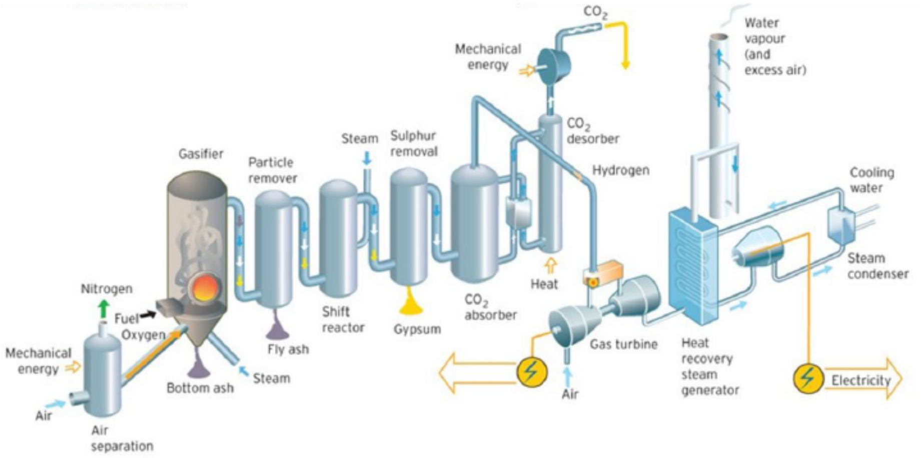

Fig. 3.1 Schematic diagram of a power plant with the pre-combustion system [12]

3.1.2 Post-combustion process

Post-combustion capture (PCC) aims to selectively separate the CO_2 from exhaust gases after combustion in the boiler. The goal is the enrichment of the CO_2 from a relative low content of 5-15% [13, 14] towards an almost pure CO_2 stream. The PCC process has the advantage that it can be retrofitted in principle to any existing plant without requiring substantial change of the basic conditions. To date, technologies of chemical adsorption with monoethanolamine (MEA)-based solvents appear to be the most acceptable adoption to this CO_2 separation process. Gas cleaning is desirable to reduce pollutants, such as SO_x emission to an acceptable level (~10 ppm) in order to avoid the loss of costly solvents [15]. However, this process requires a large amount of energy to regenerate the solvent, which consumes as much as 80% of the total energy [16]. To improve the PCC technology, membrane contactors are proposed in order to attain intensified gas-liquid CO_2 absorption in the chemical solvents [17]. Nevertheless, no special improvement in the energy efficiency of the overall power plant process is achieved through this approach. With the purpose of replacing the traditional gas-liquid absorption process, a technique based on membrane separation has been developed [18]. Dense polymeric membranes are most often suggested and have been systematically tested in the dry CO_2/N_2 gas mixture environment for their physical separation capability [19-21]. Other membranes based on chemical reactions, e.g. fixed site carrier membranes and liquid membranes, offer the possibility of extremely high selectivity (for example, CO_2/O_2 selectivity = 4100 [22]). Depending on the settings of the post-combustion process, 85-90% of the CO_2 in the exhaust gases can be captured [23]. The schematic diagram of a power plant with the post-combustion system is shown in **Fig. 3.2**.

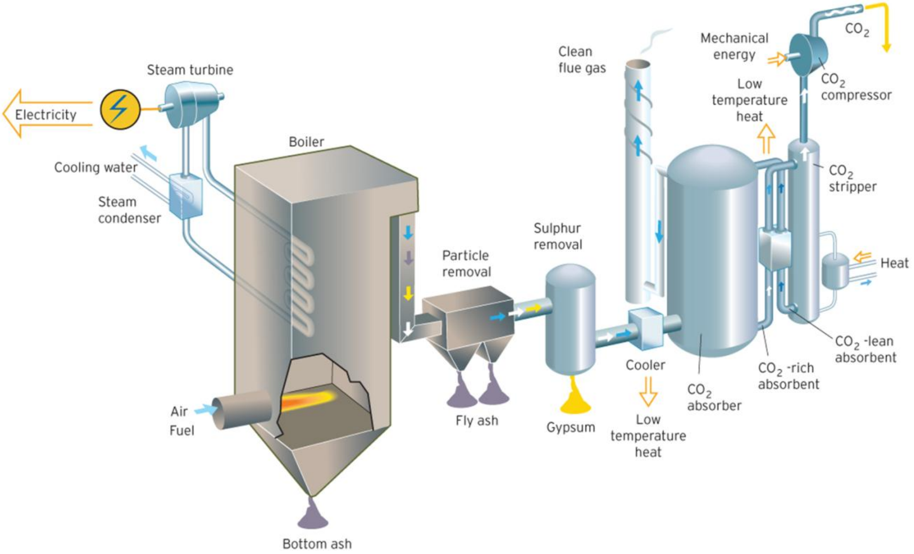

Fig. 3.2 Schematic diagram of a power plant with the post-combustion capture technique [12]

3.1.3 Oxyfuel process

In the oxyfuel process, primary fuel is combusted in a mixture of injected pure oxygen (larger than 95% purity) and recycled flue gas to produce an exhaust gas that contains mainly CO_2 (larger than 80%) and water vapour. Since this technique avoids the dilution of flue gases with nitrogen as in the case of conventional combustion with air supply, it significantly increases the partial pressure of CO_2 in the exhaust gases. When higher CO_2 concentration is achieved after combustion, the driving force for the CO_2 separation increases and hence makes the capture process much easier. In addition, less energy is consumed for CO_2 capture as the removal of nitrogen from the flue gas is deliberately avoided. Moreover, heat transfer in the convective section of the boiler is also prompted due to the larger thermal capacity of CO_2 and water vapour compared to nitrogen [16]. In view of its efficiencies and costs, oxyfuel combustion appears to be quite competitive with amine-based post-combustion plants and a number of boiler manufactures [5].

Oxyfuel combustion could be employed with solid fuels such as coal, petroleum coke, biomass, as well as liquid and gaseous fuels. The schematic diagram of a fuel-fired oxyfuel boiler is shown in **Fig. 3.3**. In a pulverized coal combustion system, a great part of the exhaust gases are recycled to control the flame temperature in the boiler [24]. Such recycling treatment of the flue gas can prevent full resizing of the boiler and its associated exchangers.

After combustion, the CO_2 content is about 75% in the wet exhaust gases. Water vapour in the flue gas can be easily condensed and separated from the mixture, resulting in 80-90% CO_2 on a dry basis. Oxides of nitrogen and sulphur (NO_x, SO_x) from combustion must be removed from the flue gases as in a conventional power plant before or during the CO_2 compression process. As a consequence, a dehydration system using triethylene glycol followed by a cryogenic impurity separation device is commonly recommended integrating into the CO_2 compression/liquefaction step [25]. It should be noticed that the presence of non-condensed gases (e.g., N_2) in the flow can cause vibrations and shock loads in the pipes during transport by the pipeline in the supercritical state. Further treatment may be required to remove air pollutants and other incondensable gases before the storage of CO_2. Eventually, a flue gas with the CO_2 concentration above 98% is obtained. Very high CO_2 purity (more than 99.9%) was achieved by using an additional distillation process, though it would cause an additional efficiency loss of about 0.2%-points [26].

For the oxyfuel combustion, several aspects should be taken into account, including the optimization of the purity level of oxygen in the boiler, the purity degree of the CO_2 product, the degree of leakage during the exhaust gas circuit as well as the influencing parameters on the CO_2 capture rate. The pure oxygen demand (95-99% purity in most current designs [4]) for this process can be provided by air separation units (ASUs), where oxygen transport membranes (OTMs) are generally selected due to their good oxygen permeability and low efficiency losses at operating temperatures between 800 and 1000 °C [27]. However, there are many problems with this technique: impact of dust, steam and the degradation of membranes under oxyfuel condition. Along with these problems, the additional ASU component does require additional energy, resulting in a decrease in the net efficiency of the power plant. Therefore, the conceptual designs for this process are still in the research phase.

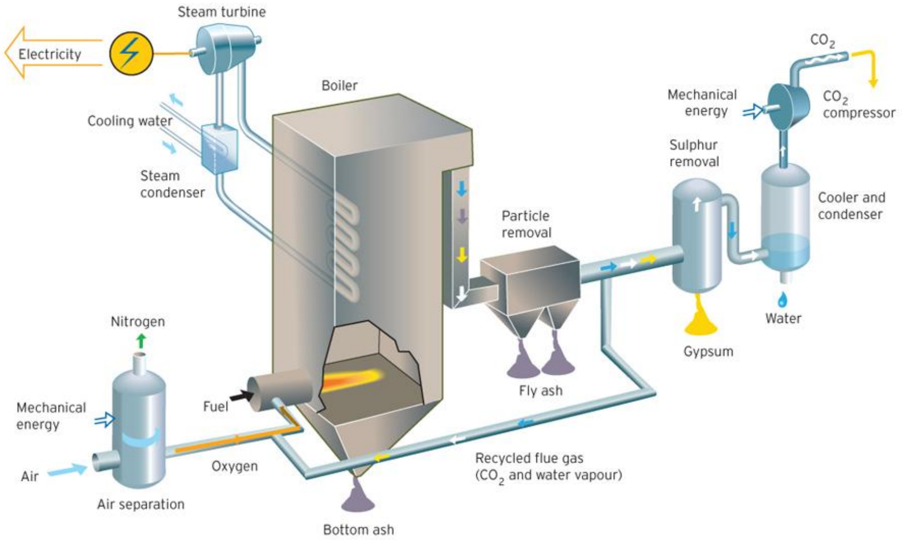

Fig. 3.3 Schematic diagram of a power plant with the oxyfuel combustion capture technique [12]

3.2 Mixed ionic and electronic conductors (MIEC)

Mixed ionic and electronic conducting (MIEC) oxides have been employed in the forefront of ceramic-based membrane technologies for their versatile applications in the fields of syngas production [28], gas separation [29-31] and solid oxide fuel cell [32]. As an elementary step in the oxyfuel process for CO_2 capture, oxygen/nitrogen separation can be realized by dense inorganic MIEC membranes. These membrane materials should exhibit infinite permselectivity so that only oxygen is allowed to pass towards the permeate stream. In addition, proper MIEC membranes must display significant electronic conductivity as well as notable ionic conductivity in order to provide sufficient oxygen flux.

3.2.1 Materials structure of MIEC membranes

The most promising materials of OTMs are those of the perovskite type with the formula ABX_3. The structure of ideal perovskites can be described as a cubic close packing of A and X ions together with B cations occupying the sixfold coordination side, as shown in **Fig. 3.4**. The A and B cations in the ideal case realize their equilibrium bond distances to oxygen (the ratio of the A-O bond length to the length of

B-O bond is $\sqrt{\ }$:1) without inducing any distortion of the cubic unit cell and they adopt the space group Pm3m. In three-dimension, the ideal ABX_3 perovskite structure is composed of a framework of corner-sharing BX_6 octahedra and the A-site cations occupy the 12 coordinate cavities AX_{12} surrounding eight BX_6 octahedra. In other words, the B-site cations are surrounded by six anions in octahedral coordination, while the A-site cations are surrounded by 12 anions in cubo-octahedral coordination. The X-site anions are coordinated by two B-site cations and four A-site cations [33]. Generally, the ionic radius of A ions is larger than that of B ions.

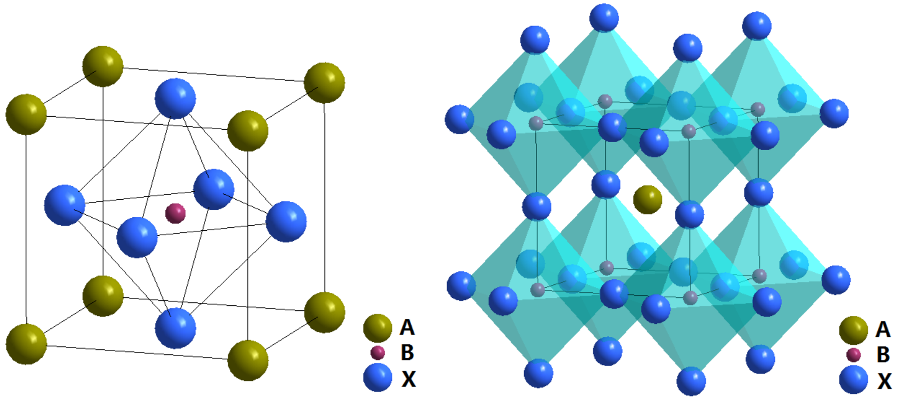

Fig. 3.4 Ideal perovskite structure ABX_3

This perovskite structure combines great flexibility and chemical stability due to the presence of two different cations. Thus it permits custom tailoring of the physical-chemical properties of materials either by doping the A and B sites with different elements or by changing the cation stoichiometry. The elements for chemical doping at the A site are various, such as alkaline, alkaline earth and rare earth ions; while the B-site ions are often of the transition metals with multiple oxidation states. Though majority of the perovskite ceramics are oxides or fluorides, other forms such as heavier halides, sulphides, hydrides, cyanides, oxyfluorides and oxynitrides were also reported [34]. Amongst the perovskite-type oxides, those that have been frequently investigated are rarely of the simple ABO_3 type but complex ones with A- or/and B-site partially substituted. Considering the case where the trivalent A cations in $A^{3+}B^{3+}O_3$ are partially replaced by divalent A' cations (e.g., Ba, Sr), the charge neutrality must be balanced by adding tetravalent B cations or by the stoichiometric formation of oxygen vacancies.

The latter would lead to the creation of non-stoichiometry δ in the perovskite More generally, if both the A- and B-site cations are partially substituted, the perovskite structure could be described by the formula $A_xA'_{1-x}\ B_yB'_{1-y}O_{3-\delta}$.

In view of the diverse compositions of perovskite-type compounds, it is essential to find out regularities to guide the exploration of new perovskite ceramics. In early 1920s, Goldschmidt proposed a tolerance factor τ to predict the formation of perovskite structure by a given assembly of ions [35]:

$$\tau \quad \frac{r \quad r}{\sqrt{\ }(r \quad r\ )}$$

r_A	the ionic radii of A-site cations
r_B	the ionic radii of B-site cations
r_O	the ionic radius of oxygen ion

For an ideal perovskite, the bond length is roughly assumed to be the sum of two ionic radii and the τ value should be equal to 1.0. However, in many perovskites, the A-O and B-O bond lengths are geometrically incompatible and lower symmetry structures are stabilized. In the case of the tolerance factor $\tau < 1.0$, the A-O bond distance is shortened due to the undersized A-site space. The coordination number of the A cation is lowered through a correlated tilting of the surrounding BO_6 octahedra network. On the other hand, if the tolerance factor is larger than 1.0, the AO_3 layer typically follows mixed cubic and hexagonal, or pure hexagonal close packing sequences. The introduction of hexagonal stacking is accompanied by the face-sharing of adjacent BO_6 octahedra and by the formation of 90° B-O-B bond angles [36]. The τ values of most cubic perovskites were found in the range of 0.8-0.9 rather than being 1.0 as for an ideal perovskite [35]. A more general criterion was given that $\tau = 0.75\text{-}1.00$ [37] is necessary for the formation of perovskite structure.

However, there exist many systems with tolerance factors in the favourable range but do not possess any perovskite structure [38], like $Cu_2O\text{-}P_2O_5$, $Li_2O\text{-}As_2O_5$, $MnO\text{-}GeO_2$, $Al_2O_3\text{-}B_2O_3$ [39]. This means the Goldschmidt's factor is merely a rough estimate of the structure, since factors other than ion size, such as covalence state, metal-metal interactions, Jahn-Teller and ion pair effects may also play a role in determining the space group and thus the structure. Therefore, another factor regarding the formation of the octahedron BO_6 as the basic unit of perovskite structure [40] has been defined as the octahedral factor (f_O):

$$f \quad \frac{r}{r}$$

It has been reported [41, 42] that the ratio of the ionic radii (r_B/r_O) should be limited in a certain range to form an octahedron consisting of one cation and six anions. For an ideal perovskite, the f_O value is equal to 0.425. This factor could vary in the range of 0.414-0.732 to ensure the formability of perovskites. According to the research by Li et al. [39], there is a lowest limit of the radius of B-site cation that no stable perovskite could form when the B ions are smaller than 0.53 Å, even this system shows a favourable value of the tolerance factor. On the same basis, this octahedron formability could be predicted by the ratio of cation and anion sizes (r_c/r_a) as well. The reported lowest limit of the r_c/r_a ratio for octahedra is 0.414 [41, 42].

3.2.2 Thermochemical properties of MIEC membranes

The key properties of MIEC materials for gas separation involve the thermochemical expansion behaviour, the variation of oxygen stoichiometry as well as the thermal stability of membranes with respect to long-term operation in power plants. All these factors correlate with each other and should be considered as criteria for the assessment of the entire membrane technologies.

Oxygen non-stoichiometry

Numerous oxide compounds in nature are non-stoichiometric with the existence of defects in the crystals. Two types of defects are generally classified, i.e. structural defects and electronic defects. Structural defects can be subdivided into point defects, line defects and planar defects [43]. Electronic defects, including electrons and electron holes are formed by intrinsic ionization or excitation of electrons from valence to conduction band [44]. They could also be created in association with point defects to fulfil the electric neutrality criteria. In the case of MIEC membranes, the formation of oxygen vacancies in the non-stoichiometric oxides is an example of point defects. Upon heating, the multivalent cations on the B-site are reduced to lower valences together with the release of lattice oxygen. Therefore, oxygen vacancies are introduced in the membranes, which is responsible for ionic conductivity. While, to complement the generation of oxygen vacancies, electrons arise concurrently inside these oxygen-deficient conductors, resulting in the electronic conductivity [45, 46]. Due to the existence of these defects, oxygen ions could be transported through the MIEC membrane (further discussion in **Chapter 3.3**). To simplify this theory, the oxygen deficit δ of perovskite $\quad_{3-\delta}$ materials is assumed only dependent on the equilibrium concentration of double ionized oxygen vacancies in the lattice.

The relative concentration of ionic/electronic defects and the oxygen nonstoichiometry δ of the oxides are influenced by temperature as well as oxygen partial pressure [47]. Theoretically, the oxygen vacancies concentration is expected to change with $pO_2^{-1/2}$ for a material with dominating electronic disorder ($[e'] = [h^{\cdot}]$) and with $pO_2^{-1/6}$ for dominating ionic disorder ($2[\ _{O}] = [e']$). Bucher et al. [48] investigated the oxygen deficiency of $Ba_{0.5}Sr_{0.5}Co_{0.8}Fe_{0.2}O_{3-\delta}$ in the range $600 \leq T \leq 900$ ℃ and $10^{-4} \leq pO_2 \leq 0.4$ bar by isobaric experiments. They found the oxygen nonstoichiometry increases continuously with temperature but decreases with pO_2. A good linear correlation of $\ln pO_2$ vs. $\ln (3-\delta$ was obtained at a certain temperature.

In addition, Yamazoe et al. [49] discerned two types of oxygen desorption in $La_xSr_{1-x}CoO_3$ termed as α and β desorption in accordance with their appearance in different temperature regions. They associated α oxygen with the oxygen vacancies formed by A-site substitution of Sr^{2+} for La^{3+} at 227-577 ℃ , whereas β oxygen corresponds to the reduction of cobalt ions at temperatures above 577 ℃ . In both cases, oxygen desorption occurred and leaded to the variation of oxygen deficiency in this material during heating. This implies that the oxygen nonstoichiometry might change with the partial substitution of A-site cations as well as the reduction/oxidation state of the transition metal ions at B-site in the perovskite oxides. Anderson [50] and Mizusaka [51] proposed that the substitution of divalent alkaline-earth ions on the A-site would increase the concentration of oxygen vacancies. Accordingly, an increase in the ionic conductivity by strontium doping in $La_xSr_{1-x}Co_{0.8}Fe_{0.2}O_{3-\delta}$ was observed [52]. Zeng et al. [53] measured the oxygen nonstoichiometry δ of $Ba_{0.5}Sr_{0.5}Co_{0.8}Fe_{0.2}O_{3-\delta}$ and $SrCo_{0.8}Fe_{0.2}O_{3-\delta}$ at room temperature (RT) by the ideometry titration method. higher δ value was achieved in $Ba_{0.5}Sr_{0.5}Co_{0.8}Fe_{0.2}O_{3-\delta}$ compared to $SrCo_{0.8}Fe_{0.2}O_{3-\delta}$, which according to their explanation is ascribed to the larger ionic radius of Ba^{2+} compared to that of Sr^{2+}. However, both materials were found to release oxygen at the same onset temperature of ~300 °C. This means the partial substitution of barium for strontium does not influence the bonding energy of metal ion-oxygen in the lattice. Based on the research by Ullmann et al. [54], the oxygen loss increases by enhancing the doping of strontium in $(La/Pr)_xSr_{1-x}Co_yMn_{1-y}O_{3-\delta}$ and $Sr_xCe_{1-x}Co_yFe_{1-y}O_{3-\delta}$, while the highest concentration of oxygen vacancies was reached in the strontium cobalt $SrCoO_{3-\delta}$. Higher A/B sub-stoichiometry in the perovskite $ABO_{3-\delta}$ was confirmed to accelerate the process of oxygen release. Shao et al. [55] observed the oxygen desorption peak of $Ba_{0.5}Sr_{0.5}Co_{0.8}Fe_{0.2}O_{3-\delta}$ at intermediate temperatures of 300-600 °C, which is attributed to the reduction of high valence state (Co^{4+} and Fe^{4+}) to trivalence state (Co^{3+} and Fe^{3+}). Merkle et al. [56] have calculated the formation energy of oxygen vacancy E_v as a function of iron content in $Ba_{0.5}Sr_{0.5}Co_{1-y}Fe_yO_{2.875}$ ($y = 0.0\text{-}1.0$). Over the whole composition range, E_v increases linearly with the iron content from 1.2 eV for $Ba_{0.5}Sr_{0.5}CoO_{2.875}$ to 2.2 eV for $Ba_{0.5}Sr_{0.5}FeO_{2.875}$. It was confirmed by Chen et al. [32] that the higher iron content in $Ba_{0.5}Sr_{0.5}Co_yFe_{1-y}O_{3-\delta}$, the smaller nonstoichiometry was achieved. As a result, it gives the reason for the drop of ionic conductivity in $BaCo_yFe_{1-y}O_{2.5}$ by increasing the iron content as fewer oxygen vacancies can be formed thermodynamically in the perovskites [57]. The reported values of oxygen nonstoichiometries in perovskite-type materials are summarized in **Tab. 3.1**. It is clear that the δ values vary significantly, depending on the experimental conditions. Nevertheless, in order to predict the membrane behaviour for oxygen separation, it is necessary to investigate the variation of oxygen nonstoichiometry during process.

Tab. 3.1 Oxygen nonstoichiometry values for perovskite-structured materials

Materials	T / °C	pO_2 / bar	δ / -	References
$Ba_{0.5}Sr_{0.5}Co_{0.8}Fe_{0.2}O_{3-\delta}$	600	0.4	0.43	[48]
$Ba_{0.5}Sr_{0.5}Co_{0.8}Fe_{0.2}O_{3-\delta}$	700	0.21	0.46	[48]
$Ba_{0.5}Sr_{0.5}Co_{0.8}Fe_{0.2}O_{3-\delta}$	700	10^{-3}	0.52	[48]
$Ba_{0.5}Sr_{0.5}Co_{0.8}Fe_{0.2}O_{3-\delta}$	900	10^{-4}	0.60	[48]
$Ba_{0.5}Sr_{0.5}Co_{0.8}Fe_{0.2}O_{3-\delta}$	850	10^{-5}	0.68	[58]
$Ba_{0.5}Sr_{0.5}Co_{0.8}Fe_{0.2}O_{3-\delta}$	1000	0.01	0.64	[58]
$Ba_{0.5}Sr_{0.5}Co_{0.8}Fe_{0.2}O_{3-\delta}$	700	0.21	0.26	[59]
$Ba_{0.5}Sr_{0.5}Co_{0.8}Fe_{0.2}O_{3-\delta}$	800	0.21	0.28	[59]
$Ba_{0.5}Sr_{0.5}Co_{0.8}Fe_{0.2}O_{3-\delta}$	850	0.21	0.30	[59]
$Ba_{0.5}Sr_{0.5}Co_{0.8}Fe_{0.2}O_{3-\delta}$	900	0.21	0.32	[59]
$Ba_{0.5}Sr_{0.5}Co_{0.8}Fe_{0.2}O_{3-\delta}$	700	0.21	0.68	[60]
$Ba_{0.5}Sr_{0.5}Co_{0.8}Fe_{0.2}O_{3-\delta}$	700	1.0	0.69	[60]
$Ba_{0.5}Sr_{0.5}Co_{0.8}Fe_{0.2}O_{3-\delta}$	700	1.0	0.34	[61]
$SrCo_{0.8}Fe_{0.2}O_{3-\delta}$	800-1000	10^{-6}	0.50	[62]
$Ba_{0.1}Sr_{0.9}Co_{0.8}Fe_{0.2}O_{3-\delta}$	500	10^{-6}	0.37	[62]
$Ba_{0.3}Sr_{0.7}Co_{0.8}Fe_{0.2}O_{3-\delta}$	500	10^{-6}	0.42	[62]
$Ba_{0.5}Sr_{0.5}Co_{0.8}Fe_{0.2}O_{3-\delta}$	500	10^{-6}	0.52	[62]
$Ba_{0.5}Sr_{0.5}Co_{0.8}Fe_{0.2}O_{3-\delta}$	700	10^{-3}	0.78	[62]
$Ba_{0.5}Sr_{0.5}Co_{0.8}Fe_{0.2}O_{3-\delta}$	700	0.21	0.26	[63]
$Ba_{0.5}Sr_{0.5}Co_{0.8}Fe_{0.2}O_{3-\delta}$	600	1.0	0.66	[64]
$Ba_{0.5}Sr_{0.5}Co_{0.8}Fe_{0.2}O_{3-\delta}$	900	10^{-3}	0.81	[64]

Thermochemical expansion

It is apparent that the thermal expansion of membrane materials is dominated by the electrostatic attraction forces within the lattice. Smaller attraction forces induce larger thermal expansion. The concentration of positive and negative charges as well as their distances in the lattice makes an impact on the attraction forces. For a lattice with a certain structure and fixed oxygen-to-metal stoichiometry, steady thermal expansion behaviour is supposed to display as a result of the thermal lattice vibrations, denoted by a constant thermal expansion coefficient (TEC). However, other types of thermal expansion caused by spin transition or/and chemical expansion [65, 66] might be observed in perovskite materials. As mentioned above, an oxygen loss coupled with the creation of oxygen vacancies occurs within some perovskites either by increasing temperature or by providing a reducing gaseous environment. Accordingly, an additional expansion caused by the change of oxygen vacancies concentration in the lattice is referred to as chemical expansion. Upon heating, the B-site cations (e.g. Co, Fe) are reduced to a lower valence state [54, 67] with larger ionic size [68], which is regarded as the primary reason for chemical expansion. Another contribution to this expansion is attributed to the Coulomb repulsion of the neighbouring cations in the absence of compensating oxygen ions. The chemical expansion coefficient can be formulated by [69]

$$\frac{d_{\text{rel}}}{d\delta}$$

here, dL_{rel} is the relative change of the length per unit of the oxygen stoichiometry change $d\delta$ at constant temperature.

Zeng et al. [53] investigated the thermal expansion behaviour of $Ba_{0.5}Sr_{0.5}Co_{0.8}Fe_{0.2}O_{3-\delta}$ and derived the TEC value from the high-temperature XRD results. Based on their research, the value was around 21×10^{-6} K^{-1} in the temperature range from room temperature (RT) to 1000 °C. Similarly, Lu et al. [70] calculated the TEC of $Ba_{0.5}Sr_{0.5}Co_{0.8}Fe_{0.2}O_{3-\delta}$ and $SrCo_{0.8}Fe_{0.2}O_{3-\delta}$ in the same temperature range (RT-1000 °C) by XRD analysis. In $Ba_{0.5}Sr_{0.5}Co_{0.8}Fe_{0.2}O_{3-\delta}$, an inflection of the TEC curve was found at 600 ℃ . Below this temperature, the material shows an expansion with the TEC equal to 16×10^{-6} K^{-1} and the value jumps to 31×10^{-6} K^{-1} at high temperatures. Larger thermochemical expansion was achieved in $SrCo_{0.8}Fe_{0.2}O_{3-\delta}$ with the TEC values of 28×10^{-6} K^{-1} and 39×10^{-6} K^{-1} in the low and high temperature regions, respectively. As both materials have similar compositions, the different expansion behaviors are mainly ascribed to their different chemical expansion due to the presence of barium in the lattice. Zhu et al. [71] measured the thermal expansion of $Ba_xSr_{1-x}Co_{0.8}Fe_{0.2}O_{3-\delta}$ (x = 0.0-0.6) in flowing air between RT and 850 °C by a dilatometer. They concluded that the thermal expansion behavior of these materials is strongly dependent on the content of barium, e.g. the overall expansion coefficient of samples with lower barium content (x = 0.1, 0.2) are much larger compared to the others. Moreover, all these expansion curves exhibit a sudden increase in their slopes between ~500 °C and 650 ℃. This inflection temperature was also found to be dependent on the barium content. Whereas a lower temperature range of 350-550 ℃, where the inflection occurs, was also observed in the nonlinear expansion curves of $Ba_xSr_{1-x}Co_{0.8}Fe_{0.2}O_{3-\delta}$ (x = 0.3-0.7) [72]. The appearance of these inflection points in the expansion curves is mainly assigned to the loss of lattice oxygen in the perovskites at intermediate temperatures.

If considering the $Ba_xSr_{1-x}Co_yFe_{1-y}O_{3-\delta}$ (BSCF) system, such oxygen release should be charge compensated by the reduction of iron and cobalt ions. This indicates that the behaviors of both B-site cations have a direct control over the thermochemical expansion of the lattice. Martínez et al. [73] calculated the linear thermal expansion coefficient of $Ba_{0.5}Sr_{0.5}Co_yFe_{1-y}O_{3-\delta}$ (y = 0.1-0.9) in air based on the XRD results. They observed a manifest increase in the TEC values with the Fe content in the temperature range of RT-700 ℃. Ovenstone et al. [74] derived the TEC values of $Ba_{0.5}Sr_{0.5}Co_yFe_{1-y}O_{3-\delta}$ (y = 0.2-0.8) under low oxygen partial pressure of 10^{-5} atm. The average TEC value was observed to increase continuously with iron content from 22.0×10^{-6} K^{-1} for $Ba_{0.5}Sr_{0.5}Co_{0.8}Fe_{0.2}O_{3-\delta}$ to 29.8×10^{-6} K^{-1} for $Ba_{0.5}Sr_{0.5}Co_{0.2}Fe_{0.8}O_{3-\delta}$. From the other aspect, the cobalt-enriched perovskites usually show high chemical expansion, which is partially due to the large variation of the ionic radii of cobalt ions when their oxidation state changes [68]. Wei et al. [72] identified one or two additional peaks in the derivate thermal expansion curves of $Ba_xSr_{1-x}Co_{0.8}Fe_{0.2}O_{3-\delta}$ around 900 ℃, representing the further reduction of Co^{3+} to Co^{2+}. While, the characteristic temperature for the thermal reduction of Fe^{3+} to the lower state in air is about 1560 °C [75].

Kriegel et al. [58] investigated the thermal expansion behavior of $Ba_{0.5}Sr_{0.5}Co_{0.2}Fe_{0.8}O_{2.51}$ in air and argon atmospheres. The expansion procedure was found to be reversible in ambient air and the material was re-oxidized upon cooling. On the contrary, the chemical expansion was much larger in the flowing argon than in air as more oxygen could be released from the lattice. No significant influence of oxygen stoichiometry on the thermal expansion behavior was detected [58]. According to the research by McIntosh et al. [64], a slight decrease in the TEC values from 20.8×10^{-6} K^{-1} to 19.0×10^{-6} K^{-1} for $\delta = 0.72$ and δ 0.80 respectively was observed. Proper doping of the B-site cations with metals of a constant oxidation state, such as Zr^{4+}, is proposed in order to suppress the variation of oxygen nonstoichiometry and also the lattice expansion induced by the changes in temperature or oxygen partial pressure [76].

3.3 Oxygen transport mechanisms

The transport mechanisms in the MIEC membrane are schematically shown in **Fig. 3.5**. The driving force for the overall oxygen transport has to be provided either by an electrical potential gradient or by a chemical potential gradient, e.g. the differential oxygen partial pressure gradient across the membrane.

The transport of gaseous oxygen from the interface at high oxygen partial pressure $p'O_2$ to the side with low oxygen pressure $p''O_2$ involves three steps:

(i) the surface-exchange reaction on interface I under high oxygen partial pressure
(ii) the diffusion of charged ions and electrons/electron holes in the bulk phase
(iii) the surface-exchange reaction on interface II under low oxygen partial pressure

In a dense and gas-tight MIEC membrane, the direct passage of oxygen molecules is blocked. Oxygen is thus transported selectively through the membrane in the form of oxygen ions. Dissociation and ionization of oxygen occur firstly at the oxygen-rich side of the membrane via the reaction with oxygen vacancies in the lattice. Then different components diffuse within the oxygen deficient membrane according to their activity gradients. The flux of oxygen ions is charge compensated by the simultaneous counteracting flux of delocalized electrons or electron holes [45]. Both the ionic and electronic charge fluxes constitute the so-called ambipolar diffusion. When these individual oxygen ions reach the oxygen-lean side of the membrane, they recombine again with their electron holes to form oxygen molecules, which are desorbed into the permeate stream.

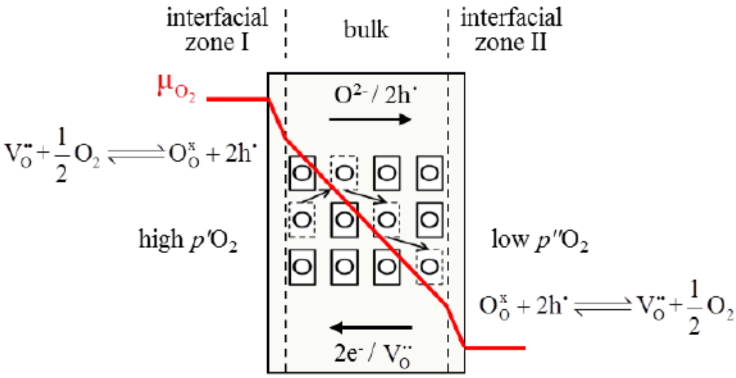

Fig. 3.5 Principle of oxygen transport through a perovskite membrane. is the chemical potential gradient between the interface with high oxygen partial pressure $p'O_2$ and the permeate side with low oxygen partial pressure $p''O_2$.

It is clear that oxygen permeation through a dense MIEC membrane is essentially limited by two factors, surface-exchange resistance on both interfaces of the membrane and the solid state diffusion kinetics within the bulk [77-79]. Lee et al. [77] indicated that the permeation of membranes in the thickness range of 1.0-2.6 mm is controlled by surface-exchange reaction and the diffusion of oxide ions. Wang et al. [59] revealed that the diffusion process predominates the rate of oxygen permeation for the 1.5 mm-thick $Ba_{0.5}Sr_{0.5}Co_{0.8}Fe_{0.2}O_{3-\delta}$ tubular membrane in the temperature range of 700-900 °C.

In lack of detailed knowledge of oxygen transport kinetics, a critical thickness L_c of the MIEC membrane is proposed to determine the rate-limiting step. It is defined as the membrane thickness at which both the diffusion and surface exchange impose equally large restrictions on the oxygen transport flux. L_c is expressed as

$$_{c} \quad \frac{_{i}}{k} \quad \frac{}{k}$$

k	the exchange flux normalized to the molar concentration of oxygen anions at equilibrium
D_i	self-diffusion coefficient of oxygen anions, assumed to be identical to D^*
D^*	tracer diffusion coefficient

Above L_c, bulk diffusion is rate determining and the oxygen flux can be increased by reducing the membrane thickness. However, marginal improvement of oxygen flux is achieved by the reduction of membrane thickness if its value is lower than the characteristic one. For the surface-exchange dominating oxygen transport, an improvement of surface properties via surface modification is suggested as an effective way to further improve the flux. The L_c value is dependent on temperature and oxygen partial pressure. Therefore, it is not an intrinsic material property though some cations concentration may influence the value of L_c in certain systems. In $La_xSr_{1-x}FeO_{3-\delta}$ oxides, for example, L_c was found to increase with Sr content [80].

Apparently, the driving forces (here corresponding to the oxygen partial pressure gradient across the membrane) and the temperature effect are major factors determining the oxygen permeation rate. While referring to the membrane properties, microstructure in relation to the mobility and concentration of charged species could also have an influence on oxygen transport.

Bulk diffusion

The oxygen permeation flux of sufficiently thick MIEC membranes is mainly determined by the slow diffusion of oxygen ions through the lattice. The interaction of gaseous oxygen with the oxide lattice is commonly described in the Kröger-Vink notation [81]:

$$- \quad \leftrightarrow \quad {}^{x} \quad h$$

with oxygen vacancies ( ), oxygen located at an oxygen lattice site (^{x}) and electron holes (h). Considering one simple case, the surface-exchange reactions on both membrane sides are fast and have no influence over the oxygen transport rate. The permeation rate is basically assumed to be determined only by the lattice diffusion of oxygen and the transport of electronic charge carriers. The flux of single component i can be determined under the premise that no interaction occurs among the moving charge carriers.

$${}_{i} \quad \frac{{}_{i}}{z_i}\nabla \quad {}_{i}$$

z_i	charge number
${}_{i}$	the conductivity of the single charge carrier
F	Faraday constant
$\nabla\eta_i$	the electrochemical potential gradient

In the case of oxygen ions flux, this equation is expressed as

$$\frac{}{}\nabla$$

while the counteracting electronic flux is:

$$_e \quad \frac{e}{}\nabla\ _e$$

If the charge species diffuses fast, this will lead to a gradient in the electrical potential and accelerate the transport of carriers with opposite charge. Now the $\nabla\ _i$ part can be subdivided into a chemical potential gradient $\nabla\ _i$ and an electrical potential gradient ∇ . Then for each charge component i,

$$\nabla\ _i \quad \nabla\ _i \quad z_i\ \nabla$$

In order to maintain the charge neutrality, the fluxes of ionic and electronic components should be correlated on the assumption that these charges are not accumulated and do not interact with each other,

$$^{-}\ _{e^-}\ ^{-}\ _h$$

Combining **Eq. 3.11** with **Eq. 3.8-3.10**, the flux of oxygen vacancies is deduced as a function of chemical potential gradient only, irrespective of electrostatic potential gradient. Here, it is postulated that these internal defects reactions are locally not influenced by the transport of matter. The relation of the potential gradients of different components then holds at equilibrium,

$$-\nabla \qquad \nabla \qquad \nabla\ _e$$

as the equation $\nabla\ _{e^-}\ \nabla\ _h$ exists due to the intrinsic ionization across the band. is the chemical potential of the oxygen vacancy, $_{e^-}$ and $_h$ the chemical potential of electrons and electron holes, respectively. Based on mass balance, the oxygen permeation rate is related to the flux of oxygen vacancies by

$$-$$

Together with **Eq. 3.8-3.13**, the oxygen flux could be expressed by

$$\frac{}{}\left[\frac{(\ _e \quad _h)}{(\ _e \quad _h)}\right]\nabla$$

or in a more generalized form,

$$\frac{}{}\left[\frac{_{ion}\ \ _e}{_{ion}\ \ _e}\right]\nabla$$

where $_{ion}$ = and $_{e}$ = $_{e'}$ $_{h}$ are the partial ionic and electronic conductivity, respectively. If oxygen transport occurs through a membrane with a thickness of L under $p'O_2/p''O_2$ partial pressure gradient, the Wagner equation is derived by integrating

using the relationship ∇ $\frac{\ln}{x}$ x distance coordinate ,

$$\frac{}{\qquad}\int_{\ln}^{\ln}\frac{_{ion}\;_{e}}{_{ion}\;_{e}}\,d\ln$$

It should be noted that the oxygen partial pressures used for integration is the ones obtained at the gas phase boundaries. In the perovskite-type oxides, the electronic conductivity is much higher than the oxygen ionic conductivity [45]. The Wagner equation can thus be further simplified to

$$\frac{}{\qquad}\int_{\ln}^{\ln}\;_{ion}d\ln$$

The oxygen ionic conductivity is given by Nernst-Einstein equation,

$$_{ion}\quad\frac{_{v}}{_{m}}$$

where V_m denotes the molar volume of perovskite. It suggests that the oxygen permeation flux is dominated mainly by two factors: the oxygen vacancy concentration and the oxygen vacancy diffusion coefficient D_V.

In conclusion, the Wagner equation has been derived by assuming that local equilibrium exists between the charged species and the hypothetical neutral species in the bulk oxide. All these defects are supposed to be ideally diluted and not to interact with each other. In general, at least three species are involved in the diffusion process, including oxygen vacancies, electrons and electron holes. Each of them might be the slowest diffusing components and thus control the oxygen flux. Therefore, different equations can be derived from Wagner equation according to the actual situation.

Surface exchange reaction

If the resistance from bulk transport is less significant due to the reduction of membrane thickness or the increase in the ionic or electronic conductivity, the surface-exchange reaction would become the rate-limiting step for oxygen transport. The overall mechanism at the gas/membrane interfaces is generally described by Kröger-Vink notation as

$$_{ads}\quad\leftrightarrow\quad{}^{x}\quad h$$

Despite of this simple description in **Eq. 3.19**, the reaction of oxygen molecules with the membrane surfaces is a quite complex process. Detailed steps consist of more elementary reactions in the sequence of adsorption, dissociation, surface diffusion of intermediate species, charge transfer reaction and several incorporation steps in the interfacial zones. Virtually, various species would appear as intermediates for the adsorption of molecular oxygen [82].

Possible surface-exchange reactions may be expressed as following,

$$(g) \leftrightarrow \quad _{,ads}$$

$$_{,ads} \leftrightarrow \quad _{,ads} \ h$$

$$_{,ads} \leftrightarrow \quad _{ads} \ h$$

$$_{ads} \leftrightarrow \quad _{ads} \ h$$

$$_{ads}^{''} \quad \leftrightarrow \quad ^{x}$$

The re-oxidation of oxygen ions is assumed to follow the same steps in the reverse direction. Each of these sequential steps may limit the overall rate of oxygen transport. However, the series of elementary steps are not yet clearly understood and vary among different materials [83].

According to the surface-exchange kinetics, the thermodynamic equilibrium of charge carriers can no longer exist as assumed in Wagner's theory A space charge layer (Mott-Schottky layer) would form next to the surface extending into the interior of oxide even at equilibrium. The width of this double layer depends on the concentration of all mobile charge carriers. Thereby, the Wagner equation is not applicable in this case as surface-exchange kinetics becomes the rate-limiting step. The oxygen flux can be given by Onsager equation [84] on the assumption that near-equilibrium surface reaction is considered irrespective of the non-linear effects occurring under a high potential gradient.

$$_{ex}\left(\frac{\nabla}{\quad}\right)$$

$_{ex}$ the kinetic parameter, representing the balanced charge rate in the absence of oxygen partial pressure gradient

∇ the chemical potential drop across the interface

Hassel [85] verified the Onsager equation to express the exchange between gaseous oxygen and ionized lattice oxygen in terms of oxygen partial pressure by

$$kp^{n} \left(\frac{\nabla}{\quad}\right)$$

k	the surface-exchange rate constant, which has an Arrhenius dependence on temperature
n	the exponent for oxygen partial pressure dependence

In addition, Tabata et al. [86] described the significant differences of chemical compositions at the surface and inside the bulk of the $La_xSr_{1-x}CoO_{3-\delta}$ compounds. This also indicates a different behavior of the surface from that of the bulk in these oxides, which should be deliberated if correlating the stoichiometric composition of perovskites to the surface-exchange kinetics.

3.4 Membrane degradation

For practical application, it is not sufficient for membrane to show only high oxygen permeability, but sustainable structural stability for long period operation is also required. However, degradation seems to be unavoidable when the membrane is exposed to different gradients (e.g. electrochemical as discussed in **Chapter 3.3**). The migration of mobile charge carriers leads to three different types of membrane degradation processes [87]:

(i) kinetic demixing; i.e., the initially homogeneous multicomponent material becomes chemically inhomogeneous
(ii) kinetic decomposition; i.e., the originally single-phase material decomposes into new phases
(iii) morphology instability; i.e., the original material morphology becomes unstable and forms new one

All these kinetic processes are irreversible and the instability of material would remain even the applied potential gradient is removed. Considering the case of industrial application, such chemical instability could cause membrane failures as different volumes of unit cells may appear in these phase mixtures, which result in an accumulation of internal stresses. Furthermore, decomposition is commonly expected to degrade the oxygen fluxes, which should be avoided to ensure a continuous and constant permeation process. Thus it is important to explore the underlying reasons for membrane degradation.

According to Gibbs-Duhem equation, inverse gradients are produced in an $(A_xB_{1-x})O$ binary system for oxygen and cations respectively:

x x x ( )

These electrochemical gradients generate mobile components fluxes towards the interfacial zones of the membrane. Therefore, based on this simple model, the kinetic demixing or decomposition in oxygen transport membranes is mainly due to the different self-diffusion rates of cations driven by the chemical gradient of oxygen partial pressure pO_2 across the membrane. Obviously, the degradation kinetics is influenced by pO_2 and temperature at the same time. $SrCo_{0.8}Fe_{0.2}O_{3-\delta}$ oxide was observed to decompose in the pO_2 range of 10^{-14}-10^{-16} atm at both sides of the membranes under the reducing atmosphere [88], resulting in a three-phase mixture containing layered intergrowth Ruddlesden-Popper phases and rocksalt. It seems that the destabilization of membrane material is associated with the decreased pO_2 on the permeate side with reducing gases as this perovskite remains stable in pO_2 down to ~10^{-12} atm. The transition temperature for cubic perovskite to oxygen-ordered brownmillerite is below 800 °C. One effective method to increase the phase stability of perovskite-type $SrCo_{0.8}Fe_{0.2}O_{3-\delta}$ oxides is via partial substitution of Sr by the elements of larger ionic radius (e.g., Ba) [63] or metal ions with high valence state (e.g., La^{3+}) [89]. It is also confirmed that the temperature of order-disorder transition shifts to higher zones by replacing Fe with Cr and Cu in $SrCo_{0.8}Fe_{0.2}O_{3-\delta}$ compounds [90].

In the MIEC membranes, the cations mobility is several orders of magnitude slower than that of oxygen or electron (holes). Therefore, kinetic demixing is also considered as a time-dependent process that becomes sufficiently effective in the membrane properties only after long period operation. An accumulation of Ba along with the depletion of Fe and Co at the oxygen-lean side of the $Ba_{0.5}Sr_{0.5}Co_{0.8}Fe_{0.2}O_{3-\delta}$ membrane was detected after cyclical permeation tests within the range 700-800 °C for approximately 4 days [91]. Similarly, Shao et al. [82] found the segregation of Ba and Sr on both membrane surfaces of $Ba_{0.5}Sr_{0.5}Co_{0.8}Fe_{0.2}O_{3-\delta}$ oxides after operation at 850 °C for 1000 h. Lein et al. [92] also observed an enrichment of the fastest diffusion cations, especially Sr, at the high oxygen pressure side of the $La_{0.5}Sr_{0.5}Co_yFe_{1-y}O_{3-\delta}$ membrane at 1150 ℃ for more than ~30 days operating, while Fe was slightly enriched at the permeate side. Ge et al. [93] investigated the oxygen permeability of A-site deficient $(Ba_{0.5}Sr_{0.5})_{1-x}Co_{0.8}Fe_{0.2}$ membrane and they attributed the slow deterioration of permeation flux at 850 °C to the segregation of Ba^{2+} and Sr^{2+} over the membrane surface for 350 h operation.

Here, it is essential to emphasize that the kinetic demixing might eventually lead to the decomposition of membranes. This means the localized inhomogeneous distribution of chemical components may tend to form new phases, though the membrane might be thermodynamically stable over the whole oxygen partial pressure gradient range [94]. The phase transition of cubic BSCF perovskites into a hexagonal phase after annealing at intermediate temperatures has been widely reported [55, 82, 93, 95, 96]. The observed kinetics of phase transition is explained by significant structural rearrangements occurring upon transition and slow cation diffusion. Moreover, it is worth noting that the multi-valence metal ions could be reduced from a higher valence state to a lower one accompanied with oxygen release from the lattice. These effects including the simultaneous variation of oxygen vacancy concentration in the host perovskite might lead to the occurrence of phase transformation. Shao et al. [55] discerned a ~30% degradation of the oxygen permeation flux through the $Ba_{0.5}Sr_{0.5}Co_{0.8}Fe_{0.2}O_{3-\delta}$ membrane below 900 ℃ , which is mainly caused by the slow phase transition of cubic perovskite into a hexagonal phase. Niedrig et al. [97] pointed out that the formation of hexagonal structure occurs at temperatures below 840 °C and it should be argued that this hexagonal phase would reform to cubic perovskite at 900 °C. Švarcová et al [98] rationalized the cubic to hexagonal phase decomposition in BSCF oxides by Goldschmidt tolerance factor derived from the radii of constituent cations. They ascribed the formation of either a 2H or 4H type hexagonal structure to the oxidation of the B-site cations. In addition to the formation of hexagonal perovskite during phase transition, some other non-cubic phases were also found at intermediate temperatures in $Ba_{0.5}Sr_{0.5}Co_{0.8}Fe_{0.2}O_{3-\delta}$ oxides [96, 99]. Detailed information related to the kinetics and influencing factors of phase transition in BSCF perovskites can be referred to in the following chapters (**Chapter 5.4-5.6**).

4 Materials and Experimental methods

In the current work, the thermochemical properties and the oxygen permeation stability of BSCF materials were analysed. For the first step, the sintering behaviour of membrane materials was characterised. The thermochemical expansion and oxygen nonstoichiometry of the sintered BSCF pellets were determined by thermo-mechanical analysis (TMA) and thermogravimetric analysis (TGA), respectively. This current work mainly focuses on the evaluation of oxygen permeation stability of dense BSCF membranes after long-term operation (up to 2000 h) at intermediate temperatures (700-900 °C). The oxygen fluxes through the membranes were recorded as a function of temperature and time. The microstructural properties of the degraded membranes and pellets were assessed by scanning electron microscope equipped with energy-dispersive X-ray spectroscopy (SEM/EDX) and electron backscatter diffraction analysis (EBSD). Phase compounds and their fractions in the used samples were determined by X-ray diffraction analysis (XRD).

4.1 Materials selection and production

4.1.1 Perovskite-structured $Ba_xSr_{1-x}Co_yFe_{1-y}O_{3-\delta}$ (BSCF)

In order to select suitable materials for oxygen separation, at least two aspects should be considered, i.e. membranes must exhibit both high oxygen permeation rate and sufficient thermochemical stability under oxyfuel condition. From the structural configuration point of view, perovskite-type $SrCoO_{3-\delta}$ has been expected to possess superior oxygen permeability, which could be ascribed to its high concentration of oxygen vacancies in the lattice as well as the relatively weak strength of Co-O bond [57, 100, 101]. However, this material is quite unstable and becomes oxygen non-permeable by forming complex secondary phases at lower temperatures (< 900 °C) [90, 102]. Thereafter, a solution was adopted by substituting a small amount of Fe for Co, since the Fe component was found necessary to preserve the perovskite structure at high Sr contents [103]. The perovskite-type $Ba_xSr_{1-x}Co_yFe_{1-y}O_{3-\delta}$ (BSCF) system was primarily developed based on $SrCo_yFe_{1-y}O_{3-\delta}$ (SCF) with the aim of improving its chemical and structural stability, as the perovskite phase of SCF is thermodynamically stable only at high temperature (> 790 °C) and high oxygen pressures (> 0.1 atm) [104]. Otherwise, a two-phase region composed of perovskite and brownmillerite emerges in the bulk of SCF material, which is detrimental to the oxygen permeability of membranes. Shao et al. found that the proper substitution by larger barium ions in SCF perovskite could greatly improve the phase stability of this material while reserves its high oxygen permeation flux [55], compared to the case of lanthanum substitution [45, 90]. Alaee et al. [105] studied the effect of Ba content and operating conditions on the oxygen permeability of BSCF membranes. In addition, the iron doping concentration was reported to have a significant effect on the lattice constant, oxygen nonstoichiometry and electrical conductivity of BSCF oxides [32].

Compared to the alternative (La,Sr)(Co,Fe)$O_{3-\delta}$ (LSCF) perovskites, BSCF materials show considerable higher lattice constants [64, 106] and lower oxygen migration energy (0.5 eV for BSCF [59, 70, 107] and 0.8-0.9 eV for LSCF [108]). The high oxygen permeation flux of BSCF membranes is simply owing to its large oxygen deficiency (see **Tab. 3.1**) and structural stability without the formation of ordered oxygen vacancy superstructures.

On the other hand, BSCF membranes have two main drawbacks including high thermal expansion coefficient (TEC) and relatively low chemical stability. A TEC value of $\sim 24\times10^{-6}$ K^{-1} was reported for $Ba_{0.5}Sr_{0.5}Co_{0.8}Fe_{0.2}O_{3-\delta}$ oxides at a pO_2 of 0.01 atm in the temperature region of 600-900 ℃ [64]. Comparably, the TEC of $La_{0.8}Sr_{0.2}FeO_{3-\delta}$ is reported to be only 12.6×10^{-6} K^{-1} or 20.7×10^{-6} K^{-1} for $La_{0.8}Sr_{0.2}Co_{0.8}Fe_{0.2}O_{3-\delta}$ at 900 °C [100]. The oxygen permeation behaviour of BSCF membranes has been extensively investigated [53, 55, 59, 82, 91, 109, 110]. Though phase decomposition or phase transition might occur in BSCF membranes at low temperatures, a steady oxygen flux through $Ba_{0.5}Sr_{0.5}Co_{0.8}Fe_{0.2}O_{3-\delta}$ membranes was obtained at temperatures above 850 ℃ [55, 111], confirming its potential as an oxygen generator in the high temperature region. Therefore, the long-term permeation stability and phase transition kinetics in BSCF materials are of great interest concerning their application in the oxyfuel process.

4.1.2 Powder production

In the present work, perovskite BSCF materials with A- or/and B-site substitution by different amounts of metal ions were selected for investigation. The stoichiometric compositions of membrane materials are listed in **Tab. 4.1**. All these BSCF powders were synthesized by the solid-state reaction method, except BSCF5582 (provided by Treibacher Industrie AG, Austria).

The raw materials ($BaCO_3$, $SrCO_3$, $CoCO_3$, Fe_2O_3) for the BSCF powder production were weighted and mixed according to their weight ratios in the stoichiometric formula. These powder mixtures were then calcined in alumina crucibles in several steps. Between each step, the product was milled (agate mortar) manually for better interaction among particles in order to prompt the formation of perovskite oxides during calcination. After producing the single-phase BSCF, a large number of agglomerates were present in the freshly prepared powder, which may be caused by the bridging effect of strong polar groups contained in the powder precursors [112]. The coarse powder (D50 > m was then wet milled by tumbling with zirconium oxide Zr $_2$) balls (d = 3- mm, m ≈ g in ethanol ml in a ball mill (Typ M 80, Alfred Schwinherr KG, Germany) for 24-48 h. The refined BSCF powders (D50 ≈ m were subsequently separated from the suspension after the evaporation of ethanol and then ground into the final products in a mortar. The information about powder production from the raw materials and the corresponding calcination parameters is illustrated in **Appendix A**.

Tab. 4.1 Chemical formula and abbreviation of the selected $Ba_xSr_{1-x}Co_yFe_{1-y}O_{3-\delta}$ materials

Series	Chemical formula	Abbreviation
$Ba_xSr_{1-x}Co_{0.2}Fe_{0.8}O_{3-\delta}$ (x = 0.2-0.8)	$Ba_{0.2}Sr_{0.8}Co_{0.2}Fe_{0.8}O_{3-\delta}$	BSCF2828
	$Ba_{0.4}Sr_{0.6}Co_{0.2}Fe_{0.8}O_{3-\delta}$	BSCF4628
	$Ba_{0.5}Sr_{0.5}Co_{0.2}Fe_{0.8}O_{3-\delta}$	BSCF5528
	$Ba_{0.6}Sr_{0.4}Co_{0.2}Fe_{0.8}O_{3-\delta}$	BSCF6428
	$Ba_{0.7}Sr_{0.3}Co_{0.2}Fe_{0.8}O_{3-\delta}$	BSCF7328
$Ba_xSr_{1-x}Co_{0.8}Fe_{0.2}O_{3-\delta}$ (x =0.2-0.8)	$Ba_{0.2}Sr_{0.8}Co_{0.8}Fe_{0.2}O_{3-\delta}$	BSCF2882
	$Ba_{0.4}Sr_{0.6}Co_{0.8}Fe_{0.2}O_{3-\delta}$	BSCF4682
	$Ba_{0.5}Sr_{0.5}Co_{0.8}Fe_{0.2}O_{3-\delta}$	BSCF5582
	$Ba_{0.6}Sr_{0.4}Co_{0.8}Fe_{0.2}O_{3-\delta}$	BSCF6482
	$Ba_{0.7}Sr_{0.3}Co_{0.8}Fe_{0.2}O_{3-\delta}$	BSCF7382

4.1.3 Uni-axial dry pressing and sintering process

$Ba_xSr_{1-x}Co_yFe_{1-y}O_{3-\delta}$ (BSCF), except $Ba_{0.5}Sr_{0.5}Co_{0.8}Fe_{0.2}O_{3-\delta}$

Disk-shaped BSCF membranes of 20 mm in diameter (~2.3 g powder) were prepared by uni-axial pressing under an isostatic pressure of 125 MPa. While, pellets of 8 mm in diameter (~0.4 g powder) were formed in the same way as membranes with identical pressure. The major steps for dry pressing are listed in **Appendix B**. Before pressing, the BSCF powder was mixed with 1% carboxymethyl cellulose (CMC) solution (CMC:H_2O = 1 g:100 ml) as binder to increase the cohesive bonding strength between particles. The mixture was then dried on a magnetic stirrer (RCT basic, IKA®, Germany) at 75 °C for a period of 10 min. The pressing sequences were completed twice for each sample, i.e., the shaped pellets/membranes after first pressing were crushed and milled into powder for the second process. The reason for this double pressing is based on the consideration of crushing the large agglomerates into fine particles and thus homogenising the particle sizes of powders by high isostatic pressure during the first pressing. The refined powders could facilitate the sintering process and lower the possibility of cracks formation in the sintered samples, which in many cases, is caused by the presence of particularly large agglomerates. The die-pressed green disks were sintered in ambient air, firstly from RT to 300 °C by a slow heating rate of 2 K/min for the CMC binder to evaporate tardily and completely from the sample. Then disks were further heated up by 5 K/min to 700 ℃ and then slowly heated with 2 K/min again till reaching the sintering temperature. A cooling rate of 2 K/min was used in this study. Prior to any subsequent experiments, both sides of the sintered pellets/membranes were polished with silicon carbide abrasive paper (P1200) to ensure geometrically flat surfaces. The relative density of each sample was determined by an analytical and precision balance (XP204, Mettler-Toledo AG, Switzerland; readability: 0.1 mg) using the Archimedes method in ethanol. Only these samples with a relative density higher than 90% were used in this work.

$Ba_{0.5}Sr_{0.5}Co_{0.8}Fe_{0.2}O_{3-\delta}$

The $Ba_{0.5}Sr_{0.5}Co_{0.8}Fe_{0.2}O_{3-\delta}$ membranes were produced by Institute for Energy and Climate Research 1 (IEK-1), Forschungszentrum Jülich GmbH. An isostatic pressure of 105 MPa was utilized for uniaxial pressing and membranes were formed with a diameter of 20 mm. The pressed green disks were sintered at 1000 ℃ for 10 h in static air with a heating/cooling rate of 5 K/min. The surfaces of the membrane samples were polished (P1200) and their relative densities were measured in the same way as other BSCF membranes.

4.2 Methods for materials characterization

4.2.1 Differential thermal analysis (DTA)

Differential thermal analysis (DTA) was performed to identify and quantitatively analyse the thermal reactions occurring in substances by recording the temperature difference between the substances and a reference standard under identical thermal conditions. In this study, the calcination and melting temperature of BSCF powders were analysed by a high resolution thermal analysis device (STA 449C Jupiter, Netzsch GmbH, Germany) combined with thermogravimetry (TG) in synthetic air atmosphere (N_2:O_2 vol %: vol % he resolution of G is g for the balance and < 1 W for the DSC signal. Before any DTA/TG analysis of the BSCF samples, the system has to be calibrated by recording the difference of an empty crucible compared to the reference through a monitored temperature program. In this way, the measured signals of BSCF samples become independent of the crucible and the reference.

Determination of calcination temperature for powder production

The calcination temperature of each stoichiometric powder mixture was determined for the synthesis of perovskite BSCF by solid-state reaction. A small amount of raw powder mixture (~150 mg) was added in an alumina crucible (Netzsch GmbH, Germany). Then the temperature and mass variations in this substance crucible versus an alumina reference were measured by DTA/TG. The temperatures for DTA analysis were determined on the basis of published calcination parameters for BSCF powder synthesis via solid-state reaction route [58, 99, 110, 113]. The system was heated up accordingly to maximum 1150 ℃ with a heating rate of 3 K/min. A continuous flow of gas mixture consisting of synthetic air (flow rate: 25 Nml/min) and helium (protective gas; flow rate: 25 Nml/min) was supplied in the whole process. After the measurements, the calcination temperature of the powder mixture was determined by normalized DTA/TG curves, where a sharp endothermic peak arises along with the sample mass approaching constant, as depicted in **Appendix A**.

Determination of melting temperature

In addition to the determination of calcination temperature for powder synthesis, the melting temperature of BSCF materials could also be measured by means of DTA/TG.

In order to avoid possible interactions between the BSCF substances and the alumina crucibles, the calcined powder (~100 mg) was added in a Pt/Ir sample pan (Netzsch GmbH, Germany) and another empty pan was used as the reference. The powder sample was heated by 3 K/min up to maximum 1500 ℃ , depending on the composition of the BSCF materials. A synthetic air flow of 25 Nml/min together with helium gas of the same flow rate was provided during the measurements. The melting temperature of BSCF powder could be determined directly from the DTA-signal curve as the onset point of the endothermic melting process. In the meantime, an exothermic peak should appear around this melting temperature during cooling, which is related to the crystallization process in materials. The measured DTA/TG curves for the determination of the melting temperatures of BSCF membrane materials are illustrated in **Appendix C**.

4.2.2 Thermomechanical analysis (TMA)

Many materials undergo variations of their thermomechanical properties upon heating or cooling. The dimensional change of a sample against monitored temperature (and/or time) under a constant non-oscillating stress was measured by the thermo-mechanical analyser (TMA). In this way, sample properties, such as sintering behaviour, linear thermal expansion coefficient (TEC), material anisotropy, softening temperatures and glass transition point, can be determined. A vertical high-performance TMA (Setsys Evolution, Setaram, France; resolution: 0.2 nm) was used in this study to record the sintering process and thermochemical expansion behaviour of BSCF membrane materials. A constant synthetic air flow was provided for all experiments at a flow rate of 20 Nml/min and argon was utilized as the protective gas. Before each measurement, the dimensional change of the system according to the settled temperature program was recorded, using sapphire (TEC = $(5.0\text{-}6.6)\times10^{-6}$ K^{-1}) as the reference sample. By comparing the TMA data of BSCF materials with that from the measurement with sapphire, the thermal behaviour of the equipment would be excluded by the associated software. Thereby, the actual dimensional change of samples as a function of temperature and time only is clearly presented.

Sintering behaviour of membrane materials

In order to produce a gas-tight pellet/membrane, the sintering behaviour of BSCF powders should be analysed he samples of pressed green pellets d mm; m ≈ g were heated up by 6 K/min to a temperature of maximum 1200 °C whilst the system was kept at this temperature for a period of 30 min. A mechanical pressure of 5 g was exerted on the sample to get rid of the external vibration interference and a measuring range of m was selected rom the measured M data, the linear shrinkage ε of sample can be calculated by

$$\varepsilon(\ ) \quad \frac{(\ )}{} \quad \frac{(\ )}{}$$

the change of sample length L(T) at temperature T

L_0 sample initial length L_0

Similarly, the shrinkage rate of sample $\dot{\varepsilon}(\ )$ was achieved by deriving the shrinkage ε to time t,

$$\dot{\varepsilon}(\ ) \quad \frac{d\varepsilon(\ )}{dt} \quad \frac{d}{dt}\left[\frac{(\ )}{}\right]$$

Based on calculation, the shrinkage curves as well as the change of shrinkage rates in BSCF samples could hereby be obtained by TMA as a function of temperature and dwelling time. Combining both curves, the sintering parameters were determined accordingly for each BSCF material.

Thermochemical expansion of membrane materials

The thermal and chemical expansion behaviours of BSCF materials were characterized by means of TMA as well. Samples were measured under the same mechanical load of g a nd a measuring range of m was selected for precise analysis. According to the linear dimensional change of the sample ε upon heating from initial temperature $_0$ till respective temperature , the thermochemical expansion coefficient α could be expressed by

$$\alpha(\ ) \quad \frac{\varepsilon(\ )}{} \quad \frac{}{} \left[\frac{(\ )}{}\right]$$

The dimensional change of sintered pellets (d ≈ 6.5 mm, h = 2.0-2.5 mm) in the temperature range of 40 °C to 1050 °C was recorded. The system was first heated up fast to 1050 °C at a heating rate of 15 K/min and kept at this temperature for a period of

20 h. After this long period dwelling, samples are assumed to achieve thermodynamic equilibrium. Afterwards, a slow cooling process with a rate of 1 K/min was conducted to the onset temperature of 40 ℃ to reserve the equilibrium status in the samples. After dwelling at 40 ℃ for 1 h, the system was heated up again at a rate of 3 K/min till the final 1050 ℃ . The TEC values of BSCF materials were calculated according to the measured TMA data of this heating period.

4.2.3 Thermogravimetric analysis (TGA)

Thermogravimetric analysis (TGA) is commonly used to measure the weight changes in a material in relation to temperature (or time) under a controlled atmosphere. The analyser consists of a highly sensitive microbalance with one pan loaded with the sample and the other kept empty as a reference. Measuring the mass change of samples under different conditions allows us to predict the thermal stability, decomposition kinetics, the moisture and volatiles contents as well as the influence of reactive or corrosive atmospheres on materials.

In the current work, the variation of oxygen stoichiometry δ as a function of temperature in BSCF materials was determined by a high-precision symmetrical TGA G , Setaram, rance; resolution: ± g he sintered pellets $m_0 = 0.25\text{-}0.35$ g) were measured in synthetic air at a flow rate of 100 Nml/min. Argon was supplied as protective gas. Before heating, the microbalance with the sample pellet in a crucible on one side and an empty crucible as the reference on the other was adjusted till balancing. Samples were first heated up to 1000 °C at a rate of 2 K/min and kept for 4 h to achieve thermodynamic equilibrium in the materials. Afterwards, the system was cooled down by 50 ℃ for each step at a cooling rate of 2 K/min and dwelled for 2 h at each temperature till 750 ℃ . hus the δ values of the samples were precisely determined in the temperature region of 750-1000 °C. Then samples were fast cooled down to room temperature by 10 K/min.

According to the measured TGA data, the change of oxygen stoichiometry of materials δ could be obtained by

$$\delta(\ ) \quad \left[\frac{m}{m_{S\ ,}}\right]\left(\frac{M_{S}}{M}\right)$$

m the mass change of the sample at T

$m_{S\ ,}$ sample weight at room temperature

M_S	molar mass of BSCF material
M	molar mass of oxygen

4.2.4 X-ray diffraction analysis (XRD)

X-ray diffraction analysis (XRD) was performed to identify the crystalline structure and phase composition of materials by the diffraction pattern of their atomic lattices. Electrons are produced firstly by heating a filament in a cathode ray tube. Then X-rays could be generated by accelerating these emitted electrons toward a target under an applied voltage and bombarding the target with electrons to produce the characteristic X-ray spectra of the target material. The most common spectra are K_α and K_β with K_α consisting of K_α and K_α in part. In order to produce monochromatic X-rays (typically K_α) for diffraction, filtering by foils or crystal monochrometers is required. During XRD analysis, these monochromatic X-rays are collimated and directed onto the sample. As both the sample and the detector are rotated, the intensity of the reflected X-rays is recorded and finally converted to a count rate as the output in a computer monitor. Diffraction effects could be observed in the form of peaks in intensity, when the geometry of the incident X-rays impinging the periodic structures of samples satisfies the Bragg equation.

$$n \quad d_{hkl} \sin \tag{4.5}$$

n	an integer
	wavelength of X-rays
d_{hkl}	interfacial distance of (hkl) plane
sin	incident angle of X-rays

The structural properties of BSCF materials were examined at room temperature by a diffractometer (D4 Endeavor, Bruker-AXS GmbH, Germany) using Cu K_α radiation. Diffraction patterns of the samples in the angle range of 0° < 2 < 162° were recorded. From the measured patterns, the phase structure and composition of BSCF materials including the respective lattice parameter(s) can be determined. In the case of BSCF powder production, the diffraction patterns of the as-calcined products were detected and analysed by XRD. From the recorded data, the unit cell volume of each stoichiometric sample could be deduced from the lattice parameter(s) of the perovskites.

Assuming an ideal perovskite structure at room temperature $\delta = 0$), the theoretical density of BSCF powder was calculated by

$$_{\text{theo}} \quad \frac{n}{\quad} \; \frac{M\ _{S}}{\quad\quad} \qquad (\quad)$$

n	number of formula units in the unit-cell
M_{BSCF}	molar mass of BSCF material
N_A	Avogadro's constant
V	unit cell volume

BSCF pellets or membranes after long-term operation were analysed by XRD as well. Thereafter, phase formation or decomposition at both sides of the samples could be detected and characterized. Part of the used samples were crushed into powder for XRD analysis to examine their overall diffraction patterns. The volumetric fraction of secondary phases in the powder samples could be computed from these overall patterns by the associated software.

4.2.5 Scanning electron microscopy (SEM)

Scanning electron microscopy (SEM) can provide high magnification images of solid materials due to its great depth of field. A beam of high-energy electrons is generated by an electron gun, typically a tungsten filament or a field emission gun. This electron beam is accelerated towards a system of apertures and electromagnetic lenses of the column through a high voltage (e.g., 20 kV) and focused at the surface of a specimen. During systematically scanning in a raster scan pattern, the interaction of the beam with specimen surface induces a signal that could be sensed by the detector. The detected signal varies as the beam is sequentially scanned over the consecutive points of the specimen. This variation of sensed intensity is then recorded and it produces a gray-scale image in the computer.

In the current work, the morphology features of the sintered pellets and membranes were characterized by SEM (Supra50VP, Carl Zeiss NTS GmbH, Germany) equipped with an energy dispersive X-ray (EDX) attachment (SDD-Detector, Oxford Instruments, UK) to identify the elemental composition of phases. Secondary phases formed in the membranes after long-term permeation tests were also identified by an electron backscatter diffraction (EBSD) detector (HKL, Oxford Instruments, UK). To image the surface or cross-section morphology without charging effects, samples were coated in vacuum with platinum using a sputter coater.

4.3 Determination of membrane permeability

4.3.1 Setup of permeation tests

The permeation tests consist of three main components: the gas supply unit, the test unit and the analytical unit. Various gases could be mixed or supplied separately for the permeation tests, including compressed air, O_2, N_2, Ar and He. In this study, the gas flow at both sides of the membrane was regulated by mass flow controllers (WMR, Brooks Instrument, Netherlands) with the measuring range of 20-1000 Nml/min. These controllers were regularly calibrated by a volumetric precision gas flow meter (DryCal Defender 500 Series, Bios International, USA).

A three-zone horizontal furnace (ThermoStar, Germany; T_{max} = 1200 °C) was built for the investigation of the long-term permeation stability of BSCF membranes. The operation temperature in the furnace was controlled by a microprocessor temperature controller to keep within ±1 ℃ of the set points. A K-type thermoelement was inserted near to the membrane in the recipient to regulate the furnace heating power. The recipient for the measurements is required to sustain high temperatures up to 1000 °C and thus quartz glass was selected here. The permeator unit is schematically presented in **Fig. 4.1**. Series of BSCF membranes with different membrane thickness (d = 15 mm, h = 1.0/2.0/2.5 mm) were produced for the long-term permeation measurements at intermediate temperatures. The sintered and polished membrane was sealed with two gold gaskets of 1 mm in thickness between the quartz glass tubes in the permeator to avoid leakage and radial contribution to the oxygen permeation flux. To ensure the gas-tightness of the recipient, a spring load system was used to introduce an external pressure onto the glass tube and therewith also to the gold seal. Afterwards, the whole assembly for permeation tests was mounted into the tubular furnace and heated up to 1000 °C, which is close to the melting point of gold ($T_{m,\,Au}$ =1064.18 °C), for further gastight sealing. The inlet gas at the so-called feed side of the BSCF membrane was synthetic air and pure helium was supplied to the other side, termed as sweep gas. The connection between the gas supply unit and the recipient was also tightly sealed. The retentate gas comprised of feed gas and nitrogen that could not permeate through the membrane was exhausted into the vent. In order to analyze the gas composition at the sweep side of the membrane during operation, the permeate gas flowing together with sweep gas was directed into a gas mouse which was connected to the permeate outlet of the reactor. Thus the effluent gas could be gathered by simply shutting off the valves at both entrances of the gas mouse to enclose the required gas inside. Moreover, this gas mouse was designed to be easily removable from the permeator and it could be taken along for the following analysis. After each measurement, the gas mouse was reconnected to the permeator again with both valves open in order that the effluent could pass through.

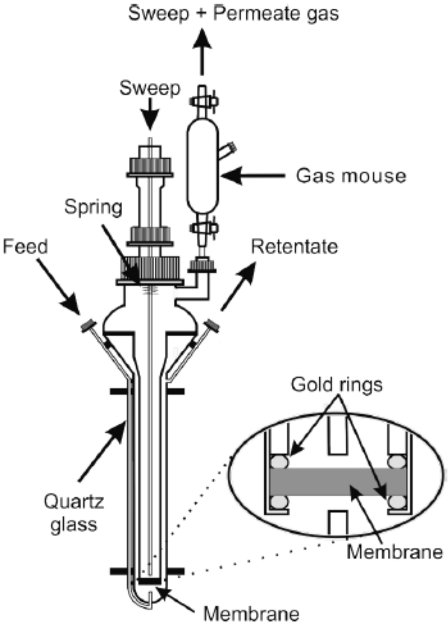

Fig. 4.1 Principle and setup of the oxygen permeator

Prior to any analysis, the operation time and the instant temperature in the furnace were recorded. The gas mouse filled up with effluent gas was connected to a gas chromatograph (7890A GC System, Agilent Technologies, USA) for gas composition analysis shortly after removing it from the recipient. In this way, the gathered gas composition was assumed unchangeable over this period. The oxygen permeation rate of membranes could be calculated by the concentration of the permeate oxygen , the permeate flow $_{permeate}$ and the effective membrane area A using this equation, permeate

Consequently, the variation of oxygen permeability of BSCF membranes in accordance with operation temperature and time was achieved. It has to be mentioned here that the reference gas for the thermal conductivity detector in the GC consists of argon, giving the possibility for the selection of helium as sweep gas in this study. The flow chart for the oxygen permeation measurement is schematically depicted in **Fig. 4.2**.

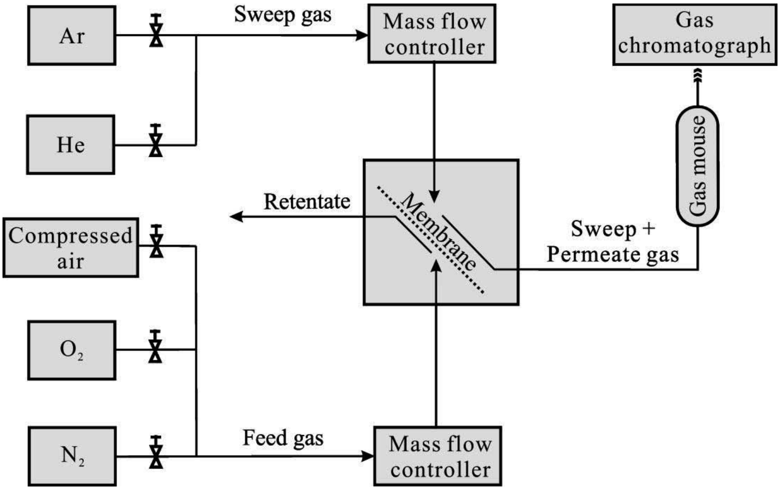

Fig. 4.2 Schematic diagram of the overall assembly for oxygen permeation measurement

4.3.2 Performance of oxygen permeation measurements

The feed gas flow of synthetic air was supplied steadily at a rate of 120 Nml/min and the helium flow was kept at 40 Nml/min at the permeate side of BSCF membranes. Under this condition, an oxygen partial pressure gradient was generated across the membrane, acting as the driving force for the oxygen permeation process. Membranes held by two gold gaskets in the recipient were firstly heated in the furnace to 1000 ℃ and dwelled for 6 h. During this period, the gold rings become softened and deformed under the compressed spring load to fill up the openings between the tubes and the membrane. After 6 h dwelling, the membrane was found to be almost sealed off leakage and only a small amount of nitrogen was detected in the permeate effluent by GC. The content of nitrogen in the permeate gas reveals the assembly gas leakage and its concentration was measured as less than 5% of the total permeation flux for all the measurements. After confirming the gas-tightness of the reactor, membranes were cooled down slowly in the furnace by 5 K/min to the respective experimental temperature.

Membranes of 1.0/2.5 mm thickness were dwelled at 800 ℃ for 2000 h under the air/He pressure gradient. The other series of membranes with a thickness of 2.0 mm were dwelled at 850 °C for 2000 h or kept in a temperature regime of 700-900 °C for cyclic permeation measurements. Materials and their corresponding operation conditions are summarized in **Tab. 4.2**. The oxygen permeation fluxes of BSCF membranes were recorded every 24 h during the experimental period.

Tab. 4.2 Membranes for long-term and cyclic permeation tests under different conditions

Experiments	Materials	Thickness / mm	Temperature / ℃	Dwelling time / h
Long-term permeation	BSCF4628	2.0	850	2000
	BSCF6482	2.0	850	2000
	BSCF5582	1.0	800	2000
	BSCF4682	2.5	800	2000
	BSCF5582	2.5	800	2000
	BSCF6482	2.5	800	2000
Cyclic permeation	BSCF5582	2.0	700-900	-
	BSCF6482*	2.0	700-900	-

* The BSCF 6482 membrane was further imposed to the cyclic condition after operating at 800 °C in the long-term permeation test for 2000 h.

Due to the existence of unavoidable gas leakage in the system, the measured oxygen concentration ($_{\text{, sweep}}$) of effluent in the gas mouse was composed of two parts: the leaked oxygen and the permeate oxygen. The leaked oxygen concentration could be associated with the detected nitrogen trace ($_{\text{, sweep}}$), assuming their concentrations ratio is same to that as in the feed air, i.e., $_{\text{, feed}}$: $_{\text{, feed}}$ = 4:1. The permeate flux $_{\text{permeate}}$ in **Eq. 4.7** is replaced here by the flow rate of the sweep gas $_{\text{sweep}}$, the value of which is thereby enlarged due to the presence of permeate oxygen and the leakage in the effluent. The oxygen permeation flux through BSCF membranes was calculated by subtracting the leaked oxygen concentration from the measured one using this equation

$$-\left(\quad _{\text{, sweep}} \qquad _{\text{, sweep}} \frac{_{\text{, feed}}}{_{\text{, feed}}} \right) \frac{_{\text{sweep}}}{\left(\quad _{\text{, sweep}} \qquad _{\text{, sweep}} \right)}$$

The effective membrane area here denotes the surface region which is responsible for the oxygen transport process. As membranes of 15 mm in diameter were sealed by gold rings in the recipient, the A value was determined by measuring the diameter of the uncovered membrane surface with a micrometer and the effective area of the membrane is 130 mm^2 for all the calculations.

The recipient was cooled down by 5 K/min to room temperature after long-term operation and the used samples were removed from the reactor and prepared for XRD, SEM/EDX and EBSD analysis.

4.4 Thermal stability evaluation of membrane materials

In the oxyfuel process, membranes are used for long-term operation at intermediate temperatures. During this period, kinetic decomposition or phase transition might occur in materials and results in their properties degradation, or more seriously, even the failure of membranes. To evaluate the phase stability of BSCF materials in this study, two sintered pellets d ≈ mm, h -2.5 mm) with polished flat surfaces for each material were annealed concurrently in a three-zone tubular furnace (Prüfer GmbH, Germany). The schematic chart of the long-term stability experiments is represented in **Fig. 4.3**.

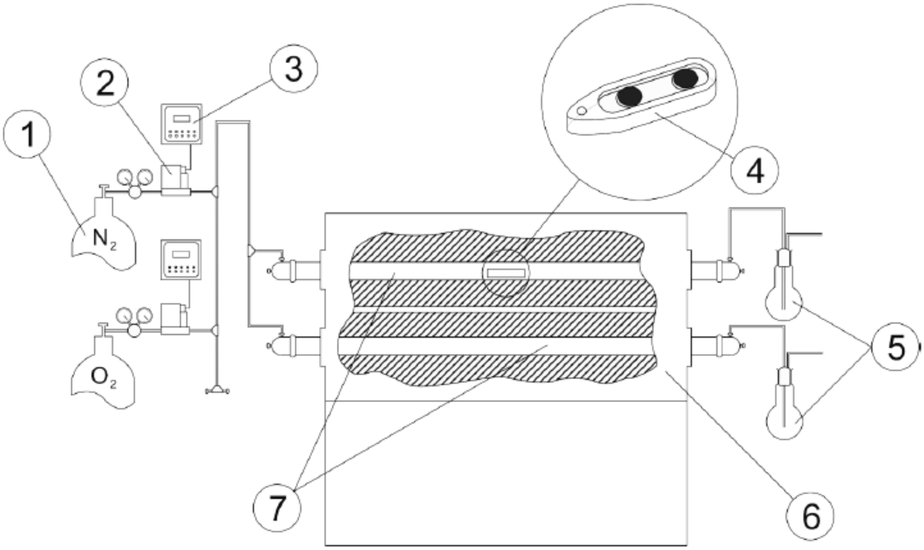

Fig. 4.3 The schematic diagram of long-term annealing experiments. This setup primarily consists of 1) gas supply; 2) the mass flow meters; 3) the mass flow controllers; 4) pellet samples in the alumina crucibles; 5) round-bottom flasks; 6) the three-zone tubular furnace and 7) quartz glass tubes.

In order to compare with the membranes for long-term permeation measurements, pellet samples were annealed in synthetic air atmosphere at 800 °C and 850 °C respectively.

The gas flow of oxygen and nitrogen was regulated separately by the mass flow meters (WMR, Brooks Instrument, Netherlands) in a range of 0-3000 Nml/min. Then both gases were mixed together as the air supply. The total flux of synthetic air for the experiments was kept at a rate of 50 Nml/min. After flowing through this horizontal furnace towards the outlet, gases were cooled down to room temperature and exhausted through a round-bottom flask.

The pellets were placed in a boat-shaped alumina pan, which was then settled in the middle of the furnace. Afterwards, the system was sealed so that only synthetic air was allowed to get through. The whole assembly was heated up by 8 K/min to 800 °C or 850 °C and dwelled for 100-1000 h respectively. The annealed samples were then cooled down to room temperature and prepared for XRD and SEM/EDX analysis. The BSCF materials along with their operation conditions for long-term stability measurements are listed in **Tab. 4.3**.

Tab. 4.3 Annealing conditions for BSCF membrane materials

Materials	Annealing temperature / ℃	Dwelling time / h
BSCF2828	850	100, 200, 500
BSCF4628		100, 200, 500
BSCF4682	800	200, 500, 1000
BSCF5582		200, 500, 1000
BSCF6482		200, 500, 1000

5 Results and discussion

5.1 Characterization of membrane materials

The structural stabilities of perovskite BSCF materials are predicted by Goldschmidt's tolerance factor, as elaborated in **Chapter 3.2.1**. In the framework of this study, the variation of tolerance factors with A- and B-site cation concentrations as well as oxygen deficit in the BSCF perovskites was determined. The BSCF powders used in the present work were synthesized by solid-state reaction. Powder materials as precursors for membranes production are required to possess single-phase perovskite structure and accurate chemical composition according to their stoichiometric formula. The influence of chemical composition on the properties of BSCF powders is declared in this chapter. An important parameter for determining the sintering or densification behaviour of powder materials is the particle size distribution. Therefore, the particle sizes of the refined BSCF powders were analysed in this work.

5.1.1 Prediction of structural stability of perovskite oxides

Ideal perovskites of the type ABO_3 are based on a cubic close packing of AO_3 with B cations in octahedral positions. Deviations from the cubic symmetry can be described in terms of Goldschmidt tolerance factor τ, which indicates the compatibility of perovskite structure with a given group of ions. he τ value of BSCF was calculated according to the ionic radii of the involved components. To simplify this calculation, all the A- and B-site cations are assumed to pack as a cubic perovskite structure of hard spheres. The average ionic radii of multivalence B cations were figured out under the premises that each component is in the high-spin state and contributes equally to the total valence of B-site cations. Oxygen vacancies in the perovskites are presumed to have the same size as oxygen ions. Moreover, it is supposed that the creation of oxygen vacancies would not reduce the coordination number of ions which causes a reduction of the calculated ionic radii. The average ionic radii of B-site cations were calculated according to [114] and the radii of components in BSCF perovskites are summarized in **Appendix D**.

In the perovskite BSCF system, the A-site cations (Ba/Sr) are in the valence state of +2, while the transition metal ions Co and Fe in the B-site could possess multiple valences.

The valence state of Co/Fe ions ranges from +2 to +4 in the ambient atmosphere. As oxygen ions have a comparable size to Ba^{2+} and Sr^{2+} [68], the perovskite structure of BSCF should resemble the cubic close packing of Ba^{2+} and Sr^{2+} with O^{2-}. With increasing temperature, oxygen releases from the lattice. This induces the reduction of B-site metal ions from a higher valence to a lower one and results in a concomitant increase of oxygen nonstoichiometry in the structure. Accordingly, the average ionic radii of B-site cations increase with oxygen nonstoichiometry, imposing a direct effect on the Goldschmidt tolerance factor. Or more generally, all the factors that influence the oxygen stoichiometry of perovskites could affect the value of τ, such as the chemical composition of materials, temperature, partial pressure gradient, reducing atmosphere, etc..

The Goldschmidt tolerance factors of the BSCF perovskites as a function of oxygen stoichiometry are illustrated in **Fig. 5.1**. Considering some exceptionally large values of oxygen nonstoichiometry were observed in BSCF materials (e.g., $\delta = 0.81$ in BSCF5582 [64]), the tolerance factor was calculated with the δ value varying from 0.0 to 1.0. According to Goldschmidt [35], the tolerance factors of most cubic perovskites should be in the range of 0.8-0.9 (shown as the dotted line in **Fig. 5.1**). It is clear that none of the BSCF materials fulfil this criterion. The inflection point in the diagrams, representing the slope change at $\delta = 0.5$, is caused by the jump in the ionic radii of B-site cations when they change from high valence states of +3 or +4 to the lower +2 or +3. Most τ values of the BSCF perovskites exceed the recommended limit of a stable structure ($0.75 \leq \tau \leq 1.00$ [37]; shown as the solid line in **Fig. 5.1**) with the nonstoichiometry δ less than 0.6 his higher tolerance factor $\tau \geq 1.0$ implies that A-site cations (Ba^{2+} and Sr^{2+}) are too large to fit into the interstitials of the cubic phase and thus hexagonal perovskite with near hexagonal close-packed layers of the A cations and O^{2-} anions is preferred. It was reported that oxygen vacancy could affect the form of octahedral network [115]. Under the extreme condition of $\delta = 0.9$-1.0, all the BSCF materials show tolerance factors below 1.0, which denotes stable perovskite structure. In this case, the average radii of B cations match the size of the octahedral interstitial sites formed by oxygen ions to constitute the BO_6 unit without large tilting. he τ values of all the BSCF materials decline with oxygen nonstoichiometry. This means the formation of oxygen vacancies in the lattice would stabilize the cubic perovskite structure. As the tolerance factor approaches the threshold of 1.0 due to the increased nonstoichiometry, the perovskite exhibits high stabilization energy, giving a reason for the stable cubic structure instead of hexagonal at high temperatures [82, 97]. With increasing the oxygen nonstoichiometry, BSCF2828 is the first to cross the boundary of $\tau = 1.0$ with the δ value larger than 0.5. Comparably, the tolerance factors of BSCF7382 stay still above 1.0 when δ reaches a high value of 0.8, indicating the large distortion of perovskite lattice in this material.

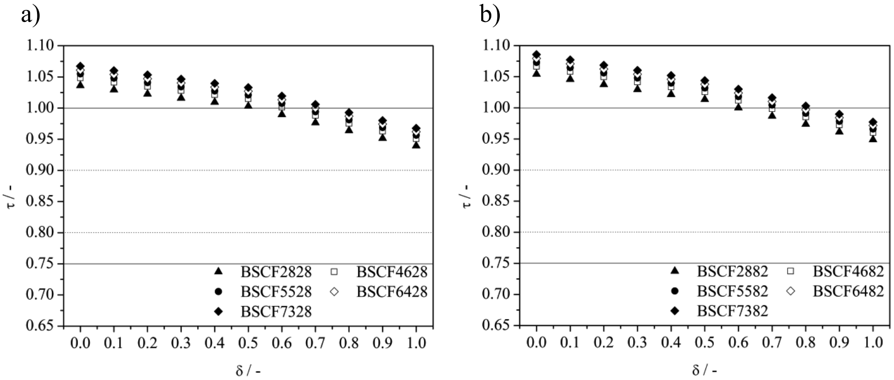

Fig. 5.1 The calculated Goldschmidt tolerance factor as a function of oxygen nonstoichiometry in BSCF materials (solid line: commonly recommended range of stable perovskite; dotted line: the range according to Goldschmidt)

The nonstoichiometry dependent τ values of BSCF materials with different chemical compositions are displayed in **Fig. 5.2**. In both series of BSCF perovskites, the tolerance factors increase with the concentration of Ba as well as the oxygen stoichiometry. The highest τ value of was found in the Ba- and Co-rich material BSCF7382. This increment of τ value with a content could be attributed to the larger ionic size of barium (r_a) compared to that of strontium (r_{Sr}) which yields the increased average ionic radii of A-site cations in BSCF. From the structural configuration point of view, the introduction of larger size Ba^{2+} into the perovskite could cause considerable tilting of the corner-shared BO_6 octahedra and thus induce a transition into a face-shared array that corresponds to the hexagonal structure. Based on the same consideration of ionic radii, the higher Co content would lead to an increase of the tolerance factor due to its smaller size compared with Fe ions in a certain valence state (see **Appendix D**). In short, materials enriched in Sr and Fe prefer cubic symmetry, whereas it becomes more difficult for BSCF to obtain cubic structure with high Ba and Co contents.

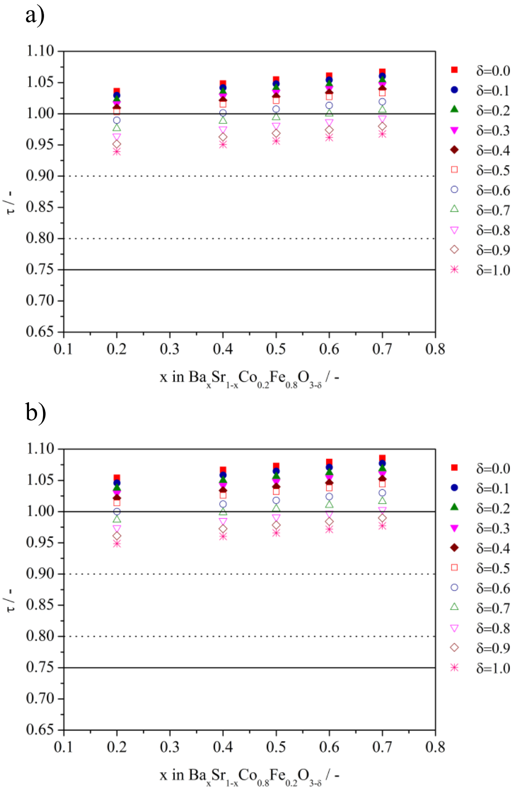

Fig. 5.2 The calculated Goldschmidt tolerance factor as a function of chemical composition with varying oxygen nonstoichiometry in BSCF materials (solid line: commonly recommended range of stable perovskite; dotted line: the range according to Goldschmidt)

Here, it is important to note that the oxidation and spin states of Co and Fe are truly different in this structure, while their valence states are not even close to integral values (B^{2+}, B^{3+} or B^{4+}) [106]. Further, the effective ionic radius of oxygen is unknown due to the existence of oxygen vacancies, the size of which remains unclear. Therefore, the perovskite should not be considered as a simple ionic compound and the τ value is only a general prediction of its structural stability.

5.1.2 Phase characterization

Phase components and structures of membrane materials are dominating factors in their oxygen permeation behaviours. In order to obtain high oxygen permeability of membranes, materials are required to possess single-phase perovskite structure. The calcined powders of different chemical compositions were analysed by XRD using Cu Kα radiation in this study.

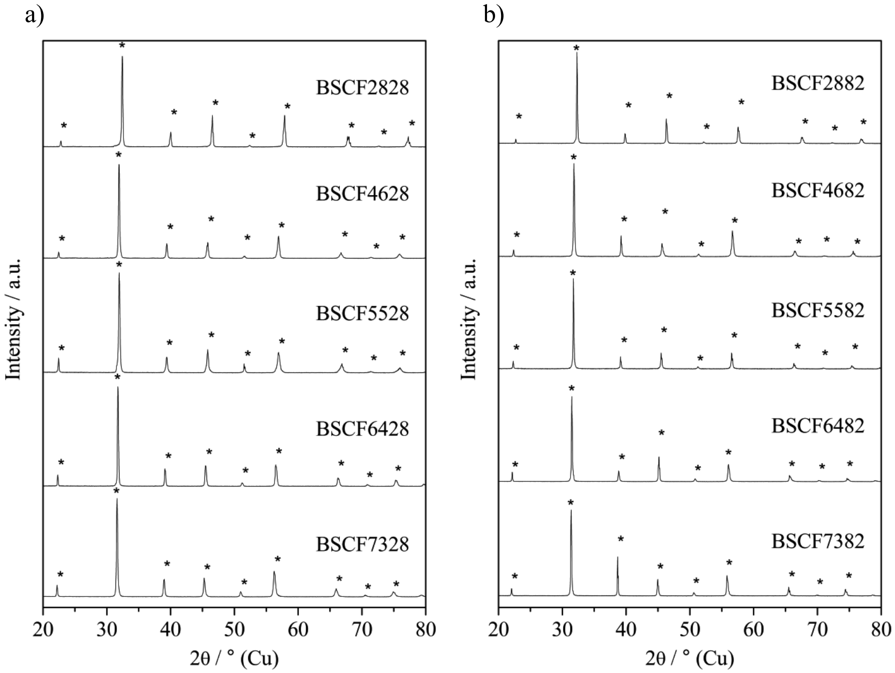

Fig. 5.3 The XRD diffraction patterns of calcined BSCF powders (peaks indexed as perovskite structure were marked with *)

Fig. 5.3 illustrates the XRD diffraction patterns of the investigated BSCF materials. All the peaks of BSCF powders were Miller indexed as perovskite structure, denoted individually with a star mark. The series of $Ba_xSr_{1-x}Co_{0.2}Fe_{0.8}O_{3-\delta}$ were found to be orthorhombic perovskites while the $Ba_xSr_{1-x}Co_{0.8}Fe_{0.2}O_{3-\delta}$ materials show pseudo-cubic symmetry. In addition, both series of BSCF powders exhibit a single-phase structure after calcination. Unlike SCF materials [55], no other additional diffraction pattern peaks were observed in BSCF. The absence of superstructure peaks as found in SCF oxides states that the oxygen vacancies in BSCF should be mobile and assist the oxygen transport process. From the XRD patterns, it could be observed that the main peak around ° shifts slightly towards left to lower degrees when the Ba content in $Ba_xSr_{1-x}Co_yFe_{1-y}O_{3-\delta}$ decreases from $x = 0.7$ to $x = 0.2$. This suggests that the lattice parameter of perovskite should increase constantly with the doping content of barium, which is in good agreement with the measured data in **Tab. 5.1**. As barium has the same valence state as strontium (+2) in the perovskites, the introduction of Ba into BSCF has marginal effect on the valence states of Co and Fe. Therefore, the expansion of structural lattice with barium content could be attributed primarily to the larger radius of

Ba^{2+} (1.61 Å) than that of Sr^{2+} (1.44 Å). The measured lattice parameters of $Ba_xSr_{1-x}Co_{0.8}Fe_{0.2}O_{3-\delta}$ are comparable with the reported data [116]. For an ideal perovskite, the lattice parameter should satisfy $a \quad (r \quad r\ ) \ \sqrt{\ } \ (r \quad r\ )$, which is around 4.26 Å in the case of BSCF materials. However, the lattice parameters measured by XRD analysis are much smaller than the ideal ones, as observed in the series of $Ba_xSr_{1-x}Co_{0.8}Fe_{0.2}O_{3-\delta}$. Large oxygen deficiency could exist in the unit cell owing to the bivalent state of barium and strontium. Such imperfection in the structure further results in the decrease of the coordination number of metal ions, which leads to the reduction of their effective ionic radii [117]. In other words, the effective coordination number of A-site cations in BSCF should be smaller than 12 and the effective average ionic radii of B-site cations are less than the calculated values for the determination of tolerance factors in **Chapter 5.1.1**. This deviation of BSCF structure from ideal perovskites due to the presence of oxygen vacancies plays an important role in the stability as well as the oxygen permeability of BSCF membranes.

Tab. 5.1 Lattice parameter, molar mass, unit cell volume and theoretical density of BSCF materials

Materials	a / Å	b / Å	c / Å	M / g/mol	V / Å^3	$_{theo.}$ / g/cm^3
BSCF2828	5.532	7.789	5.511	202.022	237.462	5.651
BSCF4628	5.594	7.880	5.573	211.964	245.662	5.731
BSCF5528	5.610	7.948	5.593	216.934	249.382	5.778
BSCF6428	5.655	7.974	5.641	221.905	254.369	5.794
BSCF7328	5.677	7.890	5.665	226.876	253.744	5.939
BSCF2882	3.921	-	-	203.875	60.282	5.616
BSCF4682	3.978	-	-	213.817	62.950	5.640
BSCF5582*	3.983	-	-	218.787	63.192	5.749
BSCF6482	4.019	-	-	223.758	64.916	5.724
BSCF7382	4.031	-	-	228.729	65.500	5.799

5.1.3 Chemical composition analysis

The chemical composition of as-calcined BSCF powders was analysed by Inductively coupled plasma optical emission spectrometer (ICP-OES) in Central Division of Analytical Chemistry (ZCH), Forschungszentrum Jülich. The relative error for each measurement is within ±3 wt.%. The measured compositions of materials investigated in this work are summarized in **Tab. 5.2**. It is apparent that all the chemical compositions are consistent with the target values considering the inaccuracy of measurements.

Tab. 5.2 Chemical compositions of the BSCF powders

Material	Barium / mol.%	Strontium / mol.%	Cobalt / mol.%	Iron / mol.%
BSCF2828	0.20 ± 0.01	0.80 ± 0.01	0.19 ± 0.01	0.81 ± 0.01
BSCF4628	0.40 ± 0.01	0.60 ± 0.01	0.21 ± 0.01	0.79 ± 0.01
BSCF5528	0.50 ± 0.01	0.50 ± 0.01	0.19 ± 0.01	0.81 ± 0.01
BSCF6428	0.59 ± 0.01	0.41 ± 0.01	0.19 ± 0.01	0.81 ± 0.01
BSCF7328	0.70 ± 0.01	0.30 ± 0.01	0.20 ± 0.01	0.80 ± 0.01
BSCF2882	0.21 ± 0.01	0.79 ± 0.01	0.80 ± 0.01	0.20 ± 0.01
BSCF4682	0.40 ± 0.01	0.60 ± 0.01	0.81 ± 0.01	0.19 ± 0.01
BSCF5582*	0.49 ± 0.01	0.51 ± 0.01	0.79 ± 0.01	0.21 ± 0.01
BSCF6482	0.60 ± 0.01	0.40 ± 0.01	0.80 ± 0.01	0.20 ± 0.01
BSCF7382	0.70 ± 0.01	0.30 ± 0.01	0.79 ± 0.01	0.21 ± 0.01

*BSCF5582 powder was received from Treibacher Industrie AG, Austria.

5.1.4 Particle size distribution

Sintering behaviour in the pressed green bodies is directly influenced by the particle size of the powders. Agglomerated powders with large mean particle size contain large pores among particles which increases the difficulty in both the pressing and sintering processes. To achieve low porosity density of the sintered membranes, the removal of those large pores requires high sintering temperature and long dwell time, resulting in grain growth or partial melting of the materials. Thus the particle sizes of calcined BSCF powders after wet milling for 24 h (except BSCF5582 as received) were analysed by laser granulometry in the Institute for Energy and Climate Research 1 (IEK-1). Three main parameters are responsible for the characterization of particle size distribution, i.e. D10, D50 and D90. Each denotes the equivalent diameter where certain mass percentage (10 wt.%, 50 wt.%, 90 wt.% respectively) of the particles has smaller sizes. The measured data of BSCF powders are listed in **Tab. 5.3**. It is obvious that all the refined BSCF materials have a value around m and the geometry mean value less than m (except BSCF5582). Powders with these particle size distributions are considered suitable for the following pressing and sintering procedure.

Tab. 5.3 Particle size distribution of BSCF powders in terms of D10, D50, D90 and geometry mean values

Materials	/ m	/ m	/ m	Geometry value / m
BSCF2828	0.64718	0.94481	1.42019	0.9644
BSCF4628	0.71668	1.02025	1.66699	1.2291
BSCF5528	0.62262	0.88960	1.32409	1.0432
BSCF6428	0.88009	1.29062	2.23532	1.4945
BSCF7328	0.62324	0.88557	1.26258	0.9299
BSCF2882	0.80158	1.12357	2.43059	1.6132
BSCF4682	0.82164	1.17729	1.93300	1.3259
BSCF5582*	2.62226	4.24980	6.41427	4.1518
BSCF6482	0.81478	1.16069	1.90615	1.3271
BSCF7382	0.84535	1.26318	2.57311	2.0112

*BSCF5582 powder was received from Treibacher Industrie AG, Austria.

5.2 Sintering behaviour of BSCF materials

For practical application, perovskite membranes are prepared through three procedures: powder synthesis, shaping and sintering. Sintering process with different sintering profiles, including atmosphere, sintering temperature, dwelling time and ramping rates, can definitely affect the membrane microstructure. Extensive research has been conducted to clarify the close relation of oxygen permeation performance with the microstructure of membranes, such as grain size and grain boundary structure [62, 63, 118-121]. Accordingly, the sintering behaviours of pressed BSCF pellets were investigated in this work. The melting point of each powder was measured by means of DTA/TG in order to avoid the melting of BSCF materials during sintering and to make a prediction of the proper sintering temperature. According to the detected melting points, the sintering behaviour of pressed pellets was systematically recorded by TMA. Sintering parameters for membrane production were determined based on the observed microstructures as well as the relative density of pellets sintered at different conditions in ambient air.

5.2.1 Melting temperature

As the pressed samples should be sintered at a temperature below their melting points, it is necessary to determine the melting temperatures of each BSCF material firstly. A small amount of wet-milled powder (~100 mg) was added in a platinum crucible for the measurements by DTA. The melting points of BSCF materials, obtained from the normalized DTA curves, are illustrated in **Fig. 5.4** and the data are summarized in **Tab. C.1**. It is clear that the melting temperature decreased with Ba content in both material series. The only exception is the BSCF5582 powder, which was provided by Treibacher Industrie AG, different from others which were synthesized in this study. The melting point of BSCF5582 is quite close to that of BSCF4682 (~1260 ℃); whereas it should arise below this temperature according to the decreasing tendency of the melting point in relation to the Ba content in the materials. This observation indicates that the melting point of BSCF might be influenced by the particle size of the powders, i.e. the larger particle size, the higher melting temperature is obtained (D50 (BSCF5582) ≈ 4.2 m, D50 (other BSCFs) ≈ 1.0 m In addition, the series of $Ba_xSr_{1-x}Co_{0.8}Fe_{0.2}O_{3-\delta}$ show much lower melting points than $Ba_xSr_{1-x}Co_{0.2}Fe_{0.8}O_{3-\delta}$ with the same composition of A-site cations, implying the melting point decreases with increasing cobalt concentration in the lattice. It is interesting to note that the tolerance factor is comparably closer to unity for the BSCF materials with a higher melting point (see **Fig. 5.1**). This means the material is more stabilized in the perovskite structure, indicating the influence of chemical composition on the bond strength in BSCF perovskites.

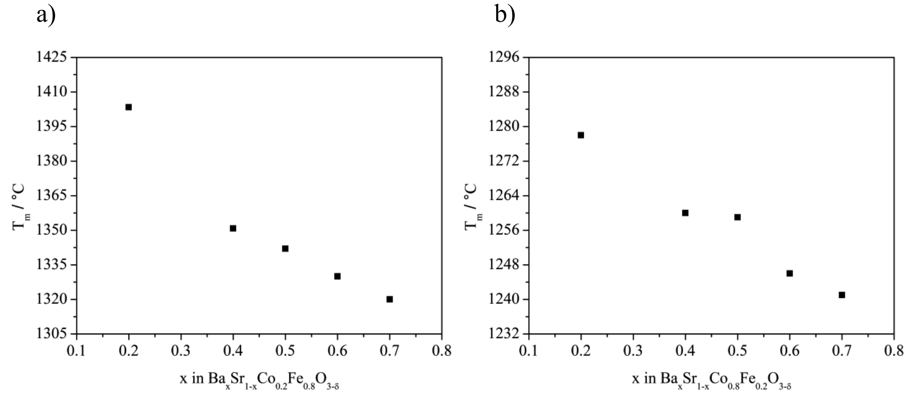

Fig. 5.4 Melting points of the calcined and wet-milled BSCF powders

5.2.2 Measurement of shrinkage curves

The sintering behaviour of pressed green pellets of BSCF were measured by TMA at temperatures below their melting points. The densification process during sintering was described in terms of shrinkage curves as a function of sintering temperature and dwelling time. In principle, the sintering process involves three stages with respect to mass transport mechanism among the powder particles: initial state, shrinkage state and the final stage. During the initial state, sintering necks are formed between two contacting particles and grow exponentially with time through the mechanism of evaporation and condensation. In the next shrinkage state of sintering, the growth of sintering neck continues and grain boundaries are formed among neighbouring particles. Large shrinkage could be observed in this period via volume and grain boundary diffusion. The relative density of samples could reach up to 95% of the theoretical density at the end of this stage [122]. In the final state, the residual pores in the sintered body are closed and pores grow together into larger sizes by volume diffusion. In the meanwhile, grain growth occurs at the expense of small grains combined with a reduction of grain boundary areas, resulting in further densification of the samples.

According to Wang et al. [63], dense BSCF membranes were obtained with considerably high relative densities (e.g., 95.80% after dwelling for 5 h) when sintered at a temperature of 1150 °C. Tan et al. [110] also reported that a sintering temperature of at least 1150 °C is required to produce dense BSCF membranes with negligible porosity. Thereby, the green BSCF pellets used in the current work were sintered at 1150 °C for 30 min to record their sintering behaviours, except BSCF2828 which possesses much higher melting point (see **Fig. 5.4 a**) than the others. For BSCF2828, the sintering temperature goes up to 1200 °C. Since negligible influence of heating rate was found within the range of 2-10 K/min on the shrinkage curves of materials [123], an average value of 6 K/min was selected as the ramping rate for the measurements.

BSCF2828

The measured shrinkage curve of BSCF2828 as a function of temperature is shown in **Fig. 5.5 a**. It can be seen that the shrinkage percentages of the pellet increase directly with sintering temperature. The shrinkage state of sintering process starts at ~720 °C in this sample, revealed by a significant rise in the dimensional change at higher temperatures. The value of the overall shrinkage reaches its maximum of -22.79% at the final temperature of 1200 °C. During the isothermal period, the shrinkage stays fairly constant and no further densification of the sample was found in this stage. Combined with the large shrinkage occurring upon heating, this maximal temperature of 1200 °C seems to be suitable for sintering the BSCF2828 samples.

Fig. 5.5 b represents the dependence of shrinkage rate of BSCF2828 on temperature during the shrinkage state in the sintering process. Two minimal values corresponding to the peaks could be observed from this curve, indicating the variation of the dominating mass transport mechanisms upon heating. The first peak appears around 790 °C and the second minimum is about 1028 °C. It was suggested that samples should be sintered at a temperature higher or at least equal to the second minimum in order to achieve a relative density larger than 90% [114]. Based on the measured shrinkage curve of BSCF2828, different sintering temperatures of 1150 °C and 1200 °C were thus chosen with a dwelling period of 3 h or 6 h respectively for the following production of the sintered samples. In combination with their respective microstructures and densities of the sintered pellets, the final sintering parameters for each material were yet determined.

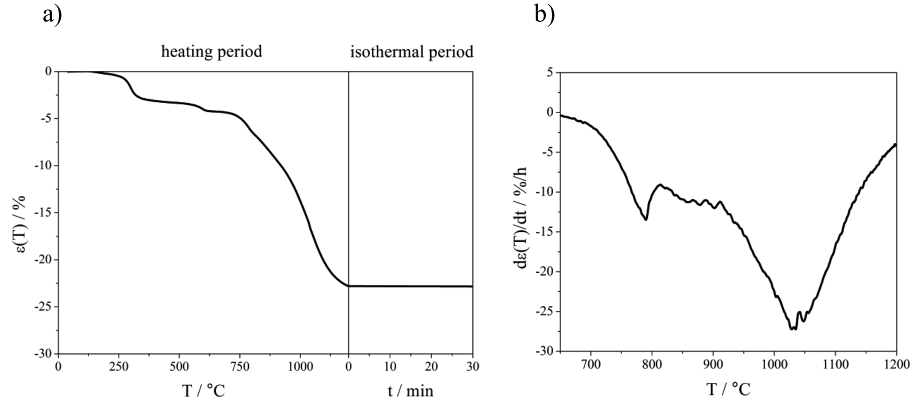

Fig. 5.5 Sintering behaviour of BSCF2828 in terms of a) shrinkage curve; b) shrinkage rate curve

BSCF4628

The temperature-dependent shrinkage curve of BSCF4628 is displayed in **Fig. 5.6 a**. Same to the sample of BSCF2828, the rise in sintering temperature leads to a larger shrinkage of the sample. A distinct shrinkage occurs at ~590 °C, which is much lower than ~720 °C observed in BSCF2828. The maximal shrinkage of BSCF4628 was obtained at 1150 °C with a value of -20.98%. Slight densification directing to the final sintering stage was detected within the range of 1.5% shrinkage during the isothermal period. This could be ascribed to the grain growth as well as complete enclosure and growth of pores controlled by the migration rate of grain boundaries.

From the derived shrinkage rate of BSCF4628 in **Fig. 5.6 b**, there are two minimal values in this curve that represent the change of the dominating mass transport mechanisms during the heating period. The first minimum value is about 797 °C and the next peak appears at ~1017 °C. As mentioned above, the sintering temperature is commonly selected higher than the temperature of the second peak. Therefore, two different sintering temperatures of 1050 °C and 1150 °C were utilized with a dwelling period of 3 h or 6 h respectively. Afterwards, the sintering parameters for BSCF4628 were determined according to the relative densities and microstructures of the sintered pellets under different sintering conditions.

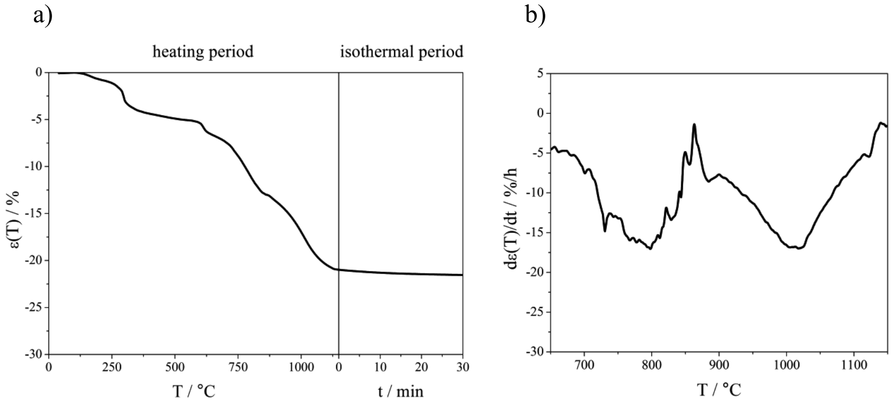

Fig. 5.6 Sintering behaviour of BSCF4628 in terms of a) shrinkage curve; b) shrinkage rate curve

BSCF4682

The change of shrinkage with sintering temperature in BSCF4682 material is shown in **Fig. 5.7 a**. The shrinkage percentages vary quite slowly in this material at temperatures below ~820 °C (around -2% shrinkage at this temperature) and almost no shrinkage occurs in the temperature range of ~410-770 °C. This observation is different from the shrinkage curves of BSCF2828 and BSCF4628, which show a slow but continuous shrinkage up to ~-5% at the end of the initial sintering state. Moreover, it is interesting to find that the onset temperature of the shrinkage state for sintering process in

BSCF2828 (~720 °C) and BSCF4628 (~590 °C) samples are lower than the one in BSCF4682 (~820 °C), in contrast to the melting points of both series (see **Fig. 5.4**). The overall shrinkage of BSCF4682 reaches -17.83% at 1150 °C, which is also smaller than that of BSCF4628 (-20.98%) at the same sintering temperature. This may probably suggest that the higher cobalt concentration in BSCF could retard the start of the shrinkage stage accompanied with a lower shrinkage for different sintering states during heating. Further densification of the pellet was detected in the isothermal period by a slight shrinkage within 1%.

The shrinkage rate of BSCF4682 in relation to the sintering temperature is displayed in **Fig. 5.7 b**. Two minimum values of 865 °C and 1013 °C can be obtained from this curve, which are close to the data of BSCF2828 and BSCF4628. According to the slight shrinkage during the isothermal period in the shrinkage curve as well as the peaks in the shrinkage rate curve, two different temperatures of 1050 °C and 1100 °C were chosen to sinter the BSCF4682 pellets for the further analysis of their relative densities and microstructures. The green pellets were dwelled for a period of 3 h or 6 h respectively during sintering.

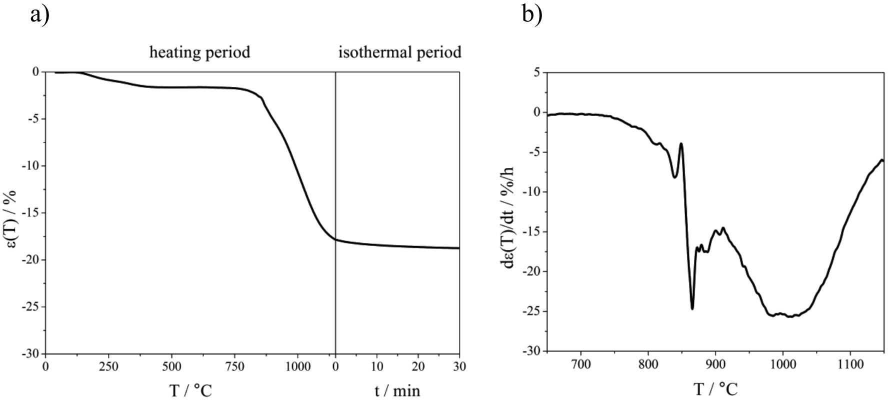

Fig. 5.7 Sintering behaviour of BSCF4682 in terms of a) shrinkage curve; b) shrinkage rate curve

BSCF6482

The sintering process of BSCF6482 material was recorded with temperatures up to 1150 °C and the measured shrinkage curve is illustrated in **Fig. 5.8 a**. Consistent with other BSCF pellets, the BSCF6482 sample shrinks gradually by elevating the sintering temperature. The onset temperature of the shrinkage state is around 840 °C. Similar to the observation in BSCF4682, the shrinkage of BSCF6482 changes quite slowly at temperatures below ~840 °C (about -2% shrinkage at this temperature) and almost no shrinkage occurs in the temperature range of ~390-840 °C. At the end of the heating period, the shrinkage of the pellet increases to its maximum of -19.60%. Then the shrinkage curve reaches a plateau with negligible densification in the pellet during the isothermal process.

The shrinkage rate of BSCF6482 as a function of sintering temperature is exhibited in **Fig. 5.8 b**. Compared with other shrinkage rate curves of BSCF pellets, there is no detectable shrinkage in BSCF6482 at temperatures below ~840 °C as the shrinkage rate stays at zero. This is consistent with the findings in the shrinkage curve of this material. Above this temperature, a sudden increase in the shrinkage rate to its maximum of -35.19 %/h was observed and this value is much larger than the ones found in other BSCF samples which are below -30 %/h. Thus, it could be concluded that the sintering process in the BSCF6482 starts at higher temperature and proceeds quite rapidly. The two peaks corresponding to the values of 898 °C and 991 °C are displayed in this curve. Accordingly, different temperatures of 1050 °C and 1100 °C were selected as the sintering temperatures with a dwelling period of 3 h or 6 h respectively for the sequential analysis of the relative density and microstructure of the sintered pellets.

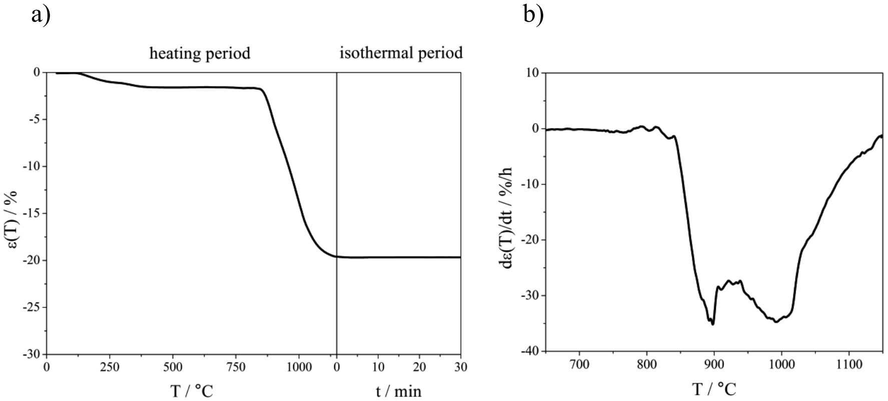

Fig. 5.8 Sintering behaviour of BSCF6482 in terms of a) shrinkage curve; b) shrinkage rate curve

All the characteristic temperatures and the overall shrinkage from the measured sintering curves in BSCF pellets are summarized in **Tab. 5.4**. Most obviously, the first minimal temperature of the peaks in the shrinkage rate curves varies in the sequence of BSCF6482 > BSCF4682 > BSCF4628 > BSCF2828, which is contrary to the tendency of their melting points. In addition, the onset temperature for the shrinkage stage of $Ba_xSr_{1-x}Co_{0.8}Fe_{0.2}O_{3-\delta}$ series is higher than that of the other series $Ba_xSr_{1-x}Co_{0.2}Fe_{0.8}O_{3-\delta}$. It probably means that the elements of barium and cobalt which increase the melting points of materials would decelerate the initial state of sintering process. However, the second minimal temperature of BSCF was found to increase in accordance with their melting points. In order to achieve a dense oxygen-permeable membrane, the critical temperature for a complete sintering process could be estimated by the melting points of BSCF materials, which increase with strontium and iron concentrations.

Tab. 5.4 The onset temperature of the sintering shrinkage state T_{onset}, two minimum values detected in the shrinkage rate curves T_{min}, the measured total shrinkage ε_{total} of BSCF pellets and the selected sintering temperatures T_{sinter} based on the TMA results

Materials	T_{onset}	$T_{min,1}$	$T_{min,2}$	ε_{total}	$T_{sinter} > T_{min,2}$	
BSCF2828	~720 ℃	790 ℃	1028 ℃	-22.79%	1150 °C	1200 °C
BSCF4628	~590 ℃	797 ℃	1017 ℃	-20.98%	1050 °C	1150 °C
BSCF4682	~820 ℃	865 ℃	1013 ℃	-17.83%	1050 °C	1100 °C
BSCF6482	~840 °C	898 ℃	991 ℃	-19.60%	1050 °C	1100 °C

5.2.3 Relative density of sintered samples

After sintering, the porosity density of the pellets was assessed in terms of relative density, i.e. the measured sample density divided by its theoretical density. This density value could also be used to evaluate the parameters of shaping and sintering process. In this work, the density of sintered BSCF pellets was measured by Archimedes method and their calculated relative densities are listed in **Tab. 5.5**. It was suggested that membranes with relative densities higher than 90% are suitable for oxygen separation [124]. The results show that almost all the sintered samples could be regarded as dense BSCF pellets. Commonly, the density of pellets increases with sintering temperature and dwelling time. This densification is caused by grain growth along with the merging of grains and from macroscopic view, the shrinkage. Accordingly, samples with larger shrinkage would have lower porosity density. The highest relative density of 96% was achieved in BSCF6482 for a dwelling period of 6 h. Compared with the densities of BSCF4682 pellets under the same sintering condition, the higher relative density in BSCF6482 could be attributed to its larger overall shrinkage (see **Tab. 5.4**).

Tab. 5.5 The relative density of the sintered pellets with different sintering parameters

Materials	Sintering Temperature	Dwelling time	
		3 h	6 h
BSCF2828	1150 °C	89%	92%
	1200 °C	-	93%
BSCF4628	1050 °C	89%	91%
	1150 °C	-	93%
BSCF4682	1050 °C	94%	94%
	1100 °C	-	95%
BSCF6482	1050 °C	95%	96%
	1100 °C	-	96%

5.2.4 Determination of sintering temperature and dwell time

It has been confirmed that the oxygen permeability of the ceramic membranes is sensitive to microstructural features, such as porosity density and grain size [121, 125-127]. Thus the influence of sintering parameters on the microstructures of BSCF sintered pellets was investigated. Samples were sintered in a temperature range of 1050-1200 °C for different periods of 3 h or 6 h respectively in ambient air. Afterwards, the morphology of the cross sections of sintered pellets was imaged by SEM. Combined with the relative density of BSCF pellets, the specific sintering parameters for pellets/membranes production for the following analysis were determined. Since the grain size of dense membranes was reported to impact significantly the oxygen permeation performance [63], the microstructure of each BSCF material sintered according to its specific sintering parameters was analysed to achieve an average value of grain size.

BSCF2828

The SEM micrographs of the cross sections of BSCF2828 pellets sintered at 1150 °C and 1200 °C for a period of 3 h and 6 h respectively are shown in **Fig. 5.9**. A small amount of (Co, Fe)-oxide was found in the microstructure of the pellet sintered at 1150 °C for 3 h. However, this secondary phase vanishes in the bulk of the pellet when the dwelling time is extended to 6 h, resulting in a single-phase microstructure. It is clear that the pellet sintered at 1200 °C is denser than the one sintered at lower temperature for the same dwelling time. The porosity density in the microstructure decreases in accordance with sintering temperature. In the meanwhile, grain growth could be observed in the sample sintered at 1200 °C in contrast to the others sintered at

1150 ℃ , representing a dense pellet with clear grain boundaries. Combined with the relative density of sintered pellets in **Tab. 5.5** that denser samples were achieved at higher sintering temperature, which is in good agreement with the microstructures observed here. The sintering parameters for BSCF2828 were determined accordingly and are listed in **Tab. 5.6**.

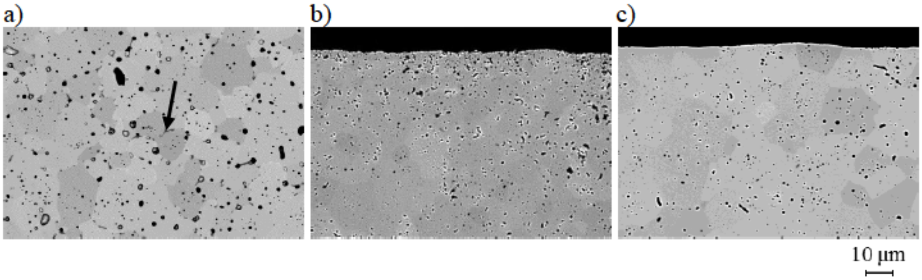

Fig. 5.9 SEM micrographs of BSCF2828 pellets sintered a) at 1150 °C for 3 h; b) at 1150 °C for 6 h; c) at 1200 °C for 6 h

BSCF4628

Fig. 5.10 shows the SEM micrographs of the cross sections of BSCF4628 pellets sintered at 1050 °C and 1150 °C for a period of 3 h or 6 h respectively. Obviously, secondary phases were found in the sample after sintering at 1050 °C for 3 h. These secondary phases are enriched in cobalt and depleted in strontium. The reason for the formation of secondary phases in BSCF4628 after sintering remains unclear. Considering the single-phase structure in the sample sintered for a dwelling period of 6 h, the secondary phases appear to redissolve into the bulk with the extension of dwell time. However, large porosity density could be observed in the pellet sintered at 1050 °C for 6 h, which has an adverse effect on the oxygen permeability of the membrane. By increasing the sintering temperature to 1150 °C, the porosity density of the pellet is significantly decreased and clear grain growth was detected here compared to the pellet sintered at 1050 °C. The reduction in porosity density of the pellet sintered at the higher temperature is also represented by a ~2% density increment as shown in **Tab. 5.5**. According to the observations, the sintering parameters for BSCF4628 materials were determined and are listed in **Tab. 5.6**.

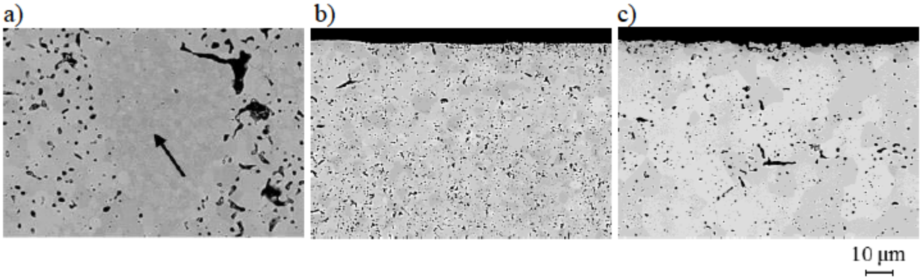

Fig. 5.10 SEM micrographs of BSCF4628 pellets sintered a) at 1050 °C for 3 h; b) at 1050 °C for 6 h; c) at 1150 °C for 6 h

BSCF4682

The microstructures of BSCF4682 pellets sintered at 1050 °C and 1100 °C for a period of 3 h or 6 h respectively are shown in **Fig. 5.11**. It appears that the microstructures are quite similar for the pellets sintered at 1050 °C but for different dwelling periods. A slight reduction in the porosity together with the growth of pore sizes on the cross sections of the pellets could be observed by prolonging the dwelling period from 3 h to 6 h. In contrast, the porosity density in the pellets was greatly decreased by enhancing sintering temperature from 1050 ℃ to 1100 ℃, resulting from the secondary recrystallization occurring at higher temperature for the same dwelling period. During the grain growth in the pellet, the amount of grain boundary is reduced, which is definitely important to the oxygen permeability of BSCF membranes. This reduction of pores along with grain growth as observed in the microstructure of the pellet sintered at 1100 °C leads to a ~1% increment of the relative density compared to the one sintered at 1050 °C for 6 h (see **Tab. 5.5**). Considering both the relative density and the microstructures of sintered pellets, the specific sintering parameter for pellets/ membranes production of BSCF4682 were determined (see **Tab. 5.6**).

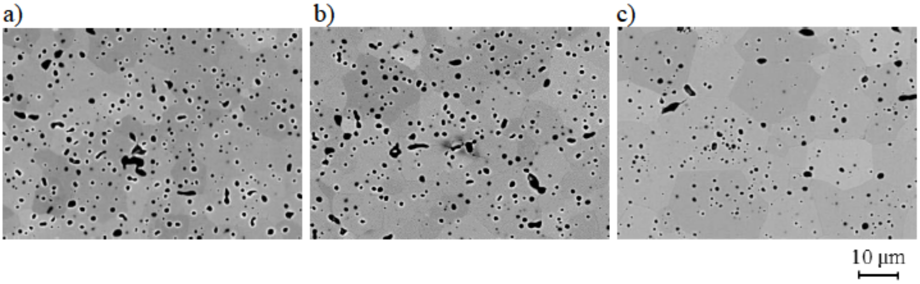

Fig. 5.11 SEM micrographs of BSCF4682 pellets sintered a) at 1050 °C for 3 h; b) at 1050 °C for 6 h; c) at 1100 °C for 6 h

BSCF6482

The SEM micrographs of the cross sections of BSCF6482 pellets sintered at 1050 °C and 1100 °C for different periods of 3 h or 6 h respectively are shown in **Fig. 5.12**. After a short dwelling time of 3 h at 1050 °C, a relatively large amount of pores were found in the microstructure. Same to other sintered BSCF samples, the porosity density in the BSCF6482 pellets is reduced by extending the dwelling period to 6 h. However, small particles recognized as Co-oxides could be observed in the matrix of the sample after sintering at 1050 °C for 6 h. Some of these Co-oxides are formed at the boundary sites, in agreement with the observation in [127]. The formation of secondary phases during sintering was ascribed to the minimization of the surface and interface energy along the boundary of two neighbouring grains [127]. Interestingly, the Co-oxides vanish in the microstructure of the pellet sintered at higher temperature of 1100 °C for the same dwelling period of 6 h, yielding a complete single-phase microstructure with less porosity. Grain growth could also be observed in the sample sintered at 1100 °C compared to the one at 1050 ℃ . No increment of the relative density was detected in this material by increasing the sintering temperature (see **Tab. 5.5**). As membranes should possess single-phase perovskite structure for the oxygen permeation tests, the sintering parameters for BSCF6482 were determined based on this requirement and the results are listed in **Tab. 5.6**.

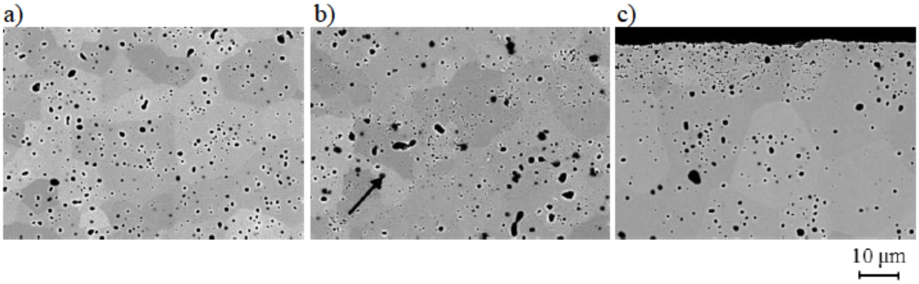

Fig. 5.12 SEM micrographs of BSCF6482 pellets sintered a) at 1050 °C for 3 h; b) at 1050 °C for 6 h; c) at 1100 °C for 6 h

Tab. 5.6 The sintering parameters and the average grain size of the sintered BSCF pellets

Materials	Sintering temperature	Dwelling time	Grain size
BSCF2828	1200 °C	6 h	m
BSCF4628	1150 °C	6 h	m
BSCF4682	1100 °C	6 h	m
BSCF5582*	1000 °C	6 h	m
BSCF6482	1100 °C	6 h	m

*Samples of BSCF5582 were sintered in Institute for Energy and Climate Research 1 (IEK-1), Forschungszentrum Jülich GmbH and the sintering parameters for this material was not referred to in this study

5.3 Thermochemical properties of membrane materials

5.3.1 Variation of oxygen nonstoichiometry

As mentioned in **Chapter 3.22**, oxygen vacancies are created in the perovskite lattice upon heating. This phenomenon could be recognized by the variation of oxygen stoichiometry in the oxides, which may have significant influence on the oxygen permeation behaviour of membranes. In this study, the weight loss in the sintered BSCF pellets in synthetic air was measured by TGA at intermediate temperatures till 1000 ℃ . The change of oxygen nonstoichiometry δ was calculated according to **Eq. 4.4**. The influences of temperature and chemical composition of BSCF materials on the δ values are clearly presented in **Fig. 5.13**.

Oxygen release occurs at ~500-550 ℃ for all the perovskites as the non-equilibrium oxygen is yet trapped in the lattice at lower temperatures. This onset temperature for large oxygen desorption is higher compared to the reported ~300 °C in SCF and BSCF5582 materials [53]. It is confirmed that the oxygen deficit of BSCF oxides increases gradually with temperature which represents the loss of lattice oxygen. omparing S and S at a given temperature, the δ values of both materials are quite similar and their oxygen stoichiometries virtually coincide at 900 ℃ with the δ equal to -0.14. When temperature rises higher than this inflection point, the variation of oxygen stoichiometry increases with the doping of barium. For example, the δ value for BSCF2828 is -0.16 and -0.14 for BSCF4628 at 1000 ℃ . More obviously, all the δ values of BSCF6482 are higher than BSCF4682 at intermediate temperatures of 750-1000 °C. he δ value of BSCF4682 reaches its minimum of -0.13, while for BSCF6482 the value is -0.12 at 1000 °C. According to McIntosh et al. [26], it was proposed that higher oxygen stoichiometries could be obtained by increasing the basicity of the A-site cations. By doping with the more basic element of Ba^{2+} compared to Sr^{2+}, higher oxidation states of the B-site cations are stabilized and thus fewer oxygen vacancies are generated in the perovskites. This prediction is supported by the investigation of the oxygen desorption behaviour in BSCF powders [82], as the introduction of barium was found to suppress the valence change of B-site cations between +3 and +4. In the meanwhile, the δ values of BSCF4628 are lower than those of BSCF4682 at a certain temperature, indicating the oxygen stoichiometry decreases with iron content. This is in good agreement with the observations in [32, 128] that larger oxygen release was found in BSCF with higher iron concentration. Along with the loss of lattice oxygen, the B-site metal ions in BSCF are prone to a lower valence state in order to keep the perovskite structure, e.g. the reduction of Co^{4+}/Fe^{4+} ions to Co^{3+}/Fe^{3+} or even to Co^{2+}. Therefore, it could be concluded, from another point of view, that the reduction of Fe^{4+} upon heating could be considered as the major source of weight loss in BSCF materials.

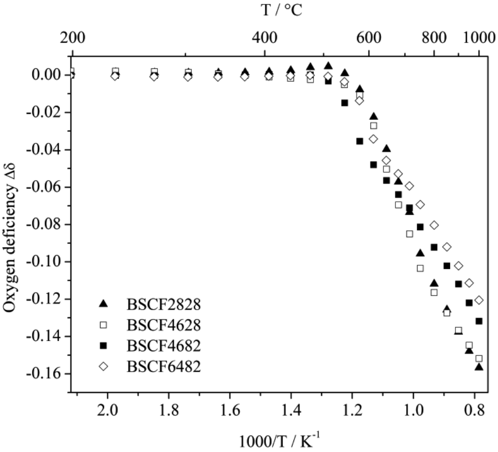

Fig. 5.13 The variation of oxygen nonstoichiometry in BSCF materials as a function of temperature

5.3.2 Thermochemical expansion behaviour

The thermal expansion behaviour of BSCF materials were recorded in synthetic air atmosphere by means of TMA. From the calculated TEC values in **Fig. 5.14**, it is evident that all the expansion behaviours of BSCF are nonlinear with a sudden increase in their slopes between ~500-550 °C, depending on the chemical compositions of materials. The finding of the inflection points in the TEC curves is consistent with the observation in the variation of oxygen nonstoichiometry in **Fig. 5.13**. Kriegel et al. [58] and Wei et al. [72] also reported that nearly linear thermal expansion of BSCF materials was obtained up to approximately 550 °C in air. This nonlinear behaviour at higher temperatures is generally associated with the formation of oxygen vacancies in the perovskites due to the loss of lattice oxygen upon heating. This so-called chemical expansion could be attributed to the enhanced repulsion force between cations as well as the reduction of B-site cations to lower valence states [100, 129]. The inflection points in the TEC curves as well as the TEC values in both temperature ranges divided by these characteristic points are summarized in **Tab. 5.7**.

For BSCF2828, the thermal expansion increases steadily upon heating at the beginning stage till ~540 °C. When the temperature is further increased up to 900 °C, a sharp rise of TEC was observed with the values varying from 17.6×10^{-6} K^{-1} to 26.3×10^{-6} K^{-1}. This jump of expansion behaviour in this material is related to the reduction of B-site cations from the valence of +4 to +3. The defect chemistry along with the release of oxygen could be described using Kröger-Vink notation.

$$^{x} \quad \leftrightarrow \quad - \quad ^{x}$$

It should be noticed that the valence change is associated with an increase of the ionic radius, especially for the reduction of Co^{4+} to Co^{3+}. At even higher temperatures (T > 900 °C), a relative stable TEC value of $\sim26.7\times10^{-6}$ K^{-1} was obtained. It was reported that the Co^{3+} could be further reduced to Co^{2+} in the high temperature range [89] caused by the desorption of lattice oxygen.

$$^{x} \quad ^{x}\leftrightarrow \quad -$$

However, considering the larger radius change from Co^{3+} to Co^{2+}, this further reduction of cobalt ions might not occur in this material as no obvious increase in TEC values was observed here.

Similarly, a slow increase in TEC values was achieved in BSCF4628 at temperatures lower than ~500 °C, and then the slope of this curve becomes steeper, resulting from the large increment of chemical expansion. At temperatures above 800 °C, the TEC value of this material approaches a plateau of 24.3×10^{-6} K^{-1}. If comparing the thermochemical expansion behavior of BSCF4628 with that of BSCF2828, it could be found that the TEC values increase with strontium concentration in the BSCF materials. Combined with the results from TGA measurements in **Fig. 5.13**, the larger expansion of

BSCF4628 could be ascribed to the more significant loss of lattice oxygen upon heating compared with BSCF2828. In other words, BSCF containing higher Sr content would release more oxygen by increasing temperature which conduces to larger chemical expansion in the TEC curves.

Different from the expansion behaviours of BSCF2828 and BSCF4628, the TEC curve of BSCF4682 is much steady at temperatures above the inflection point of 520 ℃ . A slight increment of TEC values from 12.8×10^{-6} K^{-1} to 18.8×10^{-6} K^{-1} was obtained in this temperature range. Moreover, no plateau of TEC values of this material was observed at high temperatures compared to other two BSCF materials with lower cobalt content. This might probably indicate that the further reduction of B-site cations may occur in this material. In addition, the increase in cobalt content in BSCF definitely leads to the drop of TEC values as comparing the expansion curves of BSCF4628 and BSCF4682. This could also be rationalized by the observation from TGA measurements (see **Fig. 5.13**) that the change of oxygen nonstoichiometry is larger in BSCF materials with lower cobalt content, resulting in higher oxygen vacancy concentration and thus larger chemical expansion of BSCF4628 than that of BSCF4682. It is in good agreement with the findings in $Ba_{0.5}Sr_{0.5}Co_yFe_{1-y}O_{3-\delta}$ materials where the TEC values increase with decreasing the doping content of cobalt [73, 129].

The TEC curve of BSCF6482 stays quite close to that of BSCF4682 with similar inflection points as well as similar chemical expansion behaviour. The increment of TEC values caused by chemical expansion in BSCF6482 at temperatures higher than ~530 ℃ is slightly lower compared to that in BSCF4682. This result is consistent with the conclusion reached by comparing the TEC curves and the TGA results of BSCF2828 and BSCF4628 that larger chemical expansion was achieved with higher strontium content in the BSCF materials.

In short, high thermochemical expansion were obtained in BSCF materials with the TEC values of ~25×10^{-6} K^{-1} for $Ba_xSr_{(1-x)}Co_{0.2}Fe_{0.8}O_{3-\delta}$ series and ~18×10^{-6} K^{-1} for $Ba_xSr_{(1-x)}Co_{0.8}Fe_{0.2}O_{3-\delta}$ series in the intermediate temperature range of 550-1000 °C. A nearly constant TEC value was achieved in $Ba_xSr_{(1-x)}Co_{0.2}Fe_{0.8}O_{3-\delta}$ series at high temperatures above 800 °C whereas no plateau was found in $Ba_xSr_{(1-x)}Co_{0.2}Fe_{0.8}O_{3-\delta}$ series. The TEC values of BSCF materials increase with strontium/iron contents, which could be explained by the results from TGA measurements in terms of the loss of lattice oxygen.

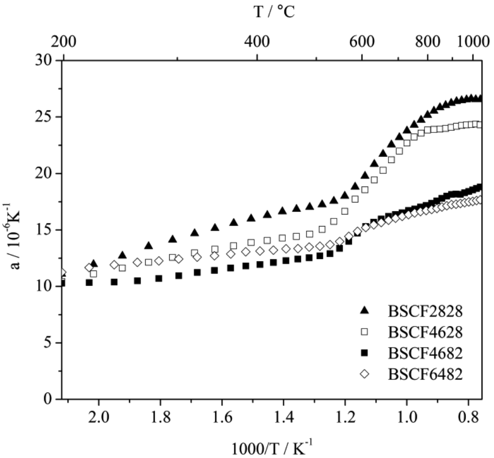

Fig. 5.14 Temperature dependence of the thermal expansion coefficients of BSCF materials measured in synthetic air atmosphere

Tab. 5.7 The inflection points of TEC curves and the TEC values of BSCF materials in different temperature ranges

Materials	$T_{inflection}$ / °C	α < $T_{inflection}$) / 10^{-6} K^{-1}	α > $T_{inflection}$) / 10^{-6} K^{-1}
BSCF2828	~540	11.4-17.6	17.6-26.7
BSCF4628	~500	10.4-14.9	14.9-24.3
BSCF4682	~520	10.3-12.8	12.8-18.8
BSCF6482	~530	10.5-13.7	13.7-17.7

5.4 Long-term oxygen permeability of BSCF membranes

In the case of practical application, MIEC membranes are required to produce stable oxygen permeation flux during long-term operation in the oxyfuel process. The BSCF membranes of different chemical compositions or membrane thicknesses were used in the current work. The recipient for each measurement was heated in a tubular furnace and its temperature was monitored according to the measured temperature by a K-type thermoelement beside the membrane.

5.4.1 Long-term permeation measurement at 850 °C

The long-term oxygen permeation behaviour of two BSCF membranes: BSCF4628 and BSCF6482 with a thickness of 2.0 mm were recorded under the air/He pressure gradient at 850 ℃ for 2000 h. The permeate oxygen flux of each membrane was calculated by excluding the leakage contribution according to **Eq. 4.8**. The oxygen permeation rate as a function of time along with the phase components and structures in the used membranes is discussed.

BSCF4628

Fig. 5.35 displays the oxygen flux through the BSCF4628 membrane of 2.0 mm thickness at 850 °C for a long-term period of 2000 h with one side of the membrane exposed to synthetic air and the other side flowed by helium. The oxygen flux at the permeate side of the membrane increases slightly from 0.62 ml cm^{-2} min^{-1} to 0.78 ml cm^{-2} min^{-1}, i.e. enhanced 26% of the initial value over the entire 2000 h. The time-dependent permeation rate of this membrane can be fitted to an exponential equation (shown as the black line),

$$\exp\left(\frac{t}{\quad}\right)$$

According to this permeation curve, it is obvious that this increment of oxygen flux could not reach a steady state over 2000 h and should proceed further with longer operation period.

In order to clarify the enhanced oxygen permeation behavior of BSCF4628 membrane, SEM analysis was performed to exam the phase changes in the used membrane after long-term operation, as shown in **Fig. 5.16**. Secondary phases were observed predominately at the feed side of the membrane, which disperse along the grain boundary sites. By quantification of the local EDX analysis in **Tab. 5.8**, a 2:1 ratio of the A-site to B-site cations was obtained in the formed secondary phases. Moreover, a great enrichment of barium in the precipitates was found compared to that in the bulk.

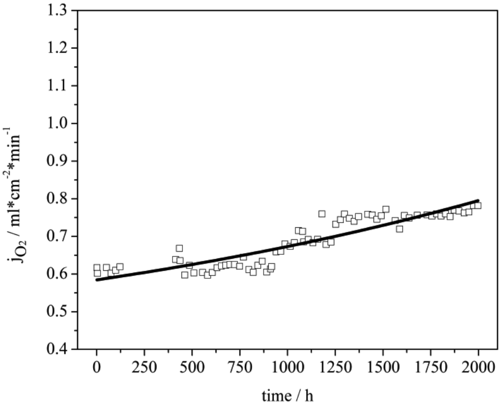

Fig. 5.15 Oxygen permeation flux through the 2.0 mm-thick BSCF4628 membrane at 850 °C for 2000 h under the air/He partial pressure gradient

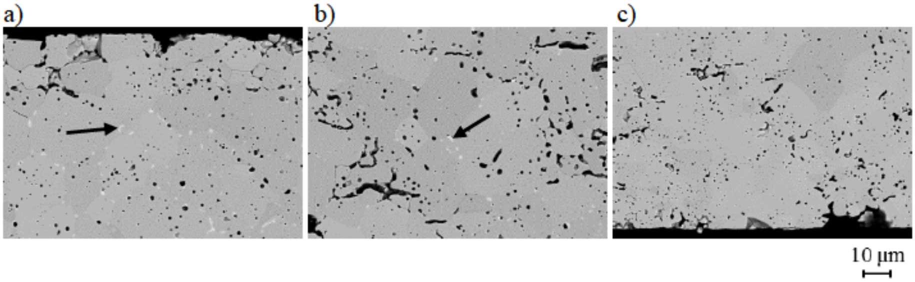

Fig. 5.16 SEM micrographs of a) the feed side; b) the inner part and c) the sweep side of the 2.0 mm-thick BSCF4628 membrane after long-term permeation test at 850 °C for a period of 2000 h under the air/He partial pressure gradient

Tab. 5.8 Quantitative local chemical composition of the BSCF4628 membrane after 2000 h oxygen permeation test at 850 °C in atomic percentage

Position	Ba / atom%	Sr / atom%	Co / atom%	Fe / atom%	O / atom%
Bulk	8.8	14.1	3.9	15.6	57.6
Precipitates	14.4	15.8	2.8	10.9	56.1

Despite of the influence of phase segregation, Shao et al. [82] ascribed the increment of oxygen flux through the BSCF5582 membrane at 850 °C to the improvement of its surface roughness of the used membrane. Accordingly, both surfaces of the feed and sweep sides of the BSCF4628 membrane after 2000 h operation were analyzed by SEM and then compared with the polished fresh surfaces of the membrane before long-term measurement (shown in **Fig. 5.17**). Consistent with the findings by Shao et al. [82], the surface roughness of the used membrane is virtually increased after long-term operation compared to the fresh sample. This increment of surface roughness yields concomitantly an increase in the effective surface area of the membrane during the long-term operation. The enlargement of membrane surface area could accelerate the oxygen permeation process as the surface exchange kinetics is improved [80], although bulk diffusion should be rate-determining here with respect to the membrane thickness (2.0 mm) selected in this measurement [130]. In this way, the rise in oxygen flux with time should be slow as observed here, due to the small contribution from the surface exchange to the entire oxygen permeation rate. The change of membrane surface morphology was also observed in BSCF2828 after 75 h operation at 950 °C [105].

Moreover, the average grain size increases from 10.26 m to 28.27 m after 2000 h operation. Based on the observations in [63, 110, 120, 126], membranes with larger grains exhibit a higher oxygen permeation flux. Therefore, it could be concluded that the slow increase in oxygen flux through the BSCF4628 membrane might come from the enlargement of surface roughness of the used membrane as well as grain growth during operation.

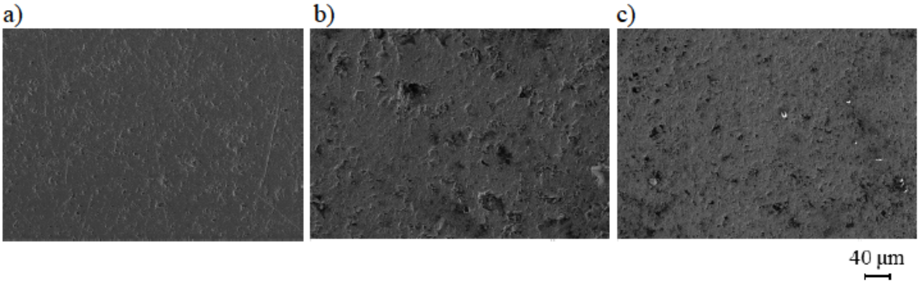

Fig. 5.17 Surface morphology of a) the polished fresh surface; b) the feed side and c) the sweep side of the BCSF4628 membrane after 2000 h oxygen permeation test at 850 °C under the air/He partial pressure gradient

BSCF6482

The oxygen permeation rate of the 2.0 mm-thick BSCF6482 membrane measured at 850 °C in air/He atmospheres for 2000 h is illustrated in **Fig. 5.18**. Different from the enhanced permeation rate of the BSCF4628 membrane with time, the oxygen flux through the BSCF6482 membrane shows a slightly deterioration as the oxygen permeation rate varies from 1.08 ml cm^{-2} min^{-1} to 0.88 ml cm^{-2} min^{-1} over the entire 2000 h.

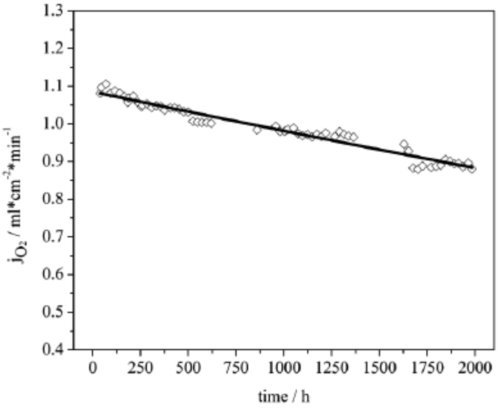

Fig. 5.18 Oxygen permeation flux through the 2.0 mm-thick BSCF6482 membrane at 850 °C for 2000 h under the air/He partial pressure gradient

The time-dependent permeation rate of this membrane can be well fitted to an exponential equation (shown as the black line),

$$\exp\left(\frac{t}{\quad}\right)$$

The reasons for the decay of oxygen permeability of BSCF membranes at intermediate temperatures could be various. One of the most proposed is the phase decomposition of cubic perovskite into noncubic structure [55, 58, 70, 98]. Therefore, it is necessary to exam the phase components and their structures in the used membranes. As shown in **Fig. 5.19**, secondary phases were found in the entire cross sections of the BSCF6482 membrane after long-term permeation.

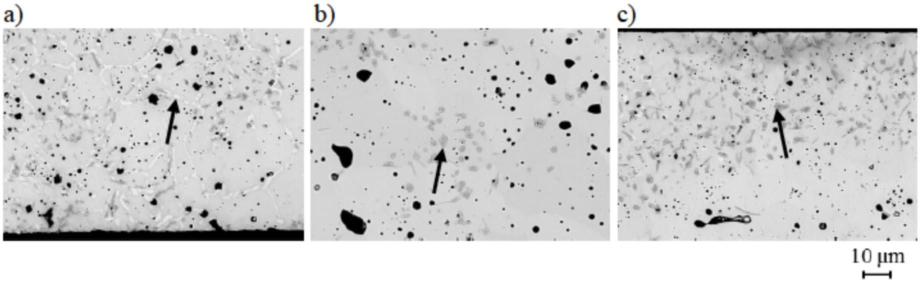

Fig. 5.19 SEM micrographs of a) the feed side; b) the inner part and c) the sweep side of the 2.0 mm-thick BSCF6482 membrane after long-term permeation test at 850 °C for a period of 2000 h under the air/He partial pressure gradient

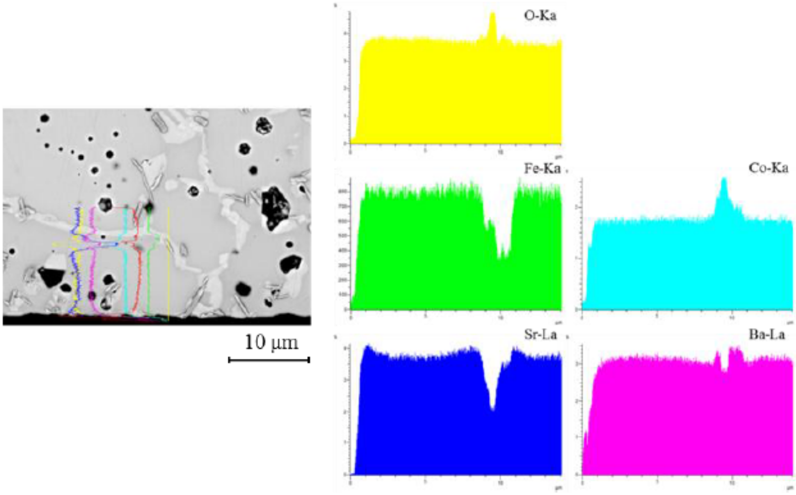

Fig. 5.20 The elemental distributions along the cross section of the feed side of the BSCF6482 membrane after long-term permeation measurement at 850 °C for 2000 h under the air/He pressure gradient

It is quite obvious that nearly all the boundary sites at the feed side of the membrane are decorated with secondary phases. According to the linescans displayed in **Fig. 5.20**, the major secondary phase along grain boundary is characterized by a substantial enrichment in barium and cobalt as well as a significant depletion in strontium and iron. Same observation was found by Mueller et al. in BSCF5582 ceramics after annealing at 800 °C in air for 192 h [131]. Moreover, it is interesting to note that the oxygen stoichiometry at the boundary sites, where the secondary phase is located, is higher than that in the bulk. From the XRD analysis of the used membrane (see **Fig. 5.21**), about 4% of hexagonal phase was detected in the BSCF6482 membrane after 2000 h operation, which could be denoted as $(Ba,Sr)CoO_3$. The lack of higher indexed reflections may be caused by the small structure factors as well as the relatively small volume fractions of the hexagonal phase [99]. Combined with the SEM micrograph at the feed side, it indicates that the secondary phase formed along the grain boundaries at the feed side of the used membrane should be related to the Fe-depleted hexagonal phase as observed in the XRD patterns. In addition, the oxygen content in the hexagonal phase was reported to be higher than that in the cubic matrix [132], further confirming that the hexagonal phase arrays at the boundary sites in the microstructure. The formation of secondary phases with lower structure symmetry act as barriers for oxygen transport and thus result in the reduction of oxygen permeability. Yoshiya et al. [133] calculated the formation energy of an oxide ion vacancy in both hexagonal- and cubic-structured $BaCoO_3$. They found that the formation of oxygen vacancy is energetically preferable in cubic phase rather than in the hexagonal structure. Since oxygen ions migrate typically via vacancies in the perovskite lattice [108], the lower oxygen flux through the membrane due to the occurrence of hexagonal phase could also be explained in terms of the reduced oxygen vacancy concentration in the material.

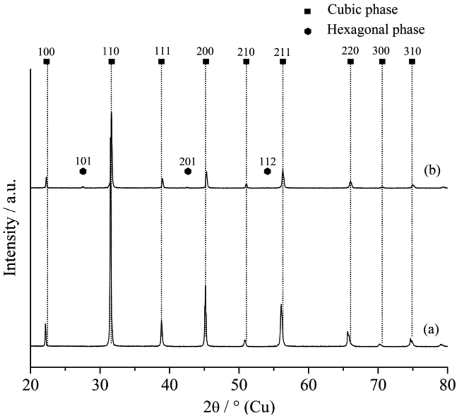

Fig. 5.21 XRD patterns of the 2.0 mm-thick BSCF6482 membranes a) as sintered state; b) after oxygen permeation tests at 850 °C for 2000 h in air/He atmospheres

Besides, the lattice parameters of the cubic perovskite in the bulk change along with the formation of hexagonal phase, as shown in **Tab. 5.9**. As the difference of the ionic radii between the A-site cations is larger than the B-site cations (r_{a} -r_{Sr} $r_{e^{n}}$ -$r_{o^{n}}$; n = +2/+3/+4), this reduction in the lattice parameter of the cube perovskite after long-term operation could be ascribed to the enrichment of Sr^{2+} in the bulk caused by the formation of the Sr-depleted hexagonal phase.

Tab. 5.9 Lattice parameters as well as the hexagonal phase fraction in the BSCF6482 samples as sintered state and after 2000 h permeation measurement at 850 ℃

Samples	Lattice parameters / Å			Hexagonal phase fraction / %
	Cubic	Hexagonal		
		a	c	
after 2000 h test	4.006	5.65	4.35	4
as sintered	4.019	-	-	-

On the other hand, some randomly distributed secondary phases were found in the microstructures of both the interior and the permeate side of the used membrane. Based on the elemental maps in **Fig. 5.22**, the phase A is mainly composed of cobalt-rich oxides along with a strong depletion of strontium, which might be the trigonal phase of approximate composition $Ba_{1-x}Sr_xCo_{2-y}Fe_yO_{5-\delta}$ found in BSCF5582 [95, 134]. However, the composition of phase A here should vary due to the different initial chemical stoichiometries according to the quantification results of EDX in **Tab. 5.10**. Another suggestion was given by Mueller et al. [135] that the phase with significant Co enrichment in combination with a Sr depletion resembles the monoclinic phase proposed by Arnold et al. [96]. As this secondary phase cannot be identified by XRD in this study due to its small volume fraction, its structure remains unknown. Phase B should be the impurities of barium sulphate contained in the raw materials of $BaCO_3$ which was used for BSCF powder production, as small amount of sulphur was detected in the EDX results (see **Appendix E**).

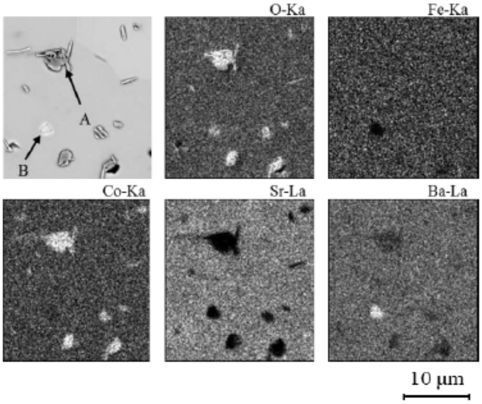

Fig. 5.22 SEM micrograph and EDX elemental distributions of the sweep side of the BSCF6482 membrane after 2000 h oxygen permeation test at 850 °C

Tab. 5.10 Quantitative local chemical compositions of the BSCF6482 membrane after 2000 h oxygen permeation test at 850 °C in atomic percentage

Position	Ba / atom%	Sr / atom%	Co / atom%	Fe / atom%	O / atom%
Bulk	13.7	10.2	16.3	4.2	55.5
Phase A	9.9	2.7	26.2	3.9	57.3
Phase B	21.2	3.7	15.4	0.4	59.3

5.4.2 Long-term permeation measurement at 800 °C

The long-term oxygen permeation behaviour of BSCF membranes with a thickness of 2.5 mm were recorded under the air/He pressure gradient at 800 ℃ for a period of 2000 h. The variation of oxygen flux through the membranes as a function of time in relation to the phase decomposition is discussed in this study.

BSCF4682

The time-dependent oxygen permeation flux through the 2.5 mm-thick BSCF4682 membrane at 800 ℃ for 2000 h is illustrated in **Fig. 5.23**. The oxygen flux at the permeate side of the membrane decreases to 0.38 ml cm^{-2} min^{-1}, namely 41% of its initial value (0.94 ml cm^{-2} min^{-1}) over the entire 2000 h. The deteriorated oxygen permeation rate can be fitted to the exponential equation (shown as the black line):

$$\exp\left(\frac{t}{}\right)$$

As the measured permeation curve shows, the decay of membrane permeability does not reach a steady state over 2000 h and the terminal oxygen permeation rate should approach 0.25 ml cm^{-2} min^{-1} according to **Eq. 5.5**.

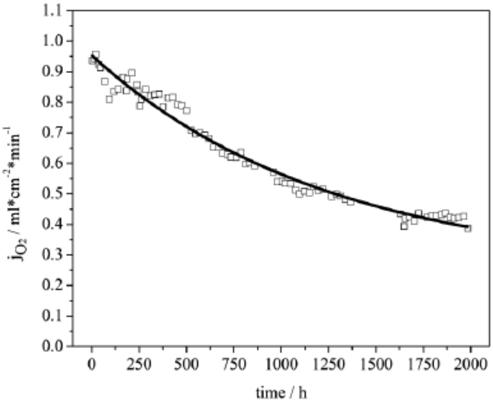

Fig. 5.23 Oxygen permeation flux through the 2.5 mm-thick BSCF4682 membrane at 800 °C for 2000 h under the air/He partial pressure gradient

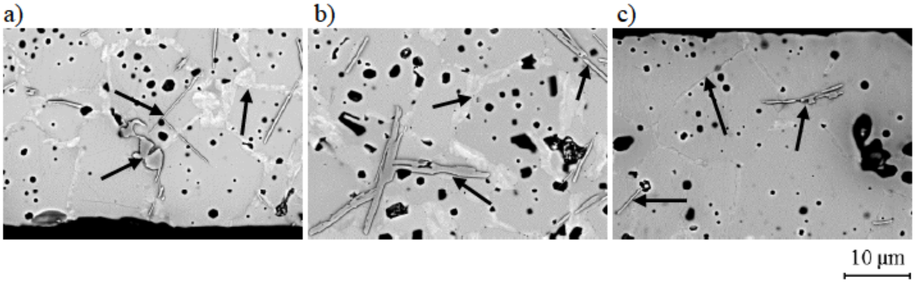

Fig. 5.24 SEM micrographs of a) the feed side; b) the inner part and c) the sweep side of the 2.5 mm-thick BSCF4682 membrane after long-term permeation test at 800 °C for a period of 2000 h under the air/He partial pressure gradient

Compared with the microstructures of the membranes measured at 850 °C, more complex secondary phases were found in the BSCF4682 membrane after 2000 h operation at 800 °C (see **Fig. 5.24**). The compositions of different phases in the SEM micrographs are displayed by elemental maps as shown in **Fig. 5.25**. The plate-like phase A was found to be enriched in cobalt but depleted in strontium, in line with the secondary phase observed at the permeate side of the BSCF6482 membrane after long-term operation at 850 °C. The formation of these cobalt-rich oxides might be attributed to the faster diffusivity of cobalt ions compared to the other cations at intermediate temperatures. A strong depletion of iron is clearly revealed in phase B along with a slight enrichment in cobalt. Combined with the XRD patterns (see **Fig. 5.26**), this Fe-depleted grain boundary phase was confirmed to be hexagonal-structured with reference to [95, 131]. After 2000 h operation at 800 °C, ~23% hexagonal phase was formed in the BSCF4682 membrane (see **Tab. 5.11**), which is regarded as the major reason for the decline of oxygen permeability of the membrane. Similar to the findings in **Fig. 5.20**, phase C is also enriched in cobalt together with higher oxygen stoichiometry compared to the bulk, but it is significantly depleted in strontium and iron (see the linescan results in **Appendix G**). However, this precipitate is too small to be detected by the quantification of the local EDX spectra. Thus, it is suggested that phase C might be another cobalt-enriched oxide with different morphology compared to phase A. This accumulation of cobalt ions in terms of oxides formation results in a reduction of cobalt concentration in the bulk. As the oxygen permeation rate of BSCF membranes increases with cobalt content [32, 136], the formation of these highly cobalt-concentrated oxides in the microstructure may also account for the deterioration of oxygen permeability of this membrane.

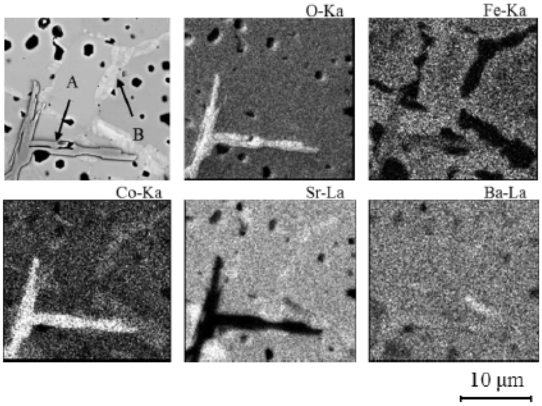

Fig. 5.25 SEM micrograph and EDX elemental distributions of the inner part of the BSCF4682 membrane after 2000 h oxygen permeation test at 800 °C

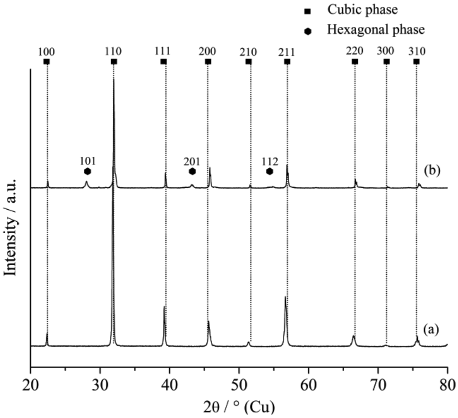

Fig. 5.26 XRD patterns of the 2.5 mm-thick BSCF4682 membranes a) as sintered state; b) after oxygen permeation tests at 800 °C for 2000 h in air/He atmospheres

Tab. 5.11 Lattice parameters as well as the hexagonal phase fraction in the BSCF4682 samples as sintered state and after 2000 h permeation measurement at 800 ℃

Samples	Lattice parameters / Å			Hexagonal phase fraction / %
	Cubic	Hexagonal		
		a	c	
after 2000 h test	3.965	5.58	4.31	23
as sintered	3.978	-	-	-

BSCF5582

Fig. 5.27 shows the oxygen permeability of the 2.5 mm-thick BSCF5582 membranes measured at 800 °C in synthetic air/He atmospheres for 400 h, 800 h and 2000 h respectively. The oxygen permeation rate decreases to 47% of its initial value (0.73 ml cm^{-2} min^{-1}) over the entire 2000 h. The oxygen permeation rate can be fitted to the exponential equation (shown as the black line):

$$\exp\left(\frac{t}{\quad}\right)$$

No steady state could be detected over the long-term operation and the equilibrium oxygen flux through the membranes should approach 0.23 ml cm^{-2} min^{-1} according to the exponential fitting equation. These results are in good agreement with the findings in [55, 91, 95]

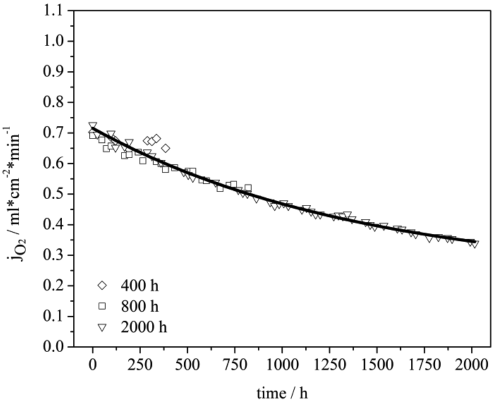

Fig. 5.27 Oxygen permeation flux through the 2.5 mm-thick BSCF5582 membrane at 800 °C for 400, 800 and 2000 h under the air/He partial pressure gradient

The ongoing formation of noncubic perovskites in the membranes was recorded by XRD after different periods of permeation tests at 800 °C (see **Fig. 5.28**). It was found that the occurrence of hexagonal phase is already detectable after 200 h with the emerged additional intensities of the reflected peaks corresponding to hexagonal structure in the XRD patterns. Similar findings in BSCF5582 were reported by in situ XRD analysis at temperatures below 800 ℃ [137]. Moreover, the reflection signal for hexagonal phase becomes more pronounced with the extension of operation time, especially the intensity of the main peak of (101) plane around °. This indicates a growing hexagonal phase fraction in the bulk of the used membranes, which is confirmed in **Fig. 5.29**.

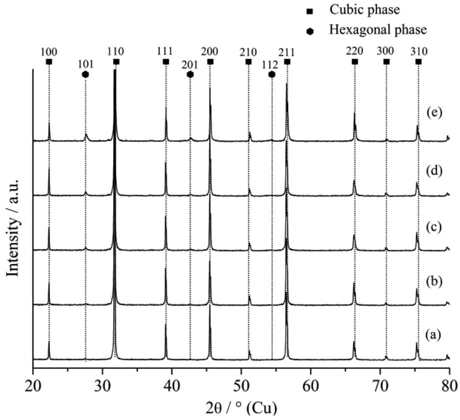

Fig. 5.28 XRD patterns of the 2.5 mm-thick BSCF5582 membranes after oxygen permeation tests at 800 °C for a) 200 h; b) 400 h; c) 600 h; d) 800 h; e) 2000 h in air/He atmospheres

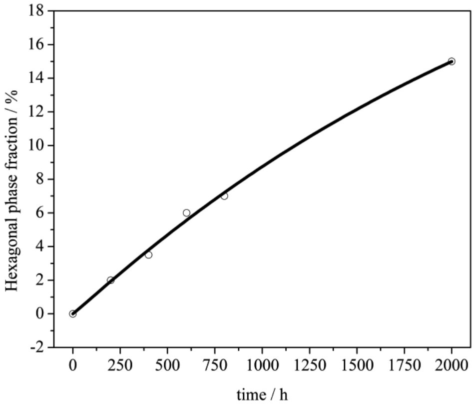

Fig. 5.29 Growth of hexagonal phase in the 2.5 mm-thick BSCF5582 membranes after oxygen permeation tests at 800 °C in air/He atmospheres

The kinetic growth of hexagonal phase in the perovskite lattice can be described by a modified Johnson-Mehl-Avrami (JMA) model [138],

$$\alpha_{hex}(t) \quad \alpha_{hex}(t \quad)\,(\quad e^{kt^{n}})$$

$\alpha_{hex}(t)$	volume fraction of hexagonal phase in the membrane at time t
$\alpha_{hex}(t \quad)$	equilibrium hexagonal phase fraction
k	rate constant for decomposition process
n	the Avrami exponent

Considering the fitting parameters in the curve, $\alpha_{hex}(t \quad) = 28.49 \pm 16.12\%$, $k = (0.0079 \pm 0.0016)\ h^{-n}$ and $n = 1.03 \pm 0.16$. The approximate unity value of n could be related to the grain-boundary nucleation that results in a fast saturation of nucleation sites [139]. This was also proposed by Niedrig et al. that the formation of hexagonal phase occurs predominantly at the grain boundaries as they compared the long-term conductivity of three BSCF5582 membranes with different average grain sizes measured for more than 1300 h at 800 ℃ in ambient air [97]. Therefore, it is reasonable for the equilibrium volume fraction of hexagonal phase to approach only 28.49% as a consequence of the limited nucleation sites for phase transformation. In order to confirm this assumption, the SEM micrographs of the cross sections of the used membranes after different oxygen permeation periods are exhibited in **Fig. 5.30**. It is apparent that secondary phases were formed mainly at the grain boundary sites and a steady growth of the major grain boundary phase could be found with the extension of time. At the feed side of the membrane, microstructural deterioration was also observed inside the grains after 2000 h operation, compared to others with shorter operation time in which decomposition occurs predominantly along grain boundaries. This implies that nucleation would be initiated in the bulk grains after the saturation of nuclei in the grain boundary until the decomposition reaction reaches equilibrium. However, it should be emphasized that the nucleation of hexagonal phase within the grains would be strongly impeded due to the structural dissimilarity and hence to the large driving force required. During the long-term oxygen permeation test at 800 ℃ , the initial cubic perovskite decomposes into an equilibrium mixture of a hexagonal phase and a Sr- and Fe-enriched cubic perovskite phase, that is,

$$a \quad Sr \quad o \quad e \quad {}^{\text{cub, educt}}_{\delta}$$

$$- a \quad {}_{x} Sr \quad {}_{x} o \quad {}^{\text{hex, product}}_{\delta} \quad - a \quad {}_{x} Sr \quad {}_{x} o \quad e \quad {}^{\text{cub, product}}_{\delta}$$

According to the fitting parameters in **Eq. 5.7**, the fact that $\alpha_{hex}(t)$ cannot reach unity indicates that the observed reaction is a kinetic decomposition process rather than a phase transformation, being consistent with the suggestions by Mueller et al. [131]. In combination with the permeate fluxes through the membranes in **Fig. 5.27**, it could be concluded that the severer deterioration of the microstructure, or the larger content of hexagonal phase in the membrane, the more significant decay of the oxygen permeability was obtained. In other words, results in this study support the proposition that the decline of the oxygen permeation stability of BSCF membranes at 800 ℃ is mainly caused by the partial decomposition from cubic into lower symmetry-structured hexagonal phase during the long-term measurement [95, 134]. In addition, the concentration of mobile oxygen vacancies in the perovskite decreases with operation time [58, 91], which could be another reason for the deterioration of oxygen permeability of the membranes. Thirdly, the variation of cation concentrations in the cubic perovskite as a result of the formation of noncubic phases should also be taken into account for the oxygen permeation behavior of the membranes.

Microstructures in **Fig. 5.30** show an interesting phenomenon that severer decay was observed at the air supply side than at the helium sweep side of the used membranes. It appears that the formation of hexagonal phase is favored in the regions with high oxygen concentration, e.g., grain boundaries. According to the transmission electron microscope investigations by Liang et al. [134], the hexagonal phase grows along cubic $<110>_c$ directions, which coincides with the average global directions of oxygen migration in cubic perovskite. This leads to the assumption that cobalt ions in BSCF are prone to migrating towards grain boundary sites due to the higher oxygen content in these regions compared to the bulk. The cationic cobalt could then be easily oxidized there and change their ionic radii and spin-states by virtue of the strongly oxidizing local conditions, which conduces to the formation of hexagonal phase. Moreover, hexagonal phase often possesses a higher oxygen stoichiometry than the cubic perovskite and the phase transition process should hence be accelerated by higher oxygen partial pressure [58, 132], i.e. high oxygen pressure would shift the equilibrium to the decomposed products. This statement is in line with the observation here that the formation of secondary phase was more pronounced at the feed side of the membrane.

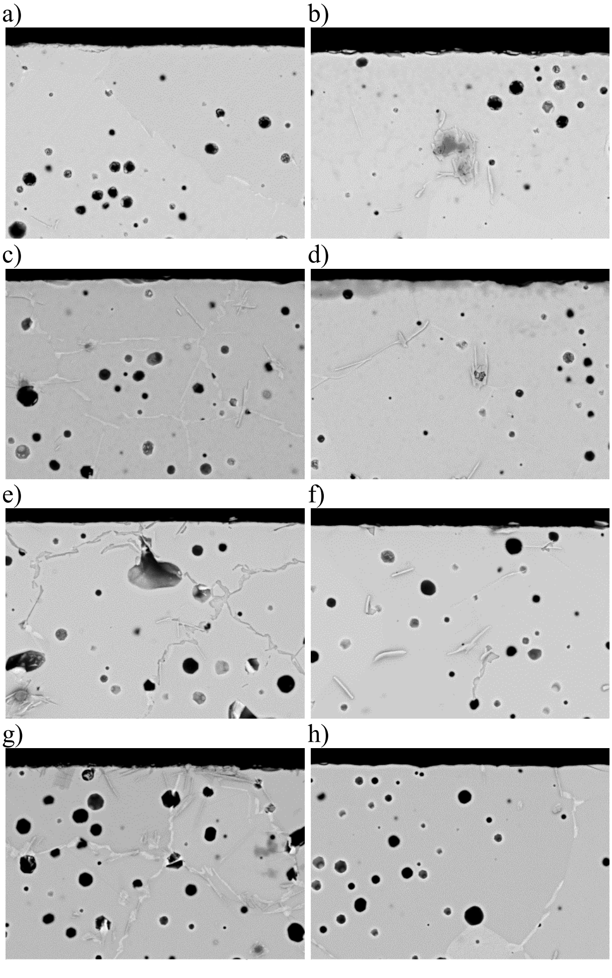

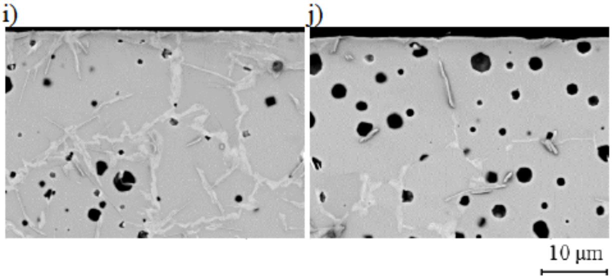

Fig. 5.30 SEM micrographs of the 2.5 mm-thick BSCF5582 membranes after long-term permeation tests at 800 °C for various periods: a) 200 h at the feed side; b) 200 h at the sweep side; c) 400 h at the feed side; d) 400 h at the sweep side; e) 600 h at the feed side; f) 600 h at the sweep side; g) 800 h at the feed side; h) 800 h at the sweep side; i) 2000 h at the feed side; j) 2000 h at the sweep side of the membranes under the air/He partial pressure gradient

BSCF6482

The oxygen permeation flux through the 2.5 mm-thick BSCF4682 membrane measured at 800 °C is displayed in **Fig. 5.31** as a function of operation time. The oxygen permeation flux at permeate side of the membrane declines fast to only 24% of its initial value (0.91 ml cm^{-2} min^{-1}) over the entire 2000 h. The decay of oxygen permeability could be described by this exponential equation (shown as the black line):

$$\exp\left(\frac{t}{\quad}\right)$$

Compared to other membranes that cannot achieve equilibrium flux after the long-term measurement, the oxygen permeation rate of the BSCF6482 membrane over 2000 h is quite close to the equilibrium value of 0.21 ml cm^{-2} min^{-1} in **Eq. 5.5**. A stable permeate flux of the membrane was obtained after t ≈ 1600 h. Thus, severe deterioration of the microstructural properties could be predicted in this membrane.

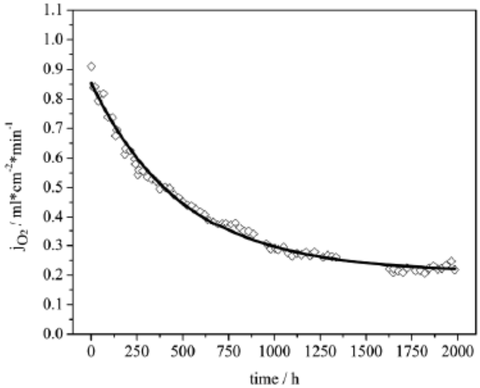

Fig. 5.31 Oxygen permeation flux through the 2.5 mm-thick BSCF6482 membrane at 800 °C for 2000 h under the air/He partial pressure gradient

In order to elucidate the rapid decay of the membrane permeability, the cross sections of the used membrane were analyzed by SEM in different regions and the microstructures are illustrated in **Fig. 5.32**. It is evident that quite severe deterioration of the microstructure occurs at feed side of the used membrane after the long-term operation, while relatively fewer secondary phases were found at the permeate side. In combination with the EDX results in **Tab. 5.12**, the Fe-depleted phase A with an enrichment of cobalt should be related to the hexagonal phase detected in the XRD patterns (see **Fig. 5.33**). From **Tab. 5.13**, nearly 27% hexagonal phase was found in the used membrane over the 2000 h operation. The plate-like phase B is similar to the cobalt-enriched phase observed in the used BSCF4682 membrane tested at 800 °C. Moreover, another secondary phase C appears in the microstructure of this membrane with a significant depletion of strontium and iron.

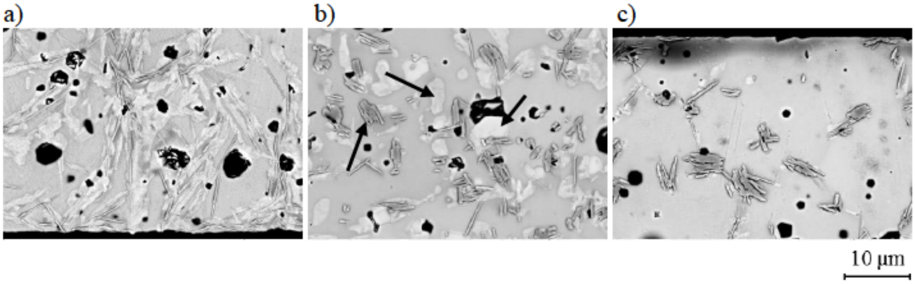

Fig. 5.32 SEM micrographs of a) the feed side; b) the inner part and c) the sweep side of the 2.5 mm-thick BSCF6482 membrane after long-term permeation test at 800 °C for a period of 2000 h under the air/He partial pressure gradient

Tab. 5.12 Quantitative local chemical compositions of the BSCF6482 membrane after 2000 h oxygen permeation test at 800 °C in atomic percentage

Position	Ba / atom%	Sr / atom%	Co / atom%	Fe / atom%	O / atom%
Bulk	13.5	10.4	15.2	5.3	55.6
Phase A	13.4	11.5	18.4	0.7	56.0
Phase B	9.1	2.6	27.7	4.4	56.1
Phase C	19.7	4.3	15.1	0.3	60.5

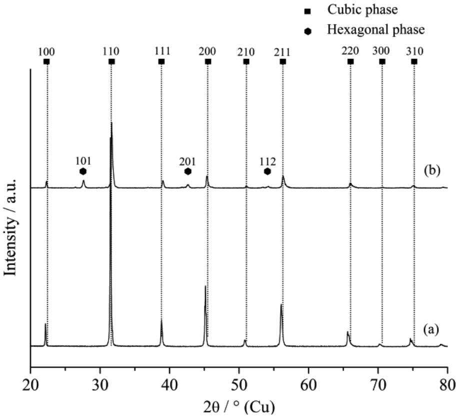

Fig. 5.33 XRD patterns of the 2.5 mm-thick BSCF6482 membranes a) as sintered state; b) after oxygen permeation tests at 800 °C for 2000 h in air/He atmospheres

Tab. 5.13 Lattice parameters and the hexagonal phase fraction in the BSCF6482 samples as sintered state and after 2000 h permeation measurement at 800 ℃

Samples	Lattice parameters / Å			Hexagonal phase fraction / %
	Cubic	Hexagonal		
		a	c	
after 2000 h test	4.006	5.64	4.34	27
as sintered	4.019	-	-	-

In order to investigate the structures of these complex secondary phases which cannot be indexed by XRD, EBSD analysis of the used membrane was performed. Interesting to note, the used membrane consists of a three phase mixture, i.e. a hexagonal, a cubic, as well as a monoclinic phase. The creation of the monoclinic-structured phase was also reported by Arnold et al. [96]. According to their postulations, the cubic perovskite phase transforms via an intermediate structure of monoclinic stacking sequence towards the hexagonal polymorph. On this basis, it could be addressed that the monoclinic phase with a mixture of cubic and hexagonal stacking sequences is more compatible with the cubic matrix and it should be preferentially formed prior to the hexagonal perovskite during the decomposition process. Therefore, the formation of this plate-like monoclinic phase (shown as the yellow area in **Fig. 5.34**) might be correlated to the phase transition kinetics between cubic and hexagonal perovskites. Furthermore, phase B in the SEM micrograph in **Fig. 5.32** seems to be a coexistence of the three-phase mixture according to the EBSD results, which surrounds the formed hexagonal phase. This could be another sign for the relation of this monoclinic phase to the cubic-hexagonal phase transition in the perovskite oxide. In the case of the BSCF6482 composition, the decomposition process could be summarized as the cubic perovskite tends to decompose into its end members: the cubic-structured $SrFeO_3$ and the hexagonal $BaCoO_3$. However, complete demixing might not occur, since the cubic perovskite product has a tolerance towards Ba composition (see the EDX results in **Tab. 5.12**). In contrast, severe redistribution of B-site cations was observed in this material as a nearly complete depletion of iron occurs in the hexagonal phase. The repulsion of iron could be explained as a consequence of the decomposition kinetics that iron preferably occupies the corner-sharing octahedral sites in cubic perovskite, while the Co cations commonly occupy the face-sharing octahedral of the hexagonal structure [96]. Combined with the microstructural observations in this membrane, it could be presumed that phase transition from cubic towards hexagonal perovskite would be preferred in Co-rich BSCF materials.

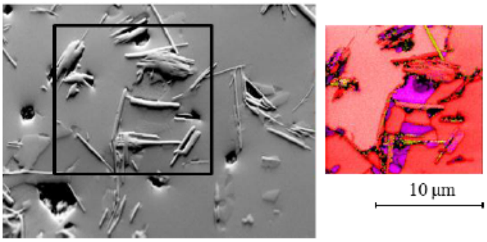

Fig. 5.34 SEM micrograph and EBSD map of the BSCF6482 membrane after long-term operation at 800 °C for 2000 h under the air/He pressure gradient

Tab. 5.14 The phase structure and volume fractions in **Fig. 5.34**

	Structure	Formula	Fraction
🟥	cubic	$SrFeO_3$	79.3%
🟪	hexagonal	$BaCoO_3$	10.0%
🟨	monoclinic	Ba_2CoO_4	3.5%
⬛	porosity	-	7.2%

5.4.3 Influence of cations on the permeation stability of BSCF membranes

The improvement of oxygen transport in perovskite membranes by proper doping of A- and B-site cations is a general trend suggested in several publications [32, 47, 61, 89, 105]. Nevertheless, few comments have been made about the influence of chemical composition on the oxygen permeability and stability of BSCF membranes. In this study, the oxygen permeation rates of BSCF membranes as a function of operation time are illustrated in **Fig. 5.35** and **Fig. 5.36**. Here, in order to represent the change of membrane permeability with time more clearly, another parameter denominated the relative oxygen permeation rate is introduced,

$$\text{elative} \qquad \frac{t}{t}$$

The fitting parameters in the exponential equation for each permeation curve as well as the relative oxygen fluxes through the membranes over 2000 h measurement are summarized in **Tab. 5.15**. If comparing the oxygen permeability of the membranes at 850 °C, complete opposite tendency was discerned. Though the oxygen flux of BSCF4628 is much lower than that of BSCF6482 at the beginning of the measurement, it increases continuously with time whereas the permeation rate of BSCF6482 declines, as observed in the relative permeation curves. Thereafter, an intersection point of both permeation curves could be estimated with further extension of the operation time to more than 2000 h. It should be noted that the increasing rate of oxygen permeability in BSCF4628 is faster than the decreasing rate in the BSCF6482 membrane. The absolute value of t_1, which represents the variation rate of the membrane permeability, is 3157.38 h for BSCF4628 and 9712.74 h for BSCF6482. The different oxygen permeation behaviors of both materials could be assigned mainly to the cobalt concentration in the perovskites. Firstly, the BSCF6482 material containing more cobalt exhibits much improved oxygen permeability with nearly twice the permeation rate of the BSCF4628 membrane. The reason for this enhancement of oxygen flux with cobalt concentration could be various. It was reported that the activation energies of oxygen permeation process decrease by increasing the Co content [92, 140, 141], resulting in an increment of the membrane permeation rate. In addition, the formation energy of oxygen vacancies drops linearly with the cobalt content in BSCF materials [56]. This means higher concentration of oxygen vacancy could be formed in perovskites with higher cobalt content, which prompts oxygen transport through the membrane. Moreover, doping with cobalt yields an increase in the electronic conductivity of BSCF perovskites [57].

Secondly, as discussed in **Chapter 5.4.1**, the decay of oxygen permeability in the BSCF6482 membrane is mainly attributed to the formation of noncubic phases as a direct consequence of cobalt ions migration. While, for the BSCF4628 membrane, the increase in oxygen flux with time is ascribed to the combination of grain growth as well as the improved surface roughness after operation. During the long-term operation at 850 °C, oxygen release would occur in the membranes along with the reduction of B-site cations towards lower valency, e.g., Co^{4+}/Fe^{4+} to Co^{3+}/Fe^{3+}. Accordingly, different decomposition kinetics in both BSCF membranes might be related to the smaller bonding energy of Co^{3+} to oxygen ions in comparison with Fe^{3+} [57, 142]. Thus, the more cobalt the perovskite contains, the easier the noncubic phases form at intermediate temperatures. The experimental observations is also consistent with the tolerance factors of BSCF discussed in **Chapter 5.1.1** that it is more difficult for Co-rich BSCF materials to obtain cubic perovskite.

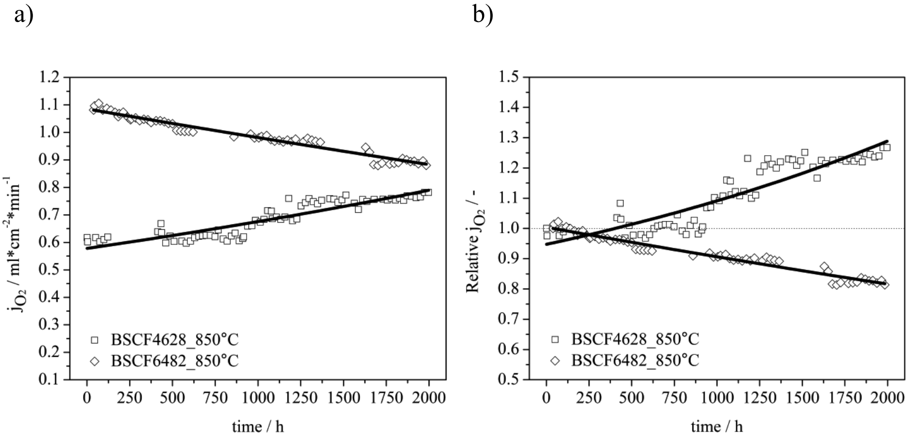

Fig. 5.35 a) Oxygen permeation flux and b) the relative oxygen permeation rate through the 2.0 mm-thick BSCF membranes at 850 °C for 2000 h under the air/He pressure gradient

In the case of oxygen permeability of the membranes at 800 °C (see **Fig. 5.36 a**), the long-term oxygen fluxes follow this sequence: BSCF4682 > BSCF5582 > BSCF6482, although it should be noticed that the initial permeation value of BSCF5582 is lower than that of BSCF6482 at the operation time shorter than ~180 h. The lower permeation rate obtained in BSCF5582 membrane could be ascribed to its smaller grain size compared to other membranes [63]. Nevertheless, the result implies that the membrane permeability increases with the reduction of barium concentration in the perovskite. However, the findings in the study is contrary to the general concept that the oxygen permeability should increase with barium content due to its larger ionic radius compared with Sr^{2+}, resulting in the reduction of the repulsive interaction and thus the increase in the mobility of oxygen ions [105, 143]. Based on the investigation of barium doping effect in SCF by Shao et al. [89], the dependence of oxygen permeability on barium content with oxygen stoichiometry in the range of 0.3-0.7 agrees with the observations in this study. They found that the maximum oxygen flux was achieved in the BSCF3782 membrane, followed by the BSCF5582 membrane and BSCF7382 showed the lowest oxygen permeability. One reason for the enhancement of oxygen permeability with lower barium content could be correlated with the measured change of oxygen nonstoichiometry in BSCF materials in **Fig. 5.13**. It seems that the creation of oxygen vacancy is virtually decelerated by doping with barium. In other words, the oxygen vacancy concentration in the perovskites is more important than the oxygen ions mobility to oxygen transport in the investigated BSCF membranes.

Unlike the clear dependence of oxygen permeability with barium content, the long-term permeation stability of BSCF membranes was found to be in the sequence of BSCF5582 > BSCF4682 > BSCF6482. The decay rates of membrane properties in BSCF4682 and BSCF5582 membranes are similar to each other as depicted in **Fig. 5.36 b**, which could also be postulated from the t_l values in **Tab. 5.15** (t_l = 1244.74 h for BSCF4682 and t_l = 1423.12 h for BSCF5582). However, a fast deterioration of membrane permeability was observed in BSCF6482 and the oxygen flux shows a plateau approaching the equilibrium value (0.21 ml cm^{-2} min^{-1}) over the entire 2000 h. Considering the possible influence of membrane production process on the permeation properties of BSCF4682 and BSCF5582 membranes, the improved membrane performance of BSCF5582 might not only come from the difference of chemical composition when compared to BSCF4682. Nevertheless, it could be concluded from the permeation behaviors of BSCF4682 and BSCF6482 membranes that the oxygen permeability of the membranes is stabilized with less barium content. This is consistent with the findings in [105]. As barium ions possess larger ionic radius than strontium, the lattice expansion caused by the addition of barium then favors the formation of lower Co oxidation states because the change of cobalt ions to lower valence is coupled with an increase in the ionic radius (Co^{4+} to Co^{3+} by 0.08 Å, Co^{3+} to Co^{2+} by 0.1 Å). Therefore, the formation of Co-rich secondary phases in the microstructure is prompted by doping with barium, which accounts for the dramatic drop of oxygen permeability in the BSCF6482 membrane. In addition, it is more difficult for Ba-rich perovskite oxides to maintain cubic structure in regard to the tolerance factor, which also supports the experimental results presented here.

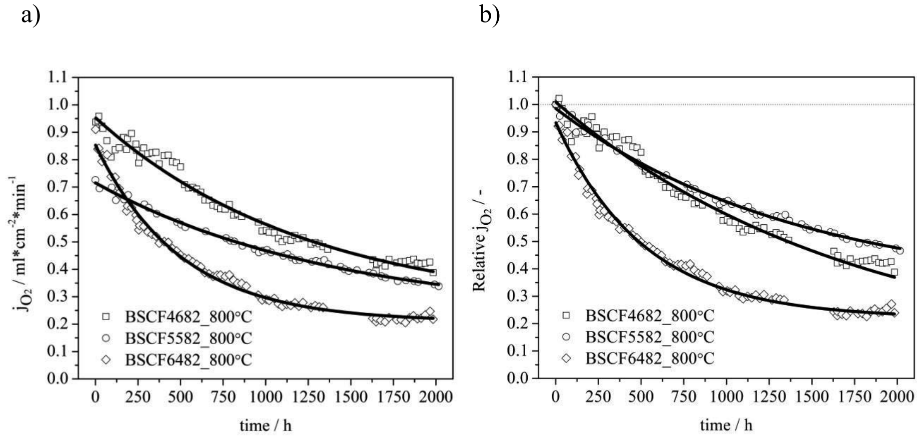

Fig. 5.36 a) Oxygen permeation flux and b) the relative oxygen permeation rate through the 2.5 mm-thick BSCF membranes at 800 °C for 2000 h under the air/He pressure gradient

Tab. 5.15 Fitting parameters of the oxygen permeate fluxes through the BSCF membranes according to $\exp\left(-\frac{t}{t}\right)$ as well as the relative permeation rate after 2000 h operation in the oxygen permeation tests

T / °C	Materials	Fitting parameters			relative
		A / ml cm^{-2} min^{-1}	t_1 / h	j_0 / ml cm^{-2} min^{-1}	(t = 2000 h)
850	BSCF4628	0.24	-3157.38	0.35	1.27
	BSCF6482	1.09	9712.74	0.12	0.81
800	BSCF4682	0.70	1244.74	0.25	0.39
	BSCF5582	0.49	1423.12	0.23	0.47
	BSCF6482	0.65	500.08	0.21	0.24

5.4.4 Temperature effect on the permeation stability of BSCF membranes

The long-term oxygen permeation stability of BSCF6482 membranes was measured at 800 °C and 850 °C under the air/He pressure gradient (see **Fig. 5.37**). The results show that the operation temperature has a considerable effect on the oxygen flux as both membranes have similar membrane thicknesses of 2.0 mm and 2.5 mm respectively. This increment of oxygen permeability with temperature could be assigned to the higher concentration of oxygen vacancies in the lattice, which is responsible for oxygen transport through the membrane. Another reason for this flux enhancement is the reduction of permeation resistance with respect to the increased oxygen diffusion rate and the surface exchange rates at higher temperatures [144].

Moreover, the oxygen permeation stability of membranes at 850 °C was greatly improved compared to the lower temperature of 800 °C. The relative permeation flux through the membrane measured at 850 ℃ declines only ~12% of its initial value in comparison with a reduction of ~76% for the membrane measured at 800 °C. This large difference of membrane permeation behaviours by 50 °C increment of operation temperature could be ascribed to the influence of temperature on the kinetic decomposition process in the membranes. Based on the XRD patterns in **Fig. 5.38**, the intensity of the peaks indexed as hexagonal phase becomes more pronounced in the membrane tested at 800 °C, corresponding to a hexagonal phase fraction of 27% in the perovskite. A smaller amount of hexagonal phase was detected in the membrane tested at 850 °C with a value of only 4% in accordance with the less significant reflection signal of hexagonal phase observed in the XRD patterns. Combined with the oxygen permeation behaviours of the membranes, the faster decay rate in the membrane measured at 800 °C could be considered as a result of the larger amount of hexagonal phase created in perovskite lattice, which hinders the transport of oxygen ions. At higher temperature of 850 °C, it seems the formation of hexagonal phase is suppressed and the deterioration of membrane performance is hence retarded. In short, the temperature increase by 50 °C could certainly improve the oxygen permeability as well as the long-term stability of BSCF membranes due to the suppressed phase decomposition of cubic towards hexagonal morphology.

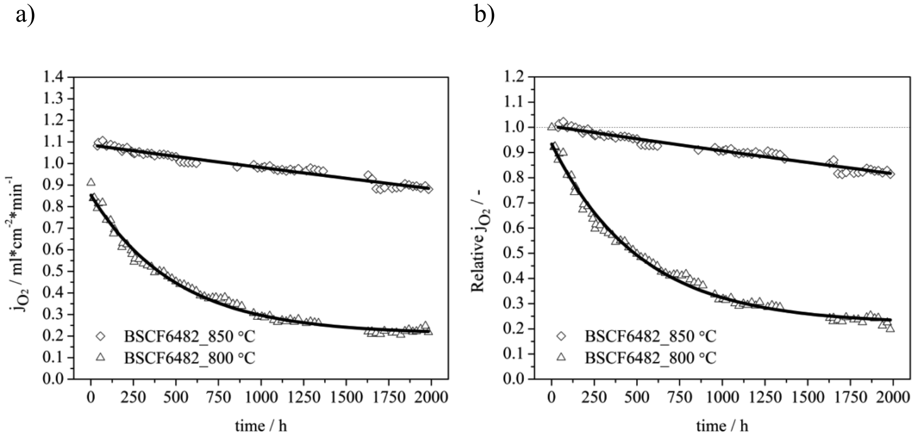

Fig. 5.37 a) Oxygen permeation flux and b) the relative oxygen permeation rate through the 2.5 mm-thick BSCF6482 membrane at 800 °C as well as the 2.0 mm-thick membrane measured at 850 °C for 2000 h under the air/He pressure gradient

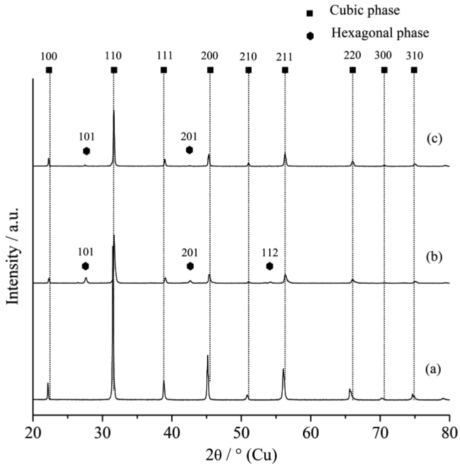

Fig. 5.38 XRD patterns of the BSCF6482 membranes a) as sintered state; b) after oxygen permeation tests at 800 °C for 2000 h; c) after oxygen permeation tests at 850 °C for 2000 h in air/He atmospheres

5.4.5 Influence of membrane thickness on the permeation stability of BSCF membranes

If the oxygen permeation process is rate-determined by bulk diffusion kinetics for thick membranes, reducing membrane thickness is an effective way to improve the flux [143, 145]. In order to determine the effect of membrane thickness on the oxygen flux as well as the long-term permeation stability, BSCF5582 membranes with a thickness of 1.0 mm or 2.5 mm were prepared respectively. **Fig. 5.39** shows the oxygen permeation behaviors of the membranes measured at 800 °C under the air/He partial pressure gradient for 2000 h. It is apparent that the 1.0 mm-thick membrane exhibits higher oxygen fluxes compared to the 2.5 mm membrane over the entire 2000 h. At the beginning of the measurement, the oxygen flux through the 1.0 mm-thick membrane is about 88% higher than that of the 2.5 mm-thick membrane. For slow bulk diffusion controlled membranes, the oxygen permeation flux should be proportional to the reciprocal of the membrane thickness according to the Wagner relation [146]. However, the permeate flux of the 1.0 mm-thick membrane is lower than the calculated value with respect to Wagner equation on the assumption that the permeation rate of the 2.5 mm-thick membrane is controlled by bulk diffusion. In other words, surface reaction resistance becomes more significant to the permeation process in the 1.0 mm-thick membrane and Wagner equation is invalid in this case.

In view of the permeation stability, the oxygen flux through the 1.0 mm-thick membrane decreases from 1.36 ml cm^{-2} min^{-1} to 0.46 ml cm^{-2} min^{-1}, namely 34% of its initial value over the 2000 h operation. According to the relative permeation curves, the decay rates of both membranes are quite similar to each other with short operation time and differences arise gradually when the operation time is longer than ~1200 h. As hexagonal phase grows continuously in the membrane during the permeation measurement (see **Fig. 5.29**), the different permeation decay rates for both membranes after long-term operation could be related to the formation of this noncubic perovskite phase. It means that the occurrence of hexagonal phase in the microstructure plays a more important role in the permeation stability of the thin membrane compared to the thick one under the same operation condition, especially when the hexagonal phase fraction exceeds a critical value. From the SEM micrographs of the used membranes in **Fig. 5.40**, severer deterioration of membrane microstructure was observed in the 1.0 mm-thick membrane than in the 2.5 mm-thick one, e.g. more hexagonal phase as well as the plate-like secondary phase was formed at the both sides of the thin membrane. This probably implies that the kinetic decomposition process is accelerated by reducing the membrane thickness over the long-term operation.

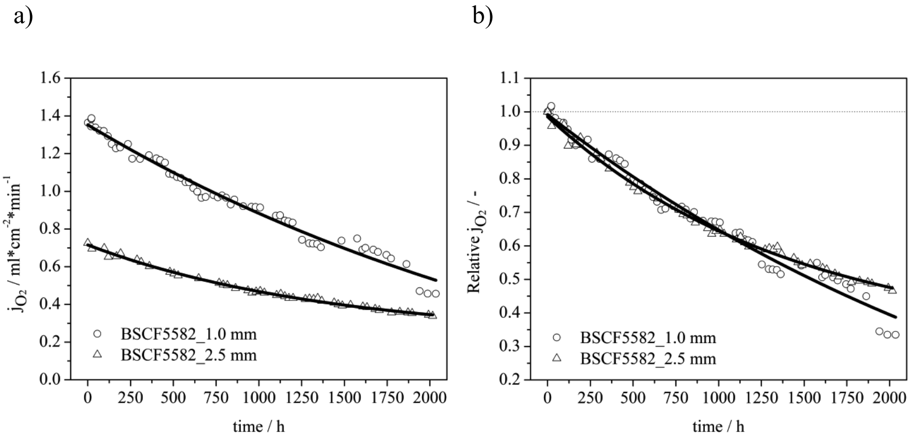

Fig. 5.39 a) Oxygen permeation flux and b) the relative oxygen permeation rate through the 1.0 mm- and 2.5 mm-thick BSCF5582 membranes at 800 °C for 2000 h under the air/He pressure gradient

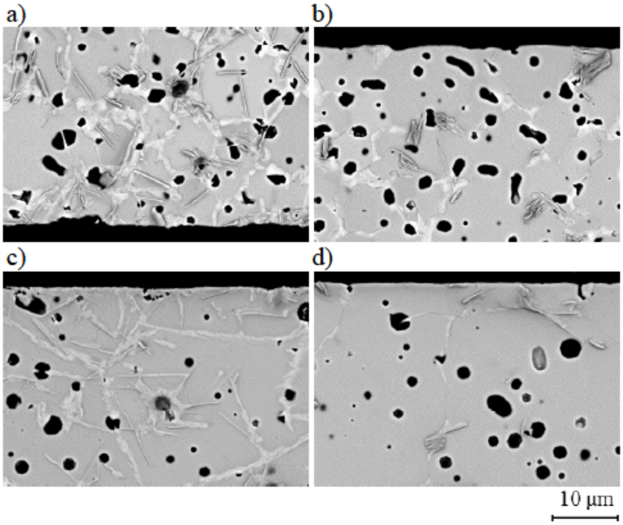

Fig. 5.40 SEM micrographs of a) the feed side and b) the sweep side of the 1.0 mm-thick BSCF5582 membrane; c) the feed side and d) the sweep side of the 2.5 mm-thick BSCF5582 membrane after long-term permeation test at 800 °C for a period of 2000 h under the air/He partial pressure gradient

5.5 Cyclic permeation measurement of BSCF membranes

As discussed in **Chapter 5.4**, the long-term permeation fluxes through BSCF membranes change during operation at intermediate temperatures. A significant influence of temperature on the phase stability of perovskite oxides was observed in the permeation measurements. In order to further clarify the temperature impact on the long-term stability of membrane performance, a cyclic permeation measurement was conducted in a wide temperature range of 700-900 °C. Moreover, the effect of cyclic treatment on the membrane performance after long-term operation at 800 °C for 2000 h was also investigated in the BSCF6482 membrane.

BSCF5582

The oxygen permeability of the BSCF5582 membrane with a thickness of 2.0 mm measured in a temperature range of 700-900 °C under the air/He partial pressure gradient is illustrated in **Fig. 5.41**. Before periodically changing the temperature, the membrane was held at 800 °C for ~90 h. During this period, the oxygen permeability decreases slightly by ~6% with time, which is mainly attributed to the phase decomposition in the perovskite as discussed in the previous chapter. Then the temperature was enhanced to 900 °C and a gradual improvement of oxygen permeability could be observed. It is obvious that the retrieve of membrane performance at high temperatures affords a clear evidence for the reversibility of the cubic-hexagonal phase transition process. Moreover, Švarcová et al found that the phase separation into the two-phase region of hexagonal and cubic polymorphs was reversible in raw powders [98], which agrees with the observations here in the permeation behaviour of the membrane. By decreasing the temperature back to 800 °C, the oxygen permeation shows a steeper decline tendency in contrast to the previous cycle at the same temperature. However, it should be argued that the initial oxygen flux in this case is higher than the one measured at the beginning of the measurement at 800 °C. This non-stationary permeability of the membrane could be interpreted from two aspects. One is the diffusion rate of each component, which changes as a function of time. It means there would be a delay for the variation of the diffusivity of constitutes participating in the oxygen transport as a consequence of the abrupt temperature change. Another is the contribution from the time-dependent loss of lattice oxygen that decreases with the extension of time as well as the drop of temperature. Results from the subsequent temperature cycles suggest that the decline of membrane permeability is more obvious at 700 °C, which is consistent with the findings in [91]. Comparing the oxygen fluxes of the first short-term cycles in the range of 700-800 °C, the rapid decrease in the membrane permeability appears to be continuous for each temperature despite of the interruption of other temperature cycles in between. It implies that the drop rate of oxygen permeability of the membrane is not influenced by temperature variation in this range and phase decomposition is supposed to occur in the material over these cycles at temperatures lower than 800 ℃ . At higher temperature of 850 °C, a fast increase in the oxygen flux from 0.49 ml cm^{-2} min^{-1} to 0.85 ml cm^{-2} min^{-1} in 72 h was observed. This large improvement of membrane performance may not only come from the temperature effect on oxygen transport mechanism but also the phase transition from low symmetric hexagonal phase to highly symmetric cubic perovskite in the high temperature range [70, 96]. Afterwards, there is a great enhancement of membrane permeability at 800 °C compared to the previous one, suggesting the short-term temperature cycle at 850 °C could significantly improve the oxygen permeation behaviour of the membrane after operation in the lower temperature range. On the contrary, a dramatic drop of oxygen permeation was obtained at the sequential 750 °C, which is more obvious than the previous cycle at the same temperature. This indicates the growing instability of the membrane performance in the low temperature range, where phase transition is triggered, after restoring its oxygen permeability at high temperatures.

The extremely high oxygen permeation in the second long-term cycle at 900 °C was unexpected here, as the membrane was supposed to show a deterioration of oxygen permeation behaviour in view of partial decomposition that may occur during the previous cycles in the low temperature range. The reason for this increment of oxygen permeability at the second cycle of 900 °C remains unclear and further investigation of the membrane properties after this cycle is required. Though the initial permeation rate of the second long-term cycle is higher than the first one, it decreases much faster and the oxygen fluxes at the second temperature cycle of 700 °C are nearly the same to the fluxes at the same temperature cycle during the first long-term cyclic operation. Similar oxygen permeation behaviour was detected in the subsequent temperature cycles during the second long-term treatment till temperature was raised to 850 °C. There, the permeation rate of the membrane at the end of this cycle was much lower compared to the one during the first long-term measurement. It implies that the potential for the membrane to retrieve its performance by increasing temperature is limited through cyclic measurement. Nevertheless, the oxygen permeation rates at 900 °C in the third cycle are just in the same range compared to the first long-term cycle at the very beginning. Similar observation was also found in the subsequent temperature cycle at 800 °C. Again, it seems the membrane permeability could be reserved over the entire cyclic permeation in contrast to the deteriorative performance of membranes during long-term operation at intermediate temperatures as displayed in **Fig. 5.27**.

In conclusion, the decline of oxygen permeation flux through the membrane with time occurs in the temperature range of 700-800 ℃ . However, the membrane performance could be retrieved by increasing temperature above 850 ℃ and the periodical membrane performance was found over the cyclic permeation measurement. The reason for the long-term stability at higher temperatures than 850 °C could be attributed to the redox behaviour of B-site cations, especially the cobalt ions. As a matter of fact, the B-site cations of perovskite possess higher oxidation states at lower temperatures and the rise in temperature would result in a reduction of B-site cations [96]. Thus, the phase transition is indeed induced by the decrease in the ionic radii of B-site cations. Moreover, the oxidation of cobalt ions from Co^{2+} to Co^{3+} is coupled with a change of the preferred spin state, which is regarded as the driving force for the formation of hexagonal phase [96]. The restoration of membrane performance at higher temperatures supports the proposition that the cubic-hexagonal phase transition is reversible and cubic polymorph is preferred in the high temperature range above 850 ℃ . This is in good agreement with the observations in [70, 89, 91]. According to the Goldschmidt factors, a meta-stability of the cubic perovskite in BSCF materials was predicted (see **Chapter 5.1.1**). Increasing temperature would conduce to the formation of oxygen vacancy in the lattice in combination with the reduction of B-site transition cations. Therefore, the occurrence of cubic perovskite is favoured at high temperatures due to the presence of larger cations compared to the oxidized ones at lower temperatures.

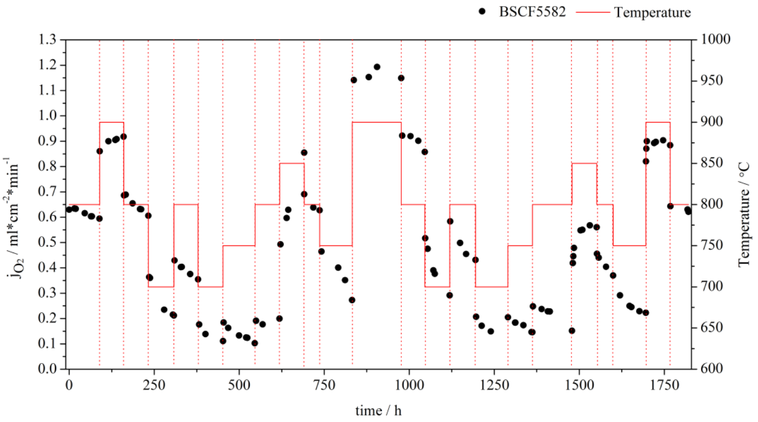

Fig. 5.41 Oxygen permeation fluxes through the 2.0-mm thick BSCF5582 membrane as a function of time in a temperature range of 700-900 °C under the air/He partial pressure gradient

Fig. 5.42 shows the SEM micrographs of the used membrane after cyclic long-term permeation measurement in the temperature range of 700-900 ℃ . Only a small amount of hexagonal phase could be detected along grain boundaries at the feed side of the membrane. In the meanwhile, there is a plate-like secondary phase found in the microstructures of both membrane sides. Based on the qualitative local analysis in **Tab. 5.16**, this secondary phase is strongly enriched in cobalt and depleted in strontium, which is similar to the precipitates found in the used membranes after long-term permeation measurements. Compared to the microstructures of the used membranes over the long-term permeation at 800 °C (see **Fig. 5.30**), less severe decay of the microstructures could be observed here along with fewer hexagonal phase formed at the feed side of the membrane. It confirms that the short temperature cycles above 850 °C could definitely retard the decay of membrane microstructures as well as hinder the formation of hexagonal phase along the boundaries. As a result, an improvement of the membrane permeability was achieved in the cyclic permeation test compared to the long-term permeation, considering the similar operation time for both measurements.

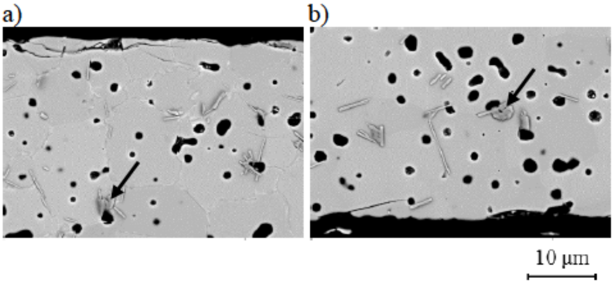

Fig. 5.42 SEM micrographs of a) the feed side and b) the sweep side of the 2.0 mm-thick BSCF5582 membrane after long-term cyclic permeation test in a temperature range of 700-900 °C under the air/He partial pressure gradient

Tab. 5.16 Quantitative local chemical compositions of the BSCF5582 membrane after cyclic oxygen permeation test in a temperature range of 700-900 °C in atomic percentage

Position	Ba / atom%	Sr / atom%	Co / atom%	Fe / atom%	O / atom%
Bulk	11.9	11.8	17.4	4.5	54.4
Precipitates	8.9	2.0	26.7	3.5	58.9

BSCF6482

As discussed above, the membrane permeability would be retrieved by enhancing the temperature higher than 850 °C. In order to confirm the influence of cyclic treatment on the membrane performance after long-term operation, a 2.0 mm-thick BSCF6482 membrane was used firstly for the long-term permeation measurement at 800 °C for 2000 h and then followed by cyclically changing the temperature within the range of 700-900 °C. The oxygen fluxes through this membrane as a function of time as well as operation temperature are displayed in **Fig. 5.43**.

Due to the technical problem occurring in the GC during the long-term permeation test at 800 C , the oxygen flux was recorded after ~1000 h operation. During this long-term period, it is clear that the membrane permeability declines progressively with time and the permeation flux is only 0.17 ml cm^{-2} min^{-1} over the entire 2000 h. As mentioned above, the decay of membrane permeability at 800 °C is more rapid in the thinner membrane and hence the oxygen flux obtained here through the 2.0 mm-thick membrane is comparable to the one with a permeate flux of 0.22 ml cm^{-2} min^{-1} through the 2.5 mm-thick membrane after 2000 h operation (see **Fig. 5.31**). By increasing the temperature up to 900 °C in the cyclic permeation test, the oxygen permeability of the membrane was greatly enhanced. The unsteady-state of the oxygen fluxes at the beginning of this temperature cycle lasts for ~20 h and a quite stable value of ~0.6 ml cm^{-2} min^{-1} was achieved afterwards, demonstrating the good permeation stability of the membrane at this temperature. However, when temperature drops back to 800 °C, a much faster decrease in the permeation rate could be observed, though the values are still larger than the one after long-term permeation. By further decreasing the temperature to 700 °C, same declining tendency of the oxygen permeability was found. Different from the permeation behaviour in BSCF5582 membrane (see **Fig. 5.41**), the oxygen permeability of this membrane at the second 800 °C temperature cycle is relatively stable. It seems that the decay of membrane permeability at this temperature is slowed down compared to the sharp decrease in the first temperature cycle. This stable oxygen flux was also found in the third cycle of 800 ℃ and the value is approaching the one achieved after long-term permeation measurement. This implies that the oxygen permeation through this membrane at 800 °C might reach an equilibrium flux after the long-term operation. When the temperature rises to 850 °C, an increment of oxygen flux could be observed, which mainly originates from the transition of formed hexagonal to cubic perovskites. Then an enhancement of membrane permeability was found by comparing the oxygen flux of the subsequent cyclic cycle at 800 ℃ to the previous one at the same temperature. This proves again that the oxygen permeation behaviour of membrane could be improved via a short-term cycle at temperatures higher than 850 °C. After the second temperature cycle at 900 °C, the oxygen fluxes through the membrane at 800 ℃ are almost the same to these in the first long-term cycle. Moreover, all the oxygen fluxes in the second long-term cycle appeared quite similar to those in the first cycle with the values in the same flux range for each temperature. However, it should be noted that an obvious increase in the permeation flux was obtained by increasing the temperature to 850 °C and the oxygen permeability of the membrane was improved in the following cycles, especially the one at 800 °C. In the third temperature cycle at 900 °C, the oxygen flux is much higher than the value obtained in the beginning of the cyclic permeation test. It confirms the membrane performance could be retrieved by the periodical variation of temperatures in this study. Thus, it could be concluded that oxygen permeability of this membrane decreases with time in the temperature range of 700-800 °C. While, a stable permeation flux was obtained at temperatures higher than 850 °C, which could be ascribed to the redox reaction of B-site cations as discussed in the BSCF5582 membrane. It is clear that the membrane performance is restored at high temperatures and after the cyclic permeation test, the oxygen flux through the membrane is significantly increased compared to the one measured at 800 °C after the long-term permeation for 2000 h. This could be caused by the reversible transition between the cubic and hexagonal polymorphs at intermediate temperatures.

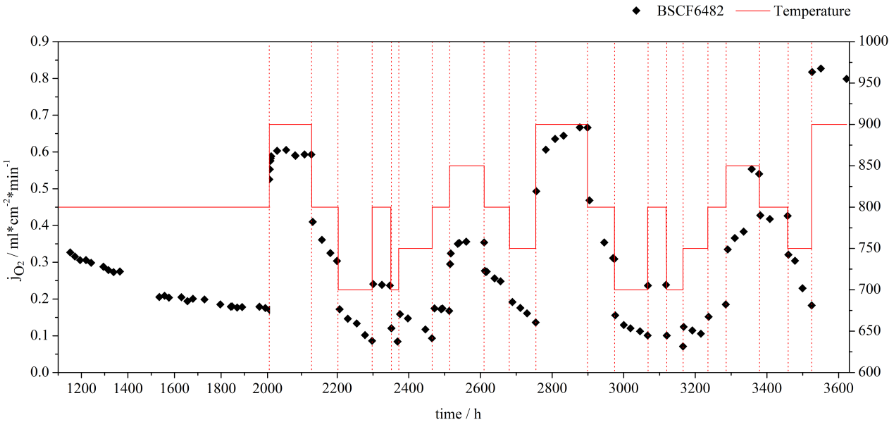

Fig. 5.43 Oxygen permeation fluxes through the 2.0-mm thick BSCF6482 membrane as a function of time at 800 °C for a period of 2000 h followed by periodical variation of temperatures in the range of 700-900 °C under the air/He partial pressure gradient

The microstructures of the used BSCF6482 membrane after the cyclic measurement are shown in **Fig. 5.44**. Various complex secondary phases were observed, especially the precipitates of barium carbonate and sulfate that distribute randomly in the bulk. The EDX results of the secondary phases in the used membrane are illustrated and discussed in **Appendix G**. According to the investigations on the structural stability of BSCF in CO_2-containing atmospheres [114, 147, 148], BSCF materials could easily react with CO_2 at intermediate temperatures and form barium carbonate on the sample surface. The formation of the carbonate particles might be caused by the short breakoff of the feed supply during the measurement that introduces a small amount of CO_2 in the ambient air to the membrane surface. Another possibility is that some impurities consisting of barium carbonate might be contained in the raw powder used for membrane production. In addition, the occurrence of barium sulfate may also originate from the impurities in the powder, since the raw material of $BaCO_3$ for BSCF powder production is generally produced from barium sulfate and some residuals might be left in the $BaCO_3$ product. The plate-like secondary phase in the microstructure was found to be enriched in cobalt and oxygen, but strongly depleted in strontium. This finding is consistent with the observations in the membranes after long-term permeation or the cyclic permeation test. It should be noticed here that no obvious formation of hexagonal phase was detected in this membrane in spite of the long-term operation at 800 °C. According to the decreasing tendency of the permeation curve at 800 °C observed in **Fig. 5.43**, there should be a phase transition occurring in the perovskite. To be more precisely, the formed hexagonal phase after the long-term operation transforms completely back into the cubic perovskite during the cyclic permeation measurement. Moreover, the absence of hexagonal phase in the microstructures may probably owing to the creation of the large amount of barium carbonate and sulfate in the bulk as well, leaving no sites for the nucleation of hexagonal phase in large scale. Therefore, it could be concluded that the oxygen permeability at intermediate temperatures is dominated by the amount of formed hexagonal phase rather than other secondary phases, as sufficiently large fractions of secondary phases could be observed at the feed side of the membrane but still a high permeation flux was achieved compared to that after the long-term operation.

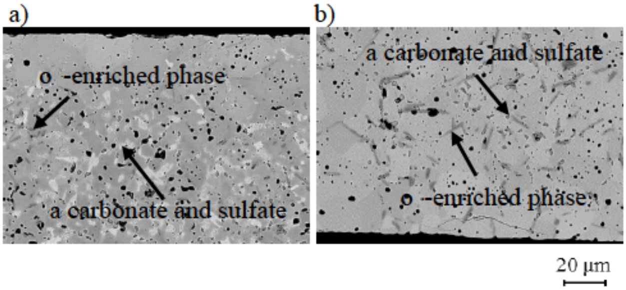

Fig. 5.44 SEM micrographs of a) the feed side and b) the sweep side of the 2.0 mm-thick BSCF6482 membrane after the long-term and cyclic permeation test in a temperature range of 700-900 °C under the air/He partial pressure gradient

5.6 Characterisation of thermochemical stability of BSCF materials

As can be seen from the oxygen permeation tests, the permeation stability decays with time at intermediate temperatures of 700-800 °C, which is commonly contributed to the formation of hexagonal phase in the perovskite lattice that hinders the oxygen transport. Increasing the temperature leads to the more stabilized permeation behaviour of BSCF membranes, though kinetic decomposition was still observed in the microstructures. Therefore, it is necessary to trace the phase decomposition or transition process in the perovskites at the investigated temperatures to further understand the kinetics for the time-dependent deterioration of membrane performance.

5.6.1 Phase decomposition of BSCF materials at 850 °C

The pellets of BSCF2828 and BSCF4628 were annealed in synthetic air at 850 ℃ for different periods: 100 h, 200 h and 500 h, respectively. The microstructural properties of the annealed samples were analysed by SEM across the cross sections and then the decomposition kinetics of the initial cubic perovskite as a function of time was recorded.

BSCF2828

The change of microstructures in BSCF2828 pellets as a function of annealing periods at 850 ℃ is illustrated in **Fig. 5.45**. A steady grain growth could be observed with the extension of annealing time and large grains with an average size of ~26.98 μm were obtained in the sample annealed for 500 h. A nearly single-phase microstructure was observed in the pellet after annealing for 100 h, except for few small particles formed at the triple-grain boundary sites. When the annealing time was extended to 200 h, more secondary phase was detected in the microstructure, which contains less iron and more strontium than the matrix. In addition, this secondary phase with similar elemental distributions was also present in the used BSCF4628 membrane after long-term permeation at 850 ℃ (see **Fig. 5.16**). In this membrane, the secondary phase was essentially restricted to the triple-grain boundaries sites that no particles passed through the bulk grains. However, considering the small sizes of these particles for quantitative analysis, the exact chemical composition of this secondary phase remains unclear. It should be emphasized that cracks could be observed in the region where this secondary phase was created. Obviously, the formation of this grain boundary phase leads to an accumulation of internal stresses in the perovskite and thus cracks are initiated along boundaries to release the stresses. After 500 h annealing, another plate-like secondary phase could be found also at the boundary sites in the microstructure. Different from the particles observed at the triple-grain boundary intersections, this plate-like phase is enriched in barium and cobalt together with a strong depletion in strontium (see **Fig. 5.46**). As discussed for the BSCF6482 membrane after long-term permeation at 800 ℃ , a monoclinic secondary phase were created as the intermediate state for the phase transition between cubic and hexagonal perovskites (see **Fig. 5.34**), which shows similar morphology and chemical distributions to the plate-like phase observed in the annealed pellet. Moreover, in combination with the linescan results of the BSCF6482 membrane tested at 850 ℃ for 2000 h in **Fig. 5.20**, the only difference in the chemical compositions between the plate-like phase in the pellet and the hexagonal phase observed in the membrane is the iron content. Here, a slight depletion of iron in the plate-like phase could be detected in the linescan results. Therefore, the formation of these plate-like precipitates could also be considered as an intermediate phase for the phase transition from cubic polymorph to hexagonal perovskite. In the meanwhile, considering the slightly depleted iron content in the intermediate phase, it could be argued that the phase decomposition process might be rate-determined by the diffusivity of iron at the boundary sites and the hexagonal phase would be formed after most of the iron is repelled from the nucleation sites.

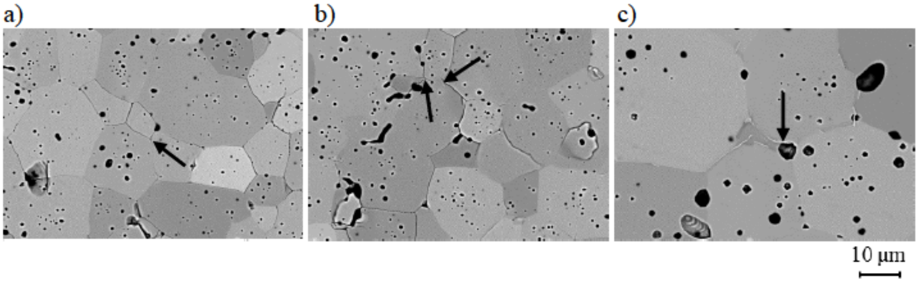

Fig. 5.45 SEM micrographs of the cross sections of the BSCF2828 pellets annealed in synthetic air atmosphere at 850 ℃ for a) 100 h; b) 200 h and c) 500 h

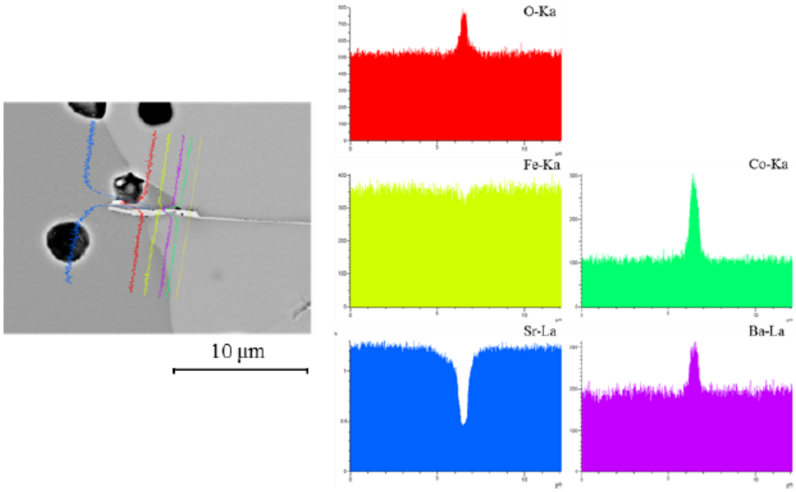

Fig. 5.46 The linescan and elemental distributions along the cross section of the BSCF2828 pellet after annealing treatment at 850 °C for 500 h in synthetic air

BSCF4628

The evolution of microstructures with annealing periods in the BSCF4628 pellets at 850 ℃ is displayed in **Fig. 5.47**. After annealing for 100 h, the pellet exhibits a pure microstructure with the single-phase morphology. By further extending the annealing time to 200 h, a dramatic grain growth of the bulk grains occurs. In addition, a secondary phase was formed at the grain boundaries sites, which induces microcracks in the vicinity as a consequence of the accumulated internal stresses. According to the local chemical compositions summarized in **Tab. 5.17**, this secondary phase contains more cobalt but less strontium than the bulk, which resembles the precipitates found in the BSCF6482 membrane after long-term permeation measurement at 850 ℃. It is worth noting that the chemical composition of the bulk also changes marginally with the annealing time, as the oxygen stoichiometry in the pellet annealed for 200 h is slightly lower than the one annealed for 100 h. The reason for the drop of oxygen concentration in the bulk could be ascribed to the formation of the oxygen-enriched secondary phase. For the pellet annealed for 500 h, some particles were also found at the boundaries sites in the microstructure. If comparing the chemical compositions of these secondary phases in the pellets annealed for 200 h and 500 h, it is interesting to find that the most significant difference between both precipitates is the iron concentration as well as the oxygen stoichiometry. As discussed above, a plate-like monoclinic phase found in the used membrane acts as the intermediate phase for the cubic-hexagonal phase transition, which shows an intermediate content of iron compared to the bulk and the formed hexagonal phase. In view of the similar elemental distributions of the precipitates in the annealed pellets, it could be addressed that these small particles formed in the perovskites during annealing at 850 ℃ might be related to the monoclinic phase found in the used membrane after long-term permeation measurement. Moreover, the gradual depletion of iron with annealing time in these secondary phases could also be regarded as a sign for the creation of the eventual hexagonal product by repelling the iron completely from the nucleation sites. In addition, the high oxygen stoichiometry in the precipitates in the pellet after 500 h annealing indicates that the elemental distribution of this secondary phase is progressively approaching the one required for a hexagonal phase with the extension of annealing time. Therefore, it could be presumed that the secondary phase observed in the annealed pellets is an intermediate step for the cubic-hexagonal phase transition.

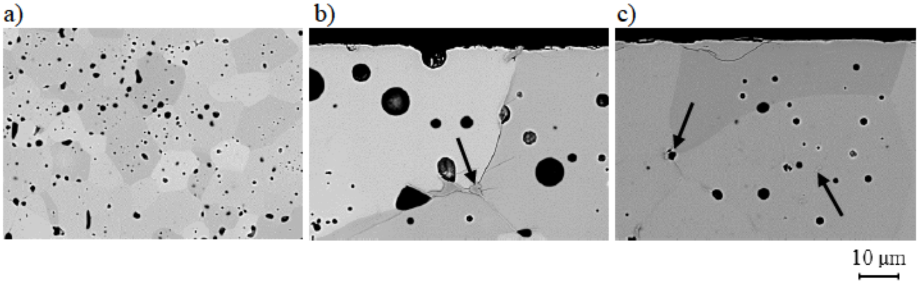

Fig. 5.47 SEM micrographs of the cross sections of the BSCF4628 pellets annealed in synthetic air atmosphere at 850 ℃ for a) 100 h; b) 200 h and c) 500 h

Tab. 5.17 Quantitative local chemical compositions of the BSCF4628 pellets annealed at 850 °C for 100 h, 200 h and 500 h in synthetic air in atomic percentage

Annealing period	Position	Ba / atom%	Sr / atom%	Co / atom%	Fe / atom%	O / atom%
100 h	Bulk	7.3	12.7	3.5	14.4	62.1
200 h	Bulk	7.9	13.2	3.6	15.3	60.0
	Precipitates	7.8	2.1	13.2	15.6	61.4
500 h	Bulk	8.1	13.2	3.6	15.3	59.8
	Precipitates	7.5	2.8	12.0	12.7	65.1

5.6.2 Phase decomposition of BSCF materials at 800 °C

The pellets of BSCF4682 and BSCF6482 were annealed in synthetic air at 800 ℃ for different periods: 200 h, 500 h and 1000 h respectively. The cross sections of the annealed samples were prepared for SEM analysis and the phase decomposition process in the BSCF perovskites as a function of time was recorded accordingly.

BSCF4682

The deterioration of microstructures in the BSCF4682 pellets annealed at 800 ℃ as a function of annealing time is illustrated in **Fig. 5.48**. The formation of hexagonal phase in the bulk was already detected in the pellet annealed for 200 h. An obvious depletion of iron along with an enrichment of cobalt was found in this hexagonal phase according to the quantitative EDX analysis in **Tab. 5.18**. It is apparent that the formed hexagonal phase was mainly restricted to the grain boundary sites in combination with some plate-like precipitates dispersing through the bulk grains. By extending the annealing time to 500 h, all the grain boundaries in the microstructure of the annealed pellet were occupied by hexagonal phase, which was characterized by a great depletion of iron content. Moreover, the chemical compositions of hexagonal phase in both samples annealed for 200 h and 500 h respectively vary markedly based on the EDX results, especially the concentrations of A-site cations (Ba^{2+} and Sr^{2+}). It seems that there is an elemental redistribution occurring in this hexagonal phase with the extension of annealing period, implying the chemical stoichiometry of this hexagonal phase boundary sites might be inhibited by the slow diffusivity of A-site cations, being consistent with the proposition in [98]. In contrast, the elemental distributions in the cubic perovskite matrix of both annealed pellets remain unchanged. For the pellet annealed for 1000 h, severe deterioration of the microstructure could be observed. It is clear that the hexagonal phase was also found running through the bulk grains as all the boundary sites were fully occupied. A continuous growth of hexagonal phase was observed with the extension of annealing time. Moreover, the cobalt concentration in the hexagonal phase increases patently along with the barium content compared to the distributions in the pellet annealed for 500 h. Similar to the findings in the BSCF4628 pellet annealed at 850 °C, a Co-enriched secondary phase could also be detected in the bulk of this material, which is considered as an intermediate state for phase decomposition. In view of the evolution of microstructures with annealing time, it could be concluded that the formation hexagonal phase goes via a nucleation and grain growth mechanism and this kinetics is probably controlled by the diffusivity of A-site cations.

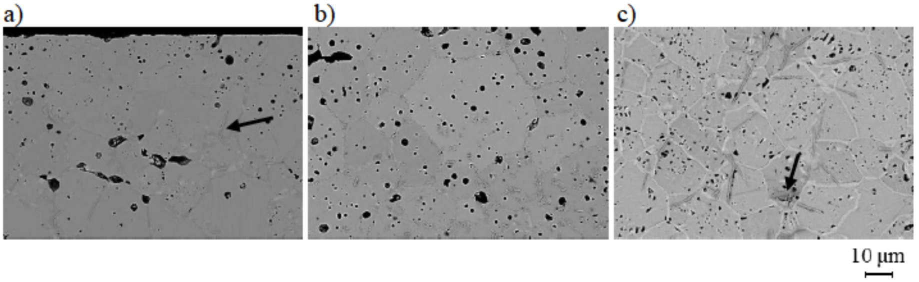

Fig. 5.48 SEM micrographs of the cross sections of the BSCF4682 pellets annealed in synthetic air atmosphere at 800 °C for a) 200 h; b) 500 h and c) 1000 h in synthetic air

Tab. 5.18 Quantitative local chemical compositions of the BSCF4682 pellets annealed at 800 °C for 200 h, 500 h and 1000 h in synthetic air in atomic percentage

Annealing period	Position	Ba / atom%	Sr / atom%	Co / atom%	Fe / atom%	O / atom%
200 h	Bulk	8.0	12.3	14.4	3.8	61.6
	Hexagonal phase	13.1	8.4	16.1	1.8	60.6
500 h	Bulk	7.6	12.4	14.0	4.0	62.0
	Hexagonal phase	7.0	13.3	15.8	0.9	63.0
1000 h	Bulk	9.5	14.3	16.8	4.4	55.0
	Hexagonal phase	10.8	13.6	18.2	0.8	56.5
	Precipitates	8.7	2.9	26.8	4.4	57.2

BSCF6482

The microstructural deterioration in the pellets annealed at 800 ℃ in synthetic air as a function of annealing time is illustrated in **Fig. 5.49**. Quite severe decay of the microstructure could already be observed in the pellet annealed for 200 h. Hexagonal phase was formed along the grain boundaries as well as within the bulk grains. This indicates that the deterioration rate in this material at 800 ℃ is extremely fast as the nucleation of hexagonal phase was initiated even in the bulk within 200 h. A large amount of plate-like secondary phase was found at the boundaries sites close to the hexagonal phase, which might be related to the Co-enriched phase as being observed in the annealed BSCF4682 pellets. By further extending the annealing period to 500 h, no obvious difference in the microstructures was detected compared to the one annealed for 200 h. It should be noticed that iron is repelled progressively from the hexagonal phase with the extension of annealing time. The most significant deterioration of microstructure was obtained in the pellet annealed for 1000 h. Nearly half of the matrix was decorated by the occurrence of hexagonal phase as well as the Co-enriched secondary phase. Compared to the pellet annealed for 500 h, much more hexagonal phase was found within the bulk grains along with a further depletion of iron from the boundary sites. Similar to the observations in the annealed BSCF4682 pellets, a redistribution of cations in the phases during annealing was detected according to the EDX analysis in **Tab. 5.19**. According to the observed microstructural properties, more hexagonal phase fraction is expected in the BSCF6482 pellets compared to BSCF4682 for the same annealing periods.

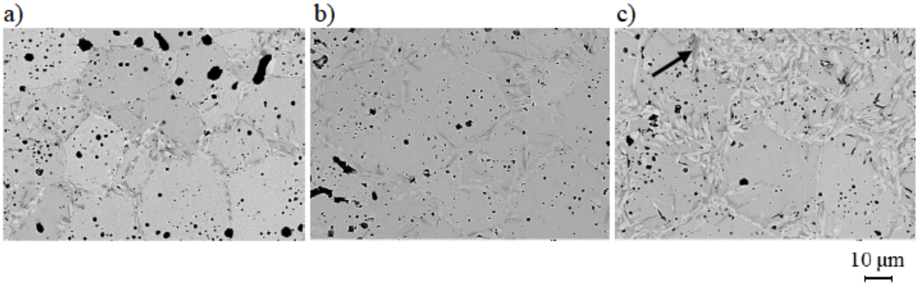

Fig. 5.49 SEM micrographs of the cross sections of the BSCF6482 pellets annealed in synthetic air atmosphere at 800 °C for a) 200 h; b) 500 h and c) 1000 h in synthetic air

Tab. 5.19 Quantitative local chemical compositions of the BSCF6482 pellets annealed at 800 °C for 200 h, 500 h and 1000 h in synthetic air in atomic percentage

Annealing period	Position	Ba / atom%	Sr / atom%	Co / atom%	Fe / atom%	O / atom%
200 h	Bulk	11.8	8.2	14.0	3.4	62.2
	Hexagonal phase	12.9	7.1	18.3	1.8	59.8
500 h	Bulk	11.8	8.4	14.5	3.9	61.4
	Hexagonal phase	12.7	7.9	15.7	1.1	62.7
1000 h	Bulk	14.2	9.8	17.2	4.4	54.3
	Hexagonal phase	15.3	8.9	18.7	0.5	56.5
	Precipitates	11.6	5.8	21.1	3.9	57.5

5.6.3 Growth kinetics of hexagonal phase

As discussed above, the hexagonal phase is formed in BSCF materials via the nucleation and grain growth mechanism at intermediate temperatures. In order to characterise this phase transition process, the formation kinetics from cubic to hexagonal perovskites is discussed in this chapter.

Fig. 5.50 illustrates the XRD patterns of the BSCF4682 pellets after long-term annealing at 800 ℃ . With the extension of annealing period, the reflection peaks for the hexagonal phase becomes more pronounced, implying a growth of its volume fraction in the perovskites. Similar observation was also found in the annealed BSCF6482 pellets as depicted in **Fig. 5.51**. Comparing the reflection signals from both samples, more hexagonal phase arises in the BSCF6482 pellets compared to BSCF4682 (see **Fig. 5.52**), which is in good agreement with the observations in the SEM micrographs. Similar findings were also reported in [98] that the phase fraction of hexagonal polymorph increases with barium content in BSCF materials after long-term annealing.

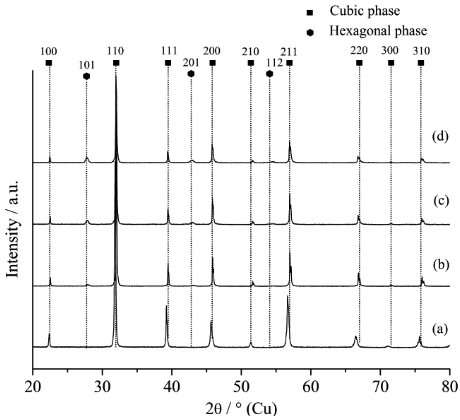

Fig. 5.50 XRD patterns of the BSCF4682 pellets a) as-sintered state (t = 0 h) and after annealing at 800 °C for b) 200 h; c) 500 h and d) 1000 h in synthetic air

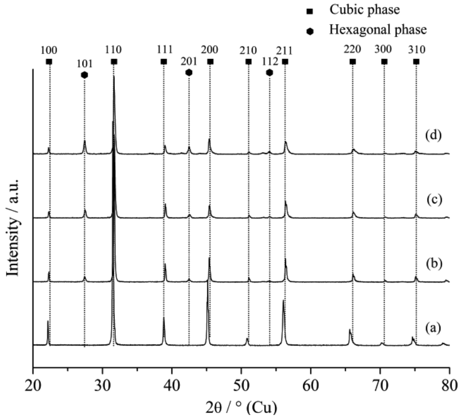

Fig. 5.51 XRD patterns of the BSCF6482 pellets a) as-sintered state (t = 0 h) and after annealing at 800 °C for b) 200 h; c) 500 h and d) 1000 h in synthetic air

As discussed on the used BSCF5582 membranes after long-term permeation at 800 ℃ , the kinetic process of hexagonal phase growth could be described according to the JMA model [138] by **Eq. 5.7**. Regarding the fitting parameters in **Tab. 5.20**, the approximate unity value of n in BSCF4682 could be ascribed to the grain boundary nucleation combined with a diffusion controlled growth. Moreover, according to the transformation kinetics summarized in [139], the unity value of n denotes that the nucleated particles grow via the thickening of needles and plates. It further confirms that the existence of the Co-enriched monoclinic phase, which exhibits a plate-like morphology in the annealed pellets, acts as an intermediate state for the cubic-hexagonal phase transition. The equilibrium volume fraction of the hexagonal phase reaches only ~45% in BSCF4682 at infinite annealing time as a result of the saturation of nucleation sites in the samples. The fitting parameters in this work is quite comparable to those obtained in the BSCF5582 ceramic membrane investigated by Mueller et al. [131]. As they proposed, the formation of the hexagonal phase is virtually not a phase transition but a decomposition process, in line with the equilibrium hexagonal fraction achieved in this material. However, for the BSCF6482 pellets, the n value is closer to 0.5 rather than unity. This means the transformation goes via nucleation and one-dimensional growth with a fast formation of the nuclei, while the growth kinetics is controlled by the slow transport of the involved ions [149]. Thus, the time required for the nucleation is much shorter than that for the growth of the new phase. In other words, the nucleation process is already accomplished before the start of the phase growth as all the nucleation sites are occupied with nuclei. It is interesting to note that the equilibrium volume fraction of hexagonal phase in BSCF6482 reaches 100%, indicating the initial cubic perovskite would transform completely into the hexagonal perovskite with the lapse of annealing time. As expected, the rate constant for the BSCF6482 pellets is three times higher than for BSCF4682. Since the hexagonal product is commonly enriched in barium but depleted in strontium, it is reasonable to argue that the decomposition rate from cubic to hexagonal phase is dependent on the Ba/Sr ratio, i.e. higher barium concentration in BSCF accelerates the formation of hexagonal phase. In order to understand the reason for the influence of A-site cations concentration on phase decomposition kinetics, the structural relationship between the cubic and hexagonal perovskites should be taken into account. In principle, the hexagonal phase possesses a structure with chains of face-sharing BO_6 octahedra, and when both A- and B-site cations matches the sizes to form cubic perovskite, an array of corner-shared BO_6 is present [98]. Based on the investigations by Arnold et al. [96, 150] and Negas et al. [151], the phase transition between cubic and hexagonal perovskites occurs via a shear of the AO_3-hexagonal layers. Increasing the size of A-site cations by substituting larger barium cations for strontium favours face-sharing octahedral and thus prompts the formation of hexagonal perovskite [152].

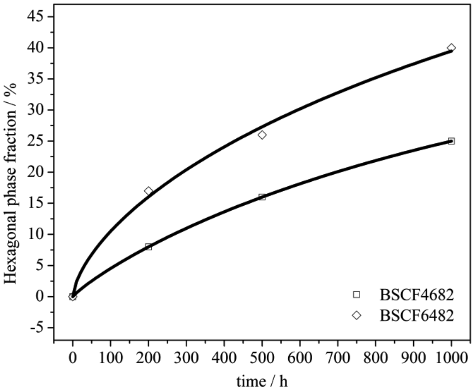

Fig. 5.52 The growth of hexagonal phase in the BSCF pellets annealed at 800 °C

Tab. 5.20 Fitting parameters for the growth of hexagonal phase in the annealed BSCF pellets according to $\alpha_{hex}(t)\quad \alpha_{hex}(t\quad)\left(\ -e^{-kt^{n}}\right)$

Materials	Fitting parameters		
	$\alpha_{hex}(t\quad)$ / %	k / h^{-n}	n / -
BSCF4682	45.33	0.0018	0.88
BSCF6482	100.00	0.0054	0.66

In addition, a significant depletion of iron was generally observed at the boundary sites where the hexagonal phase arrayed (see **Fig. 5.53**). After annealing the pellets for 1000 h, most of the iron was repelled from the grain boundaries coupled with an increment of iron concentration in the bulk to maintain the mass balance. As mentioned above, the driving force for the phase transition to hexagonal phase is related to the change in the preferred spin states of Co ions as well as the decrease in the radii of B-site cations due to oxidation [96, 134]. The reason for the preference of cobalt ions in hexagonal structure could be explained on the basis of a simple model in [96]. It is assumed that both B-site cations possess an initial oxidation state of 3+, though their valences are actually variants changing with the temperature [153]. From the structure point of view, the fundamental discrepancy between the cubic and hexagonal perovskites is the connection of the BO_6 octahedra. In the cubic structure, the B-O bonding in the corner-shared octahedra is ~0.195 nm, whereas the face-sharing octahedra in hexagonal structure have a B-O bonding distance of ~0.184 nm [96]. Considering the large differences in the ionic radii of cobalt and iron (for Fe^{3+}(HS) = 0.645 Å and for Co^{3+}(LS) = 0.545 Å [68]), it is evident that cobalt is more prone to form the hexagonal structure.

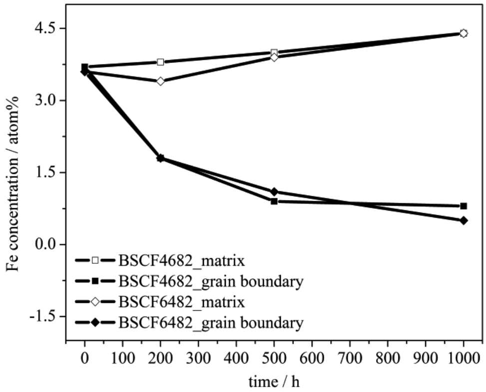

Fig. 5.53 The variation of iron concentration in the bulk as well as at the grain boundary sites in the annealed BSCF4682 and BSCF6482 pellets at 800 °C as a function of annealing time

6 Conclusions

In this work, the thermochemical properties as well as the long-term permeability and stability of membrane materials were systematically investigated under oxyfuel process conditions. First of all, suitable membrane materials were selected for this study. Based on the published literatures, the solid-state reaction method was chosen which is suitable for the synthesis of perovskite oxides. The properties of synthetized powder products were characterized in terms of phase composition, chemical composition and particle size distribution.

The structural stability of BSCF perovskite materials was predicted according to Goldschmidt tolerance factor as a function of chemical composition and oxygen nonstoichiometry. It shows that not all the BSCF materials investigated in this work can principally form an ideal cubic perovskite. The reason for this deviation is mainly attributed to the large ionic radii of A-site cations, which induce lattice distortion, especially the tilting of the corner-shared BO_6 octahedra as the basic unit for the formation of cubic perovskite. For the same reason, doping cations with a smaller size at B site in the ABO_3 perovskite lattice could also result in an increment of tolerance factor. Moreover, higher tolerance factor was obtained in the materials with a lower oxygen nonstoichiometry. As some BSCF materials were detected to exhibit a cubic perovskite structure, the tolerance factor should be considered only as a prediction for the formation of cubic perovskite.

Considering the sintering process has a direct influence on the porosity density of the samples, the sintering behaviour of each membrane material was recorded in order to determine the proper sintering parameters for sample production. All the BSCF samples show ~20% shrinkage upon heating to temperatures higher than 1150 °C, along with two minimal peaks present in the shrinkage rate curves. From the SEM micrographs, it is clear that sintering temperature plays a more significant role in the improvement of sample density compared to dwelling time. Here, all the sintered samples used for investigation show a relative density higher than 90%.

Oxygen transport through the membrane is realized by the existence of oxygen vacancies in the perovskite. Thus, it is necessary to trace the variation of oxygen stoichiometry in BSCF materials at intermediate temperatures. The oxygen deficiency increases fast when temperature exceeds ~500-550 °C. It seems that the chemical composition of BSCF materials has an effect on the change of oxygen stoichiometry. The substitution of iron for cobalt at the B site of the perovskites was found to prompt oxygen release and hence the formation of oxygen vacancies. In contrast, the substoichiometry at the A site has little influence on the variation of oxygen nonstoichiometry.

The thermochemical expansion behaviours of BSCF materials were also studied systematically. Nonlinear expansion curves were obtained in all the samples due to oxygen desorption upon heating. It was found that materials with higher strontium or iron content show a larger chemical expansion, which is consistent with the observations in the TGA measurements for the change of oxygen nonstoichiometry. The results imply that the increase of Co-doping in BSCF might decrease the critical temperature for the reduction of B-site cations from high valences to the lower ones.

The long-term permeation stability of BSCF membranes was investigated at 850 °C for 2000 h under the air/He pressure gradient. A steady increase of oxygen flux was observed in the BSCF4628 membrane over the entire 2000 h. This flux increment may be attributed to the improvement of surface roughness as well as the enlarged grain size of the used membrane. On the contrary, a slow and exponential decay of oxygen permeation rate was observed in the BSCF6482 membrane under the same condition. About 4% hexagonal phase was detected at the grain boundary sites in the used membrane, which is suggested to be the major reason for the decline of membrane permeability.

By descending the operation temperature to 800 °C, all the BSCF membranes investigated in this study show an exponential deterioration in the oxygen permeability during the long-term permeation measurement. The formation of hexagonal phase due to phase decomposition was already detected after 200 h operation at this temperature. The growth of hexagonal nuclei is a function of operation time according to the JMA model, resulting in the progressive decrease of the permeation flux. After the saturation of nucleation sites at grain boundaries, hexagonal phase was also observed within the bulk grains. Despite of the formation of hexagonal phase, a Co-rich monoclinic phase with plate-like morphology was found in the microstructures of the used membranes, which is considered as an intermediate state for the phase transition between cubic and hexagonal perovskites. In addition, severe decay of the microstructures was observed at the feed side compared to the permeate side of the membranes.

According to the measured permeation curves, the oxygen permeation stability of BSCF membranes was found to be dependent on chemical composition, temperature as well as membrane thickness. The oxygen flux through the membranes was greatly improved by increasing the cobalt concentration in the materials. However, higher cobalt concentration in BSCF could accelerate the cubic-hexagonal phase transition and leads to the decline of permeation stability at intermediate temperatures. It is proven that the substitution of strontium for barium in the BSCF materials could enhance the permeation stability of the membrane while maintain its oxygen flux. Comparing the permeation behaviours of membranes at 800 °C and 850 °C, a great improvement of membrane performance, especially the oxygen permeation stability, was achieved at 850 ℃ . It seems that the formation of hexagonal phase is supressed at the higher temperature in accordance with the stabilized oxygen permeation flux through the membrane. Moreover, the permeation stability is also influenced by membrane thickness, as faster deterioration was found in the 1.0 mm-thick membrane compared with the 2.5 mm-thick one over the long-term operation at 800 °C.

Cyclic permeation tests were performed in the temperature range of 700-900 °C to clarify the impact of temperature as well as periodical operation on the membrane permeability. A decay of oxygen flux was observed at temperatures below 850 °C. In the meanwhile, membrane performance was definitely improved by the cyclical operation at temperatures higher than 850 °C. This indicates that the phase transition occurring at intermediate temperatures is reversible and cubic perovskite is favoured in the high temperature range.

The formation kinetics of hexagonal phase in BSCF materials was rationalized on the basis of long-term annealing tests at 800 °C and 850 °C. The phase transition process in BSCF materials may follow this sequence: cubic perovskite → plate-like monoclinic phase → hexagonal phase. The change of ionic radii and spin state of cationic cobalt due to oxidation is regarded as the driving force for the creation of hexagonal phase. Considering the strongly oxidizing local conditions for cobalt ions, the nucleation of hexagonal phase occurs preferably at the grain boundaries. The growth kinetics of hexagonal phase could be well fitted to the JMA model. The phase transition via the nucleation and grain growth mechanism is probably controlled by the diffusivity of A-site cations.

References

[1] International Energy Agency, World Energy Outlook 2011, Executive summary, OECD/IEA, Paris, 2011.

[2] http://co2now.org/Current-CO2/CO2-Now/global-carbon-emissions.html.

[3] http://europa.eu/legislation_summaries/energy/european_energy_policy/l27068_en.htm.

[4] B. Metz, Intergovernmental panel on climate change. Working group III, IPCC special report on carbon dioxide capture and storage, Cambridge University Press for the Intergovernmental Panel on Climate Change, 2005.

[5] J. Gibbins, H. Chalmers, Carbon capture and storage, Energy Policy, 36 (2008) 4317-4322.

[6] CO_2 capture technologies, Technology options for CO_2 capture, Global CCS institute, 2012.

[7] C. Descamps, C. Bouallou, M. Kanniche, Efficiency of an Integrated Gasification Combined Cycle (IGCC) power plant including CO_2 removal, Energy, 33 (2008) 874-881.

[8] M. Amelio, P. Morrone, F. Gallucci, A. Basile, Integrated gasification gas combined cycle plant with membrane reactors: Technological and economical analysis, Energy Conversion and Management, 48 (2007) 2680-2693.

[9] H. Matsuyama, M. Teramoto, H. Sakakura, K. Iwai, Facilitated transport of CO_2 through various ion exchange membranes prepared by plasma graft polymerization, Journal of Membrane Science, 117 (1996) 251-260.

[10] H. Chen, A.S. Kovvali, S. Majumdar, K.K. Sirkar, Selective CO_2 separation from CO_2-N_2 mixtures by immobilized carbonate-glycerol membranes, Industrial & Engineering Chemistry Research, 38 (1999) 3489-3498.

[11] A.S. Kovvali, K.K. Sirkar, Dendrimer liquid membranes: CO_2 separation from gas mixtures, Industrial & Engineering Chemistry Research, 40 (2001) 2502-2511.

[12] Vattenfall AG: http://www.vattenfall.com/en/ccs/illustrations.htm.

[13] H. Herzog, J. Meldon, A. Hatton, Advanced post-combustion CO_2 capture, MIT Energy Initiative, 2009.

[14] E. Favre, Membrane processes and postcombustion carbon dioxide capture: Challenges and prospects, Chemical Engineering Journal, 171 (2011) 782-793.

[15] D. Adams, Flue gas treatment for CO_2 capture, IEA Clean Coal Centre, 2010.

[16] T.F. Wall, Combustion processes for carbon capture, Proceedings of the Combustion Institute, 31 (2007) 31-47.

[17] P.H.M. Feron, A.E. Jansen, R. Klaassen, Membrane technology in carbon dioxide removal, Energy Conversion and Management, 33 (1992) 421-428.

[18] E. Drioli, M. Romano, Progress and new perspectives on integrated membrane operations for sustainable industrial growth, Industrial Engineering Chemistry Research, 40 (2001) 1277-1300.

[19] C.E. Powell, G.G. Qiao, Polymeric CO_2/N_2 gas separation membranes for the capture of carbon dioxide from power plant flue gases, Journal of Membrane Science, 279 (2006) 1-49.

[20] R. Baker, Future directions of membrane gas-separation technology, in: Membrane Technology, John Wiley & Sons, 2001, pp. 5-10.

[21] H. Lin, B.D. Freeman, Gas solubility, diffusivity and permeability in poly

(ethylene oxide), Journal of Membrane Science, 239 (2004) 105-117.

[22] W.J. Ward, W.L. Robb, Carbon dioxide—Oxygen separation: Facilitated transport of carbon dioxide across a liquid film, Science, 156 (1967) 1481-1484.

[23] E. Tzimas, A. Mercier, C.C. Cormos, S.D. Peteves, Trade-off in emissions of acid gas pollutants and of carbon dioxide in fossil fuel power plants with carbon capture, Energy Policy, 35 (2007) 3991-3998.

[24] T. Wall, R. Gupta, B. Buhre, S. Khare, Oxy-fuel (O_2/CO_2, O_2/RFG) technology for sequestration-ready CO_2 and emission compliance, The clearwater coal conference: The 30th international technical conference on coal utilization and fuel systems, coal technology: Yesterday-today-tomorrow, Clearwater USA, 2005.

[25] M. Kanniche, R. Gros-Bonnivard, P. Jaud, J. Valle-Marcos, J.-M. Amann, C. Bouallou, Pre-combustion, post-combustion and oxy-combustion in thermal power plant for CO_2 capture, Applied Thermal Engineering, 30 (2010) 53-62.

[26] A. Kather, S. Kownatzki, Assessment of the different parameters affecting the CO_2 purity from coal fired oxyfuel process, International Journal of Greenhouse Gas Control, 5 (2011) 204-209.

[27] M. Czyperek, P. Zapp, H.J.M. Bouwmeester, M. Modigell, K. Ebert, I. Voigt, W.A. Meulenberg, L. Singheiser, D. Stöver, Gas separation membranes for zero-emission fossil power plants: MEM-BRAIN, Journal of Membrane Science, 359 (2010) 149-159.

[28] P.N. Dyer, R.E. Richards, S.L. Russek, D.M. Taylor, Ion transport membrane technology for oxygen separation and syngas production, Solid State Ionics, 134 (2000) 21-33.

[29] M. Freemantle, Membranes for gas separations, Chemical & Engineering News, 83 (2005) 9.

[30] S. Gopalan, Using ceramic mixed ionic and electronic conductors for gas separation, Journal of Minerals, Metals and Materials Society, 54 (2002) 26-29.

[31] A.J. Jacobson, S. Kim, A. Medina, Y.L. Yang, B. Abeles, Dense oxide membranes for oxygen separation and methane conversion, Materials Research Society Symposium-Proceedings, 497 (1998) 29-34.

[32] Z. Chen, R. Ran, W. Zhou, Z. Shao, S. Liu, Assessment of $Ba_{0.5}Sr_{0.5}Co_{1-y}Fe_yO_{3-\delta}$ (y = 0.0-1.0) for prospective application as cathode for IT-SOFCs or oxygen permeating membrane, Electrochimica Acta, 52 (2007) 7343-7351.

[33] S. Stølen, E. Bakken, C.E. Mohn, Oxygen-deficient perovskites: Linking structure, energetics and ion transport, Physical Chemistry Chemical Physics, 8 (2006) 429-447.

[34] F.S. Galasso, Perovskites and high Tc superconductors, Gordon and Breach, New York, 1990.

[35] V.M. Goldschmidt, Die Gesetze der Krystallochemie, Dybwad, 1926.

[36] J. Martynczuk, Mixed conducting perovskites and their solid state chemistry, Südwestdt. Verl. für Hochschulschriften, Saarbücken, 2008.

[37] N. Ramadass, ABO_3-type oxides—Their structure and properties—A bird's eye view, Materials Science and Engineering, 36 (1978) 231-239.

[38] C. Ye, J. Yang, L. Yao, N. Chen, Regularities of formation and lattice distortion of perovskite-type compounds, Chinese Science Bulletin, 47 (2002) 458-460.

[39] C. Li, K.C.K. Soh, P. Wu, Formability of ABO_3 perovskites, Journal of Alloys and Compounds, 372 (2004) 40-48.

[40] Z. Wang, Functional and smart materials, in: Wiley Encyclopedia of Electrical and Electronics Engineering, John Wiley & Sons, Inc., 1999.

[41] R.C. Buchanan, T. Park, Materials crystal chemistry, Taylor & Francis, 1997.

[42] G.S. Rohrer, Structure and bonding in crystalline materials, Cambridge University Press, 2001.

[43] P. Kofstad, Nonstoichiometry, diffusion, and electrical conductivity in binary metal oxides, John Wiley & Sons, Inc., 1972.

[44] W.D. Kingery, H.K. Bowen, D.R. Uhlmann, Introduction to ceramics, Wiley-Interscience, 1976.

[45] H.J.M. Bouwmeester, A.J. Burggraaf, Chapter 10—Dense ceramic membranes for oxygen separation, Membrane Science and Technology, 4 (1996) 435-528.

[46] S.P.S. Badwal, F.T. Ciacchi, Ceramic membrane technologies for oxygen separation, Advanced Materials, 13 (2001) 993-996.

[47] J. Sunarso, S. Baumann, J.M. Serra, W.A. Meulenberg, S. Liu, Y.S. Lin, J.C. Diniz da Costa, Mixed ionic-electronic conducting (MIEC) ceramic-based membranes for oxygen separation, Journal of Membrane Science, 320 (2008) 13-41.

[48] E. Bucher, A. Egger, P. Ried, W. Sitte, P. Holtappels, Oxygen nonstoichiometry and exchange kinetics of $Ba_{0.5}Sr_{0.5}Co_{0.8}Fe_{0.2}O_{3-\delta}$, Solid State Ionics, 179 (2008) 1032-1035.

[49] N. Yamazoe, Y. Teraoka, T. Seiyama, TPD and XPS study of thermal behavior of adsorbed oxygen on $La_{1-x}Sr_xCoO_3$, Chemistry Letters, (1981) 1767-1770.

[50] H.U. Anderson, Review of p-type doped perovskite materials for SOFC and other applications, Solid State Ionics, 52 (1992) 33-41.

[51] J. Mizusaki, Nonstoichiometry, diffusion, and electrical properties of perovskite-type oxide electrode materials, Solid State Ionics, 52 (1992) 79-91.

[52] Y. Teraoka, H.M. Zhang, K. Okamoto, N. Yamazoe, Mixed ionic-electronic conductivity of $La_{-x}Sr_xCo_{-y}Fe_yO_{-\delta}$ perovskite-type oxides, Materials Research Bulletin, 23 (1988) 51-58.

[53] P. Zeng, Z. Chen, W. Zhou, H. Gu, Z. Shao, S. Liu, Re-evaluation of $Ba_{0.5}Sr_{0.5}Co_{0.8}Fe_{0.2}O_{-\delta}$ perovskite as oxygen semi-permeable membrane, Journal of Membrane Science, 291 (2007) 148-156.

[54] H. Ullmann, N. Trofimenko, F. Tietz, D. Stöver, A. Ahmad-Khanlou, Correlation between thermal expansion and oxide ion transport in mixed conducting perovskite-type oxides for SOFC cathodes, Solid State Ionics, 138 (2000) 79-90.

[55] Z. Shao, W. Yang, Y. Cong, H. Dong, J. Tong, G. Xiong, Investigation of the permeation behavior and stability of a $Ba_{0.5}Sr_{0.5}Co_{0.8}Fe_{0.2}O_{3-\delta}$ oxygen membrane, Journal of Membrane Science, 172 (2000) 177-188.

[56] R. Merkle, Y.A. Mastrikov, E.A. Kotomin, M.M. Kuklja, J. Maier, First principles calculations of oxygen vacancy formation and migration in $Ba_{-x}Sr_xCo_{1-y}Fe_yO_{-\delta}$ perovskites, Journal of The Electrochemical Society, 159 (2012) 219-226.

[57] C.A.J. Fisher, M. Yoshiya, Y. Iwamoto, J. Ishii, M. Asanuma, K. Yabuta, Oxide ion diffusion in perovskite-structured $Ba_{1-x}Sr_xCo_{1-y}Fe_yO_{2.5}$: A molecular dynamics study, Solid State Ionics, 177 (2007) 3425-3431.

[58] R. Kriegel, R. Kircheisen, J. Töpfer, Oxygen stoichiometry and expansion behavior of $Ba_{0.5}Sr_{0.5}Co_{0.8}Fe_{0.2}O_{3-\delta}$, Solid State Ionics, 181 (2010) 64-70.

[59] H. Wang, Y. Cong, W. Yang, Oxygen permeation study in a tubular $Ba_{0.5}Sr_{0.5}Co_{0.8}Fe_{0.2}O_{3-\delta}$ oxygen permeable membrane, Journal of Membrane Science, 210 (2002) 259-271.

[60] J.F. Vente, S. McIntosh, W.G. Haije, H.J.M. Bouwmeester, Properties and

performance of $Ba_xSr_{1-x}Co_{0.8}Fe_{0.2}O_{-\delta}$ materials for oxygen transport membranes, Journal of Solid State Electrochemistry, 10 (2006) 581-588.

[61] E. Girdauskaite, H. Ullmann, M. Daroukh, V. Vashook, M. Bülow, U. Guth, Oxygen stoichiometry, unit cell volume, and thermodynamic quantities of perovskite-type oxides, Journal of Solid State Electrochemistry, 11 (2007) 469-477.

[62] S. McIntosh, J.F. Vente, W.G. Haije, D.H.A. Blank, H.J.M. Bouwmeester, Structure and oxygen stoichiometry of $SrCo_{0.8}Fe_{0.2}O_{-\delta}$ and $Ba_{0.5}Sr_{0.5}Co_{0.8}Fe_{0.2}O_{-\delta}$, Solid State Ionics, 177 (2006) 1737-1742.

[63] H. Wang, C. Tablet, A. Feldhoff, J. Caro, Investigation of phase structure, sintering, and permeability of perovskite-type $Ba_{0.5}Sr_{0.5}Co_{0.8}Fe_{0.2}O_{-\delta}$ membranes, Journal of Membrane Science, 262 (2005) 20-26.

[64] S. McIntosh, J.F. Vente, W.G. Haije, D.H.A. Blank, H.J.M. Bouwmeester, Oxygen stoichiometry and chemical expansion of $Ba_{0.5}Sr_{0.5}Co_{0.8}Fe_{0.2}O_{3-\delta}$ measured by in situ neutron diffraction, Chemistry of Materials, 18 (2006) 2187-2193.

[65] A. Atkinson, T.M.G.M. Ramos, Chemically-induced stresses in ceramic oxygen ion-conducting membranes, Solid State Ionics, 129 (2000) 259-269.

[66] X. Chen, J. Yu, S.B. Adler, Thermal and chemical expansion of Sr-doped lanthanum cobalt oxide ($La_{1-x}Sr_xCoO_{3-\delta}$), Chemistry of Materials, 17 (2005) 4537-4546.

[67] M. Al Daroukh, V.V. Vashook, H. Ullmann, F. Tietz, I. Arual Raj, Oxides of the AMO_3 and A_2MO_4-type: Structural stability, electrical conductivity and thermal expansion, Solid State Ionics, 158 (2003) 141-150.

[68] R. Shannon, Revised effective ionic radii and systematic studies of interatomic distances in halides and chalcogenides, Acta Crystallographica Section A, 32 (1976) 751-767.

[69] J.M. Paulsen, Thermodynamics, oxygen stoichiometric effects and transport properties of ceramic materials in the system Sr-Ce-M-O (M = Co, Fe), Dissertation, Dresden: Technische Univ. Dresden, 1997.

[70] H. Lu, Y. Cong, W.S. Yang, Oxygen permeability and stability of $Ba_{0.5}Sr_{0.5}Co_{0.8}Fe_{0.2}O_{-\delta}$ as an oxygen-permeable membrane at high pressures, Solid State Ionics, 177 (2006) 595-600.

[71] X. Zhu, Y. Cong, W. Yang, Oxygen permeability and structural stability of $BaCe_{0.15}Fe_{0.85}O_{-\delta}$ membranes, Journal of Membrane Science, 283 (2006) 38-44.

[72] B. Wei, Z. Lü, X. Huang, J. Miao, X. Sha, X. Xin, W. Su, Crystal structure, thermal expansion and electrical conductivity of perovskite oxides $Ba_xSr_{-x}Co_{0.8}Fe_{0.2}O_{-\delta}$ $\le x \le$, ournal of the European eramic Society, 26 (2006) 2827-2832.

[73] J. Pena-Martínez, D. Marrero- ópez, J.C. Ruiz-Morales, P. Nunez, C. Sanchez-Bautista, A.J. Dos Santos-Garcia, J. Canales-Vazquez, On $Ba_{0.5}Sr_{0.5}Co_{1-y}Fe_yO_{3-\delta}$ ($y = 0.1$-0.9) oxides as cathode materials for $La_{0.9}Sr_{0.1}Ga_{0.8}Mg_{0.2}O_{2.85}$ based IT-SOFCs, International Journal of Hydrogen Energy, 34 (2009) 9486-9495.

[74] J. Ovenstone, Jae-II. Jung, J.S. White, D.D. Edwards, S.T. Misture, Phase stability of BSCF in low oxygen partial pressures, Journal of Solid State Chemistry, 181 (2008) 576-586.

[75] Y. Teraoka, M. Yoshimatsu, N. Yamazoe, T. Seiyama, Oxygen sorptive properties and defect structure of perovskite-type oxides, Chemistry Letters, 13 (1984) 893-896.

[76] H. Wang, C. Tablet, W. Yang, J. Caro, In situ high temperature X-ray diffraction studies of mixed ionic and electronic conducting perovskite-type membranes, Materials Letters, 59 (2005) 3750-3755.

[77] T.H. Lee, Y.L. Yang, A.J. Jacobson, B. Abeles, M. Zhou, Oxygen permeation in dense $SrCo_{0.8}Fe_{0.2}O_{-\delta}$ membranes: Surface exchange kinetics versus bulk diffusion, Solid State Ionics, 100 (1997) 77-85.

[78] J. Sunarso, S. Liu, Y.S. Lin, J.C. Diniz da Costa, Oxygen permeation performance of $BaBiO_{-\delta}$ ceramic membranes, Journal of Membrane Science, 344 (2009) 281-287.

[79] Y.S. Lin, W. Wang, J. Han, Oxygen permeation through thin mixed-conducting solid oxide membranes, AIChE Journal, 40 (1994) 786-798.

[80] J.E. ten Elshof, H.J.M. Bouwmeester, H. Verweij, Oxygen transport through $La_{-x}Sr_xFeO_{-\delta}$ membranes II. Permeation in air/CO, CO_2 gradients, Solid State Ionics, 89 (1996) 81-92.

[81] F.A. Kröger, H.J. Vink, Relations between the concentrations of imperfections in crystalline solids, in: Solid State Physics, Academic Press, 1956, pp. 307-435.

[82] Z. Shao, G. Xiong, H. Dong, W. Yang, L. Lin, Synthesis, oxygen permeation study and membrane performance of a $Ba_{0.5}Sr_{0.5}Co_{0.8}Fe_{0.2}O_{-\delta}$ oxygen-permeable dense ceramic reactor for partial oxidation of methane to syngas, Separation and Purification Technology, 25 (2001) 97-116.

[83] M. Mosleh, M. Søgaard, P.V. Hendriksen, Kinetics and mechanisms of oxygen surface exchange on $La_{0.6}Sr_{0.4}FeO_{-\delta}$ thin films, Journal of The Electrochemical Society, 156 (2009) 441-457.

[84] H.J.M. Bouwmeester, H. Kruidhof, A.J. Burggraaf, Importance of the surface exchange kinetics as rate limiting step in oxygen permeation through mixed-conducting oxides, Solid State Ionics, 72 (1994) 185-194.

[85] Bart A. van Hassel, Oxygen transfer across composite oxygen transport membranes, Solid State Ionics, 174 (2004) 253-260.

[86] K. Tabata, I. Matsumoto, S. Kohiki, Surface characterization and catalytic properties of $La_{1-x}Sr_xCoO_3$, Journal of Materials Science, 22 (1987) 1882-1886.

[87] M.-L. Fontaine, T. Norby, Y. Larring, T. Grande, R. Bredesen, Oxygen and hydrogen separation membranes based on dense ceramic conductors, Membrane Science and Technology, 13 (2008) 401-458.

[88] Y. Li, E.R. Maxey, J.W. Richardson, Structural behavior of oxygen permeable $SrFe_{0.2}Co_{0.8}O_x$ ceramic membranes with and without pO_2 gradients, Journal of the American Ceramic Society, 88 (2005) 1244-1252.

[89] Z. Shao, G. Xiong, J. Tong, H. Dong, W. Yang, Ba effect in doped $Sr(Co_{0.8}Fe_{0.2})O_{3-\delta}$ on the phase structure and oxygen permeation properties of the dense ceramic membranes, Separation and Purification Technology, 25 (2001) 419-429.

[90] H. Kruidhof, H.J.M. Bouwmeester, R.H.E. v. Doorn, A.J. Burggraaf, Influence of order-disorder transitions on oxygen permeability through selected nonstoichiometric perovskite-type oxides, Solid State Ionics, 63-65 (1993) 816-822.

[91] A.C. Van Veen, M. Rebeilleau, D. Farrusseng, C. Mirodatos, Studies on the performance stability of mixed conducting BSCFO membranes in medium temperature oxygen permeation, Chemical Communications, 9 (2003) 32-33.

[92] H.L. Lein, K. Wiik, T. Grande, Kinetic demixing and decomposition of oxygen permeable membranes, Solid State Ionics, 177 (2006) 1587-1590.

[93] L. Ge, W. Zhou, R. Ran, S. Liu, Z. Shao, W. Jin, N. Xu, Properties and

performance of A-site deficient $(Ba_{0.5}Sr_{0.5})_{-x}Co_{0.8}Fe_{0.2}O_{-\delta}$ for oxygen permeating membrane, Journal of Membrane Science, 306 (2007) 318-328.

[94] H. Schmalzried, Oxidation of metals, in: Chemical Kinetics of Solids, Wiley-VCH Verlag GmbH, 2007, pp. 165-182.

[95] K. Efimov, Q. Xu, A. Feldhoff, Transmission electron microscopy study of $Ba_{0.5}Sr_{0.5}Co_{0.8}Fe_{0.2}O_{-\delta}$ perovskite decomposition at intermediate temperatures, Chemistry of Materials, 22 (2010) 5866-5875.

[96] M. Arnold, T.M. Gesing, J. Martynczuk, A. Feldhoff, Correlation of the formation and the decomposition process of the BSCF perovskite at intermediate temperatures, Chemistry of Materials, 20 (2008) 5851-5858.

[97] C. Niedrig, S. Taufall, M. Burriel, W. Menesklou, S.F. Wagner, S. Baumann, E. Ivers-Tiffée, Thermal stability of the cubic phase in $Ba_{0.5}Sr_{0.5}Co_{0.8}Fe_{0.2}O_{3-\delta}$ (BSCF)1, Solid State Ionics, 197 (2011) 25-31.

[98] S Švarcová, K Wiik, olc hard, M ouwmeester, Grande, Structural instability of cubic perovskite $Ba_xSr_{1-x}Co_{1-y}Fe_yO_{3-\delta}$, Solid State Ionics, 178 (2008) 1787-1791.

[99] P. Müller, H. Störmer, L. Dieterle, C. Niedrig, E. Ivers-Tiffée, D. Gerthsen, Decomposition pathway of cubic $Ba_{0.5}Sr_{0.5}Co_{0.8}Fe_{0.2}O_{3-\delta}$ between 700 °C and 1000 °C analyzed by electron microscopic techniques, Solid State Ionics, 206 (2012) 57-66.

[100] L.W. Tai, M.M. Nasrallah, H.U. Anderson, D.M. Sparlin, S.R. Sehlin, Structure and electrical properties of $La_{-x}Sr_xCo_{-y}Fe_yO_3$, Part 1. The system $La_{0.8}Sr_{0.2}Co_{-y}Fe_yO_3$, Solid State Ionics, 76 (1995) 259-271.

[101] Y. Teraoka, H.-M. Zhang, S. Furukawa, N. Yamazoe, Oxygen permeation through perovskite-type oxides, Chemistry Letters, 14 (1985) 1743-1746.

[102] N. Miura, H. Murae, H. Kusaba, J. Tamaki, G. Sakai, N. Yamazoe, Oxygen permeability and phase transformation of $Sr_{0.9}Ca_{0.1}CoO_{\delta}$, Journal of the Electrochemical Society, 146 (1999) 2581-2586.

[103] Y. Teraoka, H.-M. Zhang, N. Yamazoe, Oxygen-sorptive properties of defect perovskite-type $La_{1-x}Sr_xCo_{1-y}Fe_yO_{3-\delta}$, Chemistry Letters, 14 (1985) 1367-1370.

[104] S. Pei, M.S. Kleefisch, T.P. Kobylinski, J. Faber, C.A. Udovich, V. Zhang-McCoy, B. Dabrowski, U. Balachandran, R.L. Mieville, R.B. Poeppel, Failure mechanisms of ceramic membrane reactors in partial oxidation of methane to synthesis gas, Catalysis Letters, 30 (1994) 201-212.

[105] M.A. Alaee, Effect of Ba content on oxygen permeation performance of $Ba_xSr_{-x}Co_{0.8}Fe_{0.2}O_{3-\delta}$ (x = 0.2, 0.5, and 0.8) perovskite-type membrane, Journal of chemical & engineering, 54 (2009) 3082-3091.

[106] S. Wang, M. Katsuki, M. Dokiya, T. Hashimoto, High temperature properties of $La_{0.6}Sr_{0.4}Co_{0.8}Fe_{0.2}O_{-\delta}$ phase structure and electrical conductivity, Solid State Ionics, 159 (2003) 71-78.

[107] Z. Shao, S.M. Haile, A high-performance cathode for the next generation of solid-oxide fuel cells, Nature, 431 (2004) 170-173.

[108] T. Ishigaki, S. Yamauchi, K. Kishio, J. Mizusaki, K. Fueki, Diffusion of oxide ion vacancies in perovskite-type oxides, Journal of Solid State Chemistry, 73 (1988) 179-187.

[109] A. Yan, M. Yang, Z. Hou, Y. Dong, M. Cheng, Investigation of $Ba_{1-x}Sr_xCo_{0.8}Fe_{0.2}O_{-\delta}$ as cathodes for low-temperature solid oxide fuel cells both in the absence and presence of CO_2, Journal of Power Sources, 185 (2008) 76-84.

[110] L. Tan, X. Gu, L. Yang, L. Zhang, C. Wang, N. Xu, Influence of sintering

condition on crystal structure, microstructure, and oxygen permeability of perovskite-related type $Ba_{0.8}Sr_{0.2}Co_{0.8}Fe_{0.2}O_{-\delta}$ membranes, Separation and Purification Technology, 32 (2003) 307-312.

[111] H. Lu, J. Tong, Z. Deng, Y. Cong, W. Yang, Crystal structure, oxygen permeability and stability of $Ba_{0.5}Sr_{0.5}Co_{0.8}Fe_{0.1}M_{0.1}O_{-\delta}$ (M = Fe, Cr, Mn, Zr) oxygen-permeable membranes, Materials Research Bulletin, 41 (2006) 683-689.

[112] D.W. Kim, D.S. Kim, Y.G. Kim, Y.C. Kim, S.G. Oh, Preparation of hard agglomerates free and weakly agglomerated antimony doped tin oxide (ATO) nanoparticles by coprecipitation reaction in methanol reaction medium, Materials Chemistry and Physics, 97 (2006) 452-457.

[113] A. Waindich, M. Müller, Corrosion of $Ba_{1-x}Sr_xCo_{1-y}Fe_yO_{3-\delta}$ and $La_{0.3}Ba_{0.7}Co_{0.2}Fe_{0.8}O_{3-\delta}$ materials for oxygen separating membranes under oxycoal conditions, Journal of Membrane Science, 337 (2009) 182-187.

[114] S.A. Möbius, Charakterisierung perowskitischer Hochtemperaturmembranen zur Sauerstoffbereitstellung für fossil gefeuerte Kraftwerksprozesse, Dissertation, Jülich: Zentralbibliothek, Forschungszentrum Jülich GmbH, 2010.

[115] S. Kato, M. Ogasawara, M. Sugai, S. Nakata, Crystal structure and property of perovskite-type oxides containing ion vacancy, Catalysis Surveys from Asia, 8 (2004) 27-34.

[116] Z. Yang, A.S. Harvey, A. Infortuna, L.J. Gauckler, Phase relations in the Ba-Sr-Co-Fe-O system at 1273 K in air, Journal of Applied Crystallography, 42 (2009) 153-160.

[117] M. Mogensen, D. Lybye, N. Bonanos, P.V. Hendriksen, F.W. Poulsen, Factors controlling the oxide ion conductivity of fluorite and perovskite structured oxides, Solid State Ionics, 174 (2004) 279-286.

[118] S. Diethelm, J. van Herle, J. Sfeir, P. Buffat, Influence of microstructure on oxygen transport in perovskite type membranes, British Ceramic Transactions, 103 (2004) 147-152.

[119] V.V. Kharton, F.M.B. Marques, Mixed ionic-electronic conductors: Effects of ceramic microstructure on transport properties, Current Opinion in Solid State and Materials Science, 6 (2002) 261-269.

[120] J. Martynczuk, M. Arnold, A. Feldhoff, Influence of grain size on the oxygen permeation performance of perovskite-type $(Ba_{0.5}Sr_{0.5})(Fe_{0.8}Zn_{0.2})O_{-\delta}$ membranes, Journal of Membrane Science, 322 (2008) 375-382.

[121] M. Salehi, F. Clemens, E.M. Pfaff, S. Diethelm, C. Leach, T. Graule, B. Grobéty, A case study of the effect of grain size on the oxygen permeation flux of BSCF disk-shaped membrane fabricated by thermoplastic processing, Journal of Membrane Science, 382 (2011) 186-193.

[122] W. Schatt, Sintervorgänge—Grundlagen, Springer-Verlag GmbH, 1992.

[123] A. Möbius, D. Henriques, T. Markus, Sintering behaviour of $La_{-x}Sr_xCo_{0.2}Fe_{0.8}O_{-\delta}$ $(0.3 \leq x \leq 0.8)$ mixed conducting materials, Journal of the European Ceramic Society, 29 (2009) 2831-2839.

[124] A. Mosadeghkhah, M.A. Alaee, T. Mohammadi, Effect of sintering temperature and dwell time and pressing pressure on $Ba_{0.5}Sr_{0.5}Co_{0.8}Fe_{0.2}O_{-\delta}$ perovskite-type membranes, Materials & Design, 28 (2007) 1699-1706.

[125] L. Tan, X. Gu, L. Yang, W. Jin, L. Zhang, N. Xu, Influence of powder synthesis methods on microstructure and oxygen permeation performance of $Ba_{0.5}Sr_{0.5}Co_{0.8}Fe_{0.2}O_{-\delta}$ perovskite-type membranes, Journal of Membrane Science, 212 (2003) 157-165.

[126] M. Arnold, J. Martynczuk, K. Efimov, H. Wang, A. Feldhoff, Grain boundaries

as barrier for oxygen transport in perovskite-type membranes, Journal of Membrane Science, 316 (2008) 137-144.

[127] S. Baumann, F. Schulze-Küppers, S. Roitsch, M. Betz, M. Zwick, E.M. Pfaff, W.A. Meulenberg, J. Mayer, D. Stöver, Influence of sintering conditions on microstructure and oxygen permeation of $Ba_{0.5}Sr_{0.5}Co_{0.8}Fe_{0.2}O_{-\delta}$ (BSCF) oxygen transport membranes, Journal of Membrane Science, 359 (2010) 102-109.

[128] Jae-II. Jung, S.T. Misture, D.D. Edwards, Oxygen stoichiometry, electrical conductivity, and thermopower measurements of BSCF ($Ba_{0.5}Sr_{0.5}Co_xFe_{1-x}O_{3-\delta}$, $0 \le x \le 0.8$) in air, Solid State Ionics, 181 (2010) 1287-1293.

[129] Z. Qingshan, J. Tongan, W. Yong, Thermal expansion behavior and chemical compatibility of $Ba_xSr_{-x}Co_{-y}Fe_yO_{-\delta}$ with 8YSZ and 20GDC, Solid State Ionics, 177 (2006) 1199-1204.

[130] W.K. Hong, G.M. Choi, Oxygen permeation of BSCF membrane with varying thickness and surface coating, Journal of Membrane Science, 346 (2010) 353-360.

[131] D.N. Mueller, R.A. De Souza, T.E. Weirich, D. Roehrens, J. Mayer, M. Martin, A kinetic study of the decomposition of the cubic perovskite-type oxide $Ba_xSr_{1-x}Co_{0.8}Fe_{0.2}O_{3-\delta}$ (BSCF) ($x = 0.1$ and 0.5), Physical Chemistry Chemical Physics, 12 (2010) 10320-10328.

[132] R. Kriegel, N. Preu, Dilatometric determination of phase transition temperatures and oxidation temperatures on the compounds $SrMnO_{-y}$ and Sr_2MnO_{-y}, Thermochimica Acta, 285 (1996) 91-98.

[133] M. Yoshiya, C.A.J. Fisher, Y. Iwamoto, M. Asanuma, J. Ishii, K. Yabuta, Phase stability of $BaCo_{-y}Fe_yO_{-\delta}$ by first principles calculations, Solid State Ionics, 172 (2004) 159-163.

[134] F. Liang, H. Jiang, H. Luo, J. Caro, A. Feldhoff, Phase stability and permeation behavior of a dead-end $Ba_{0.5}Sr_{0.5}Co_{0.8}Fe_{0.2}O_{3-\delta}$ tube membrane in high-purity oxygen production, Chemistry of Materials, 23 (2011) 4765-4772.

[135] P. Muller, L. Dieterle, E. Muller, H. Stormer, D. Gerthsen, C. Niedrig, S. Taufall, S.F. Wagner, E. Ivers-Tiffee, $Ba_{0.5}Sr_{0.5}Co_{0.8}Fe_{0.2}O_{3-\delta}$ for oxygen separation membranes, ECS Transactions, 28 (2010) 309-314.

[136] Z. Chen, Z. Shao, R. Ran, W. Zhou, P. Zeng, S. Liu, A dense oxygen separation membrane with a layered morphologic structure, Journal of Membrane Science, 300 (2007) 182-190.

[137] M. Rebeilleau-Dassonneville, S. Rosini, A.C. v. Veen, D. Farrusseng, C. Mirodatos, Oxidative activation of ethane on catalytic modified dense ionic oxygen conducting membranes, Catalysis Today, 104 (2005) 131-137.

[138] W.A. Johnson, R.F. Mehl, Reaction kinetics in processes of nucleation and growth, American Institute of Mining and Metallurgical Engineers Transactions, 135 (1939) 416-442.

[139] J.W. Christian, Chapter 12—Formal theory of transformation kinetics, in: The Theory of Transformations in Metals and Alloys, Pergamon, Oxford, 2002, pp. 529-552.

[140] H.J.M. Bouwmeester, Dense ceramic membranes for methane conversion, Catalysis Today, 82 (2003) 141-150.

[141] W. Geir, Determination of oxygen transport coefficients in perovskites and perovskite related materials with mixed conductivity, Dissertation, Trondheim Norway: Norwegian University of Science and Technology, 2005.

[142] Y. Teraoka, T. Nabunaga, N. Yamazoe, Effect of cation substitution on the

oxygen semipermeability of perovskite-type oxides, Chemistry Letters, 17 (1988) 503-506.

[143] A. Ghadimi, M.A. Alaee, A. Behrouzifar, A.A. Asadi, T. Mohammadi, Oxygen permeation of $Ba_xSr_{1-x}Co_{0.8}Fe_{0.2}O_{3-\delta}$ perovskite-type membrane: Experimental and modeling, Desalination, 270 (2011) 64-75.

[144] Z. Yang, Y.S. Lin, A semi-empirical equation for oxygen nonstoichiometry of perovskite-type ceramics, Solid State Ionics, 150 (2002) 245-254.

[145] Q. Jiang, K.J. Nordheden, S.M. Stagg-Williams, Oxygen permeation study and improvement of $Ba_{0.5}Sr_{0.5}Co_{0.8}Fe_{0.2}O_x$ perovskite ceramic membranes, Journal of Membrane Science, 369 (2011) 174-181.

[146] C. Wagner, Equations for transport in solid oxides and sulfides of transition metals, Progress in Solid State Chemistry, 10 (1975) 3-16.

[147] Z. Yang, A.S. Harvey, L.J. Gauckler, Influence of CO_2 on $Ba_{0.2}Sr_{0.8}Co_{0.8}Fe_{0.2}O_{-\delta}$ at elevated temperatures, Scripta Materialia, 61 (2009) 1083-1086.

[148] A. Yan, V. Maragou, A. Arico, M. Cheng, P. Tsiakaras, Investigation of a $Ba_{0.5}Sr_{0.5}Co_{0.8}Fe_{0.2}O_{-\delta}$ based cathode SOFC: II. The effect of CO_2 on the chemical stability, Applied Catalysis B: Environmental, 76 (2007) 320-327.

[149] Z.-X. Cai, Y. Zhu, Dislocation-assisted-diffusion model for the kinetics of bismuth cuprate 2212-to-2223 transformation, Applied Superconductivity, IEEE Transactions on, 9 (1999) 2714-2717.

[150] M. Arnold, H. Wang, J. Martynczuk, A. Feldhoff, In situ study of the reaction sequence in the sol–gel synthesis of a $(Ba_{0.5}Sr_{0.5})(Co_{0.8}Fe_{0.2})O_{-\delta}$ perovskite by X-ray diffraction and transmission electron microscopy, Journal of the American Ceramic Society, 90 (2007) 3651-3655.

[151] T. Negas, R.S. Roth, The system $SrMnO_{-x}$, Journal of Solid State Chemistry, 1 (1970) 409-418.

[152] R. Søndenå, S. Stølen, P. Ravindran, T. Grande, N.L. Allan, Corner-versus face-sharing octahedra in $AMnO_3$ perovskites (A = Ca, Sr, and Ba), Physical Review B, 75 (2007) 184105.

[153] M. Arnold, Q. Xu, F.D. Tichelaar, A. Feldhoff, Local charge disproportion in a high-performance perovskite, Chemistry of Materials, 21 (2009) 635-640.

Symbol index

Latin symbols

a	Å	Lattice parameter
A	cm^2	effective membrane area
b	Å	Lattice parameter
c	Å	Lattice parameter
, feed/sweep	%	oxygen concentration in the feed/permeate gas
, feed/sweep	%	nitrogen concentration in the feed/permeate gas
	mol·cm^{-3}	oxygen vacancy concentration
d	mm	sample diameter
D^*	cm^{2}s $^{-1}$	tracer diffusion coefficient
D_i	cm^{2}s $^{-1}$	self-diffusion coefficient of oxygen ions
D_v	cm^{2}s $^{-1}$	diffusion coefficient of oxygen vacancy
E_v	eV	formation energy of oxygen vacancy
f_O	-	Octahedral factor
h	mm	membrane thickness
$_e$	mol·cm^{-2}s $^{-1}$	flux density of electrons
$_{ex}$	mol·cm^{-2}s $^{-1}$	exchange flux density on the membrane surface in the absence of oxygen partial pressure gradient
$_h$	mol·cm^{-2}s $^{-1}$	flux density of electron holes
$_i$	mol·cm^{-2}s $^{-1}$	flux of single component i
	ml·cm^{-2}·min^{-1}	oxygen permeation flux through the membrane
	mol·cm^{-2}s $^{-1}$	flux density of oxygen vacancy
$_{permeate}$	ml·min^{-1}	flow of the permeate gas
k	h^{-n}	the rate constant for decomposition process
L	mm	membrane thickness
L_0	m	sample initial length
$_c$	m	characteristic membrane thickness
( )	m	sample length

$_{rel}$	-	the relative change of the sample length
$m_{S\ ,}$	g	sample weight at room temperature
m	g	sample mass at temperature T
M_S	g	molar mass of BSCF material
M	g	molar mass of oxygen
n	-	Avrami exponent for decomposition process
pO_2	bar	oxygen partial pressure
$p'O_2$	bar	oxygen partial pressure at the feed side
$p''O_2$	bar	oxygen partial pressure at the permeate side
r_a	Å	the size of anion
r_c	Å	the size of cation
r_A	Å	the ionic radii of A-site cations
r_B	Å	the ionic radii of B-site cations
r_O	Å	the ionic radii of oxygen ion
T	℃	temperature
$T_{inflection}$	℃	temperature corresponding to the inflection point in thermochemical expansion curve
$T_{min,1}$	℃	temperature corresponding to the first minimal value of shrinkage rate
$T_{min,2}$	℃	temperature corresponding to the second minimal value of shrinkage rate
T_{onset}	℃	onset temperature for the occurrence of shrinkage state
V_m	Å^3	molar volume of perovskite
x	-	molar fraction of A-site cations
y	-	molar fraction of B-site cations
z_i	-	charger number of single component i

Greek symbols

$\alpha_{hex}(t)$	%	volume fraction of the hexagonal phase in membrane at time t
$\alpha_{hex}(t\quad)$	%	equilibrium hexagonal phase fraction
α	K^{-1}	thermochemical expansion coefficient
	-	chemical expansion coefficient

δ	-	oxygen nonstoichiometry
δ	-	variation of oxygen nonstoichiometry
ε_{total}	%	total shrinkage occurring in the sintered sample
ε( )	%	linear shrinkage of sample
dε( )/dt	$\% \cdot h^{-1}$	shrinkage rate
η_i	$J \cdot mol^{-1}$	electrochemical potential of single component i
	$J \cdot mol^{-1}$	chemical potential
$_{theo}$	$g \cdot cm^{-3}$	theoretical density
$_{e}$	$S \cdot m^{-1}$	conductivity of electrons
$_{i}$	$S \cdot m^{-1}$	conductivity of the single charge carrier i
$_{ion}$	$S \cdot m^{-1}$	conductivity of ions
	$S \cdot m^{-1}$	conductivity of oxygen ions
τ	-	Goldschmidt tolerance factor
	$J \cdot mol^{-1}$	electronic potential

Abbreviations

ASU	Air separation unit
BSCF	$Ba_xSr_{1-x}Co_yFe_{1-y}O_{3-\delta}$
CCS	Carbon capture and storage
CMC	Carboxymethyl cellulose
DTA	Differential thermal analysis
EBSD	Electron backscatter diffraction analysis
EDX	Energy-dispersive X-ray spectroscopy
GC	Gas chromatograph
ICP-OES	Inductively coupled plasma optical emission spectrometer
IGCC	Intergrated gasification combined cycle
IT	Intermediate temperature
JMA	Johnson-Mehl-Avrami
LSCF	$(La,Sr)(Co,Fe)O_{3-\delta}$
MEA	Monoethanolamine
MIEC	Mixed ionic and electronic conducting
OTM	Oxygen transport membrane
PCC	Post-combustion capture

RT	Room temperature
SCF	$SrCo_yFe_{1-y}O_{3-\delta}$
SEM	Scanning electron microscope
TEC	Thermal expansion coefficient
TGA	Thermogravimetric analysis
TMA	Thermomechanical analysis
XRD	X-ray diffraction

Constants

$F = 96485.3415$	$C\cdot mol^{-1}$	Faraday constant
$N_A = 6.02214\cdot 10^{23}$	mol^{-1}	Avogadro's constant
$R = 8.31446$	$J\cdot K^{-1}\cdot mol^{-1}$	Gas constant

Figure index

Table index

Appendix

A Raw materials and calcination parameters for powder production

The raw materials and calcination parameters (calcination temperature $T_{cal.}$ and overall dwell time $t_{cal.}$) for BSCF perovskite production are summarized in **Tab. A.1**. The heating rate for powder calcination is 10 K/min and the cooling rate is 5 K/min. The calcination temperature for each stoichiometric powder mixture was determined by the normalized DTA/TG curves, as shown in **Fig. A.1**.

Tab. A.1 Raw materials and calcination parameters for BSCF powder production

Materials	Raw materials	$T_{cal.}$ / ℃	$t_{cal.}$ / h
BSCF2828	$BaCO_3$, $SrCO_3$, $CoCO_3$, Fe_2O_3	1150	42
BSCF4628	$BaCO_3$, $SrCO_3$, $CoCO_3$, Fe_2O_3	1150	42
BSCF5528	$BaCO_3$, $SrCO_3$, $CoCO_3$, Fe_2O_3	1150	54
BSCF6428	$BaCO_3$, $SrCO_3$, $CoCO_3$, Fe_2O_3	1150	54
BSCF7328	$BaCO_3$, $SrCO_3$, $CoCO_3$, Fe_2O_3	1150	54
BSCF2882	$BaCO_3$, $SrCO_3$, $CoCO_3$, Fe_2O_3	1150	60
BSCF4682	$BaCO_3$, $SrCO_3$, $CoCO_3$, Fe_2O_3	1150	24
BSCF5582*	as-received	as-received	as-received
BSCF6482	$BaCO_3$, $SrCO_3$, $CoCO_3$, Fe_2O_3	1150	24
BSCF7382	$BaCO_3$, $SrCO_3$, $CoCO_3$, Fe_2O_3	1140	36

*BSCF5582 powder was provided by Treibacher Industrie AG, Austria.

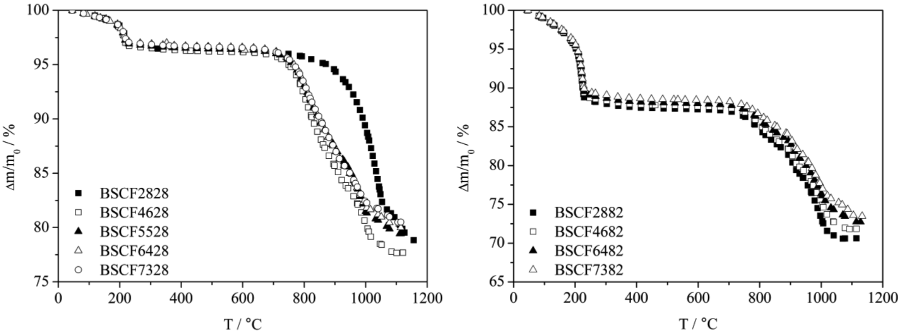

Fig. A.1 Determination of the calcination temperature for raw powder mixtures by normalized DTA/TG curves.

B Pressing steps for pellets/membranes production

In **Tab. B.1**, the load forces and dwell time of each pressing step for $Ba_xSr_{1-x}Co_yFe_{1-y}O_{3-\delta}$ pellets/membranes production (except BSCF5582) are presented.

Tab. B.1 Uni-axial pressing steps for the production of green disks of membranes/pellets

Shapes	Load forces / kN	Dwelling time / min
Membrane (d = 20 mm)	2	0.5
	6	0.5
	17	0.5
	28	0.5
	39	10
Pellet (d = 8 mm)	2	0.5
	4	0.5
	6	10

C Melting temperature determination

The melting temperature (T_m) of calcined and wet-milled BSCF powders used in this study was determined by means of DTA. The onset point of the endothermal melting peak in the measured DTA curve represents the melting point of BSCF. The obtained DTA signals for the determination of the melting point of BSCF materials are illustrated in **Fig. C.1**. The measured melting temperatures of BSCF are summarized in **Tab. C.1**.

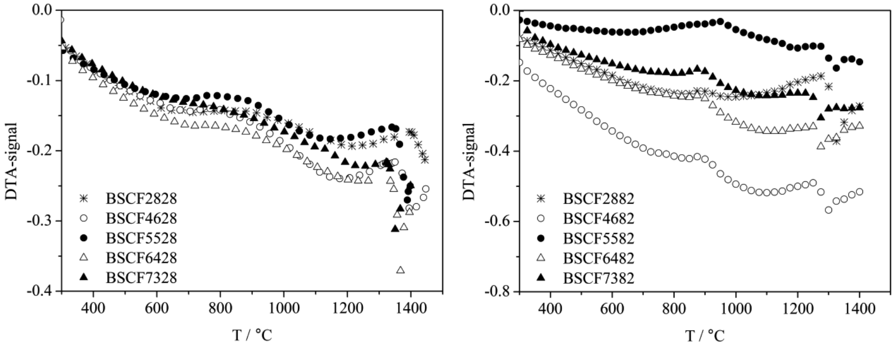

Fig. C.1 DTA curves of the BSCF materials measured for the determination of melting points

Tab. C.1 Melting temperatures of the BSCF powders

Materials	T_m	Materials	T_m
BSCF2828	~1403 °C	BSCF2882	~1278 °C
BSCF4628	~1351 °C	BSCF4682	~1260 °C
BSCF5528	~1342 °C	BSCF5582	~1259 °C
BSCF6428	~1330 ℃	BSCF6482	~1246 °C
BSCF7328	~1320 °C	BSCF7382	~1241 °C

D Data of the ions in BSCF materials

The effective ionic radii (IR), along with the coordination number (CN), molar mass (M_i), valence (z_i) and spin state (SP) of ions in BSCF are presented in **Tab. D.1** according to the data in [68].

Tab. D.1 Valency state, spin state, effective ionic radii, coordination number, molar mass of the elements in BSCF

Elements	z_i / -	SP / -	IR / Å	CN / -	M_i / g/mol
Barium	+2	-	1.61	12	137.327
Strontium	+2	-	1.44	12	87.62
Cobalt	+2	HS	0.745	6	58.933
Cobalt	+3	LS	0.545	6	58.933
Cobalt	+3	HS	0.61	6	58.933
Cobalt	+4	HS	0.53	6	58.933
Iron	+2	HS	0.780	6	55.845
Iron	+3	LS	0.55	6	55.845
Iron	+3	HS	0.645	6	55.845
Iron	+4	HS	0.585	6	55.845
Oxygen	-2	-	1.40	6	15.999

E D X analysis of the 2 0 mm-thick BSCF6482 membrane after 2000 h permeation at 8 0 °C under the air/He pressure gradient

Fig. E.1 shows the SEM micrograph and local EDX analysis of the BSCF6482 membrane after permeation measurement at 850 °C for 2000 h. A small amount of barium sulfate particles were observed in this microstructure. The reason for the existence of this secondary phase might be caused by the impurities in the raw powder ($BaCO_3$) used for membrane production.

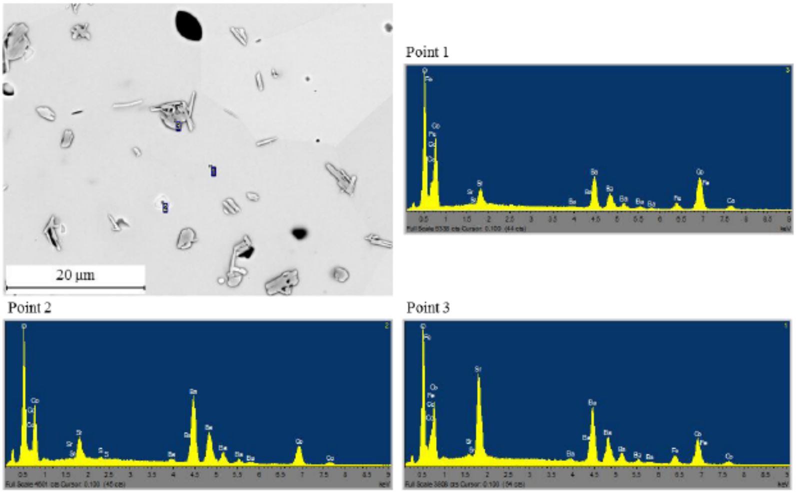

Fig. E.1 SEM micrograph and EDX results of the cross sections of the BSCF6482 membrane after long-term permeation at 850 °C for 2000 h under the air/He pressure gradient

F Linescans of the 2 mm-thick BSCF4682 membrane after 2000 h permeation at 800 °C under the air/He pressure gradient

The chemical composition of the plate-shaped secondary phases in BSCF4682 was characterised by linescans through the microstructure at the permeate side of the membrane after long-term permeation measurement at 800 °C for 2000 h under the air/He pressure gradient. From **Fig. F.1**, the plate-shaped secondary phase should be cobalt-enriched oxides which were formed due to kinetic demixing of the BSCF perovskite.

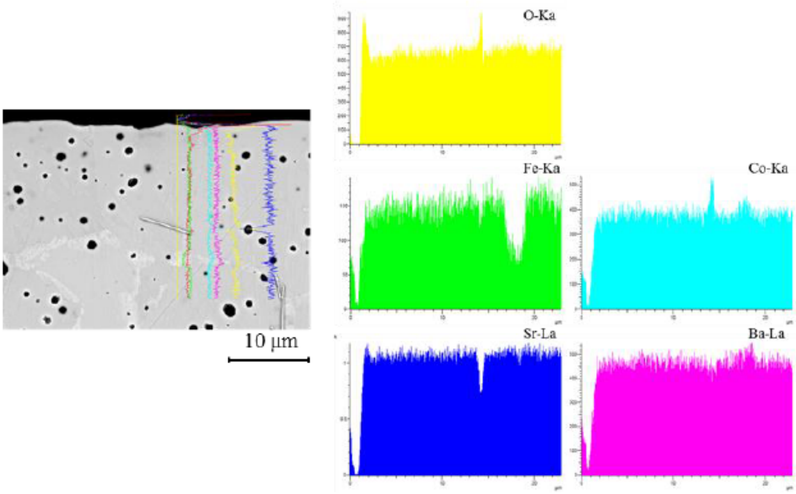

Fig. F.1 Elemental distributions along the cross section of sweep side of the BSCF4682 membrane after long-term permeation at 800 °C for 2000 h under the air/He pressure gradient

G SEM and EDX analysis of the secondary phases in the BSCF6482 membrane after long-term and cyclic permeation measurement

Fig. G.1 displays the microstructures of the 2.0 mm-thick BSCF6482 membrane after long-term and cyclic permeation test in the temperature range of 700-900 °C under the air/He pressure gradient. Various complex secondary phases could be observed at both sides of the membrane after the measurement. In the microstructure of feed side of the membrane, the initial cubic perovskite decomposes into at least four components: a cobalt-enriched phase, a mixture of barium carbonate and sulfate, a barium-enriched phase with complete depletion of iron as well as the cubic matrix. At the permeate side of the membrane, less severe decay of the microstructure was observed in contrast to that at the feed side. Similar to the secondary phases found at the other side of membrane, the microstructure of the sweep side consists of a cobalt-enriched phase, barium carbonate and sulfate as well as the perovskite matrix.

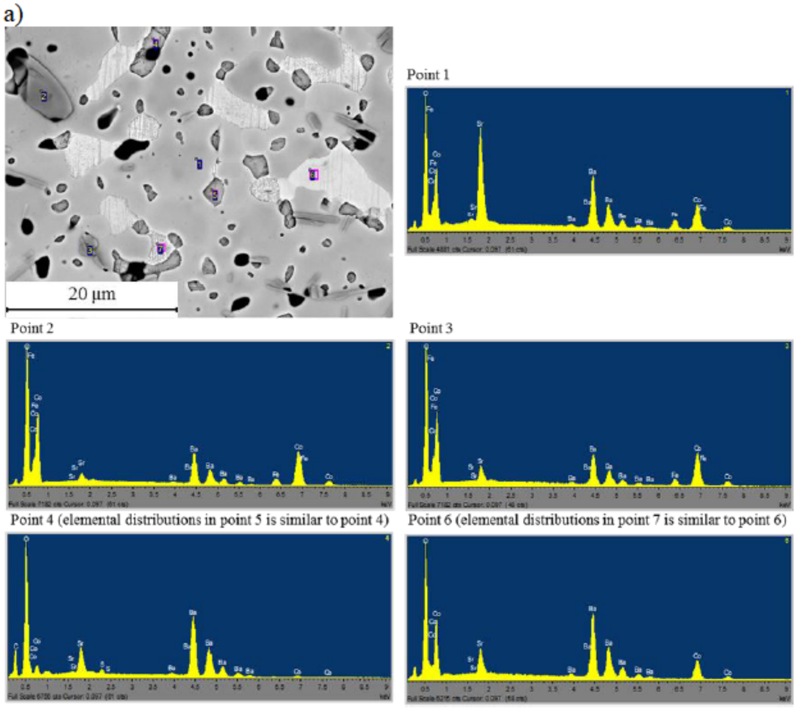

Point 1

Point 2

Point 3

Point 4 (elemental distributions in point 5 is similar to point 4)

Point 6 (elemental distributions in point 7 is similar to point 6)

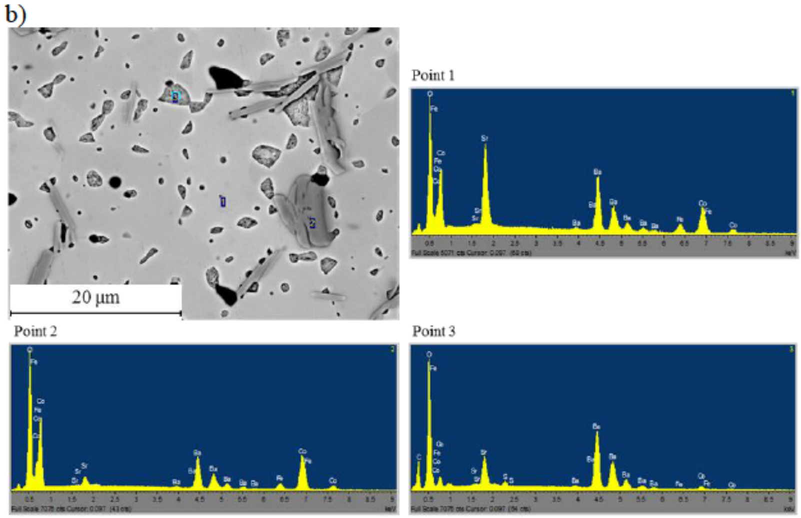

Fig. G.1 SEM micrographs and EDX results of cross sections at a) the feed side and b) the sweep side of the BSCF6482 membrane after long-term permeation at 800 °C for 2000 h followed by a cyclic permeation test in the temperature range of 700-900 °C under the air/He pressure gradient

Acknowledgements

I would like to express my gratitude to Univ-Prof. Dr.-Ing. Lorenz Singheiser for offering me this opportunity to work in IEK-2 on this interesting topic for my doctoral thesis.

I want to thank my direct supervisor Priv.-Doz. Dr.-Ing. Torsten Markus for his helpful guidance and kind suggestions on my work. I do appreciate those discussions about the scientific difficulties involved in the task during my three-years study.

My sincere thanks are given to my nice colleges Mr. David Henriques, Dr. Christos Chatzicharalampous, Dr. Annett Möbius for their great help and advices on my experiments.

I would like to thank Mr. Mikro Ziegner for his help on the XRD analysis. Many thanks are given to Dr. rer. nat.Egbert Wessel and Dr. Daniel Grüner for their help on the SEM analysis. I would like to acknowledge all the colleges involved in my doctoral thesis during the three years.

Special thanks to my lovely family and friends for their continuous support and encouragement through this thesis.

Band / Volume 182
Monazite-type Ceramics for Conditioning of Minor Actinides: Structural Characterization and Properties
C. Babelot (2013), x, 127 pp
ISBN: 978-3-89336-889-1

Band / Volume 183
High-rate growth of hydrogenated amorphous and microcrystalline silicon for thin-film silicon solar cells using dynamic very-high frequency plasma-enhanced chemical vapor deposition
T. Zimmermann (2013), x, 126 pp
ISBN: 978-3-89336-892-1

Band / Volume 184
IEK-3 Report 2013. Durable Electrochemical Process Engineering
(2013), ca. 180 pp
ISBN: 978-3-89336-893-8

Band / Volume 185
Light Trapping with Plasmonic Back Contacts in Thin-Film Silicon Solar Cells
U. W. Paetzold (2013), X, 175 pp
ISBN: 978-3-89336-895-2

Band / Volume 186
Plant-plant interactions, biodiversity & assembly in grasslands and their relevance to restoration
V. M. Temperton (2013), ca 420 pp
ISBN: 978-3-89336-896-9

Band / Volume 187
Ab initio investigation of ground-states and ionic motion in particular in zirconia-based solid-oxide electrolytes
J. A. Hirschfeld (2013), v, 144 pp
ISBN: 978-3-89336-897-6

Band / Volume 188
Entwicklung protonenleitender Werkstoffe und Membranen auf Basis von Lanthan-Wolframat für die Wasserstoffabtrennung aus Gasgemischen
J. Seeger (2013), V, 130 pp
ISBN: 978-3-89336-903-4

Band / Volume 189
Entwicklung und Herstellung von metallgestützten Festelektrolyt-Brennstoffzellen (MSC-SOFC) mit einem Sol-Gel-Elektrolyten
S. D. Vieweger (2013), xviii, 176 pp
ISBN: 978-3-89336-904-1

Band / Volume 190
Mobile Brenngaserzeugungssysteme mit Mitteldestillaten für Hochtemperatur-PEFC
C. Wiethege (2013), iii, 179 pp
ISBN: 978-3-89336-905-8

Band / Volume 191
Verbundvorhaben Öko-effiziente Flugzeugsysteme für die nächste Generation (EFFESYS) - Teilprojekt Brennstoffzelle, Infrastruktur, Komponenten und System (BRINKS) – Schlussbericht
J. Pasel, R.C. Samsun, H. Janßen, W. Lehnert, R. Peters, D. Stolten (2013), xii, 152 pp
ISBN: 978-3-89336-908-9

Band / Volume 192
Analyse des Betriebsverhaltens von Hochtemperatur-Polymerelektrolyt-Brennstoffzellen
L. Lüke (2013), 156 pp
ISBN: 978-3-89336-909-6

Band / Volume 193
Full-waveform inversion of crosshole GPR data for hydrogeological applications
A. Klotzsche (2013), X, 164 pp
ISBN: 978-3-89336-915-7

Band / Volume 194
Long Term Stability and Permeability of Mixed Ion Conducting Membranes under Oxyfuel Conditions
X. Li (2013), III, 143 pp
ISBN: 978-3-89336-916-4

Weitere ***Schriften des Verlags im Forschungszentrum Jülich*** unter
http://wwwzb1.fz-juelich.de/verlagextern1/index.asp

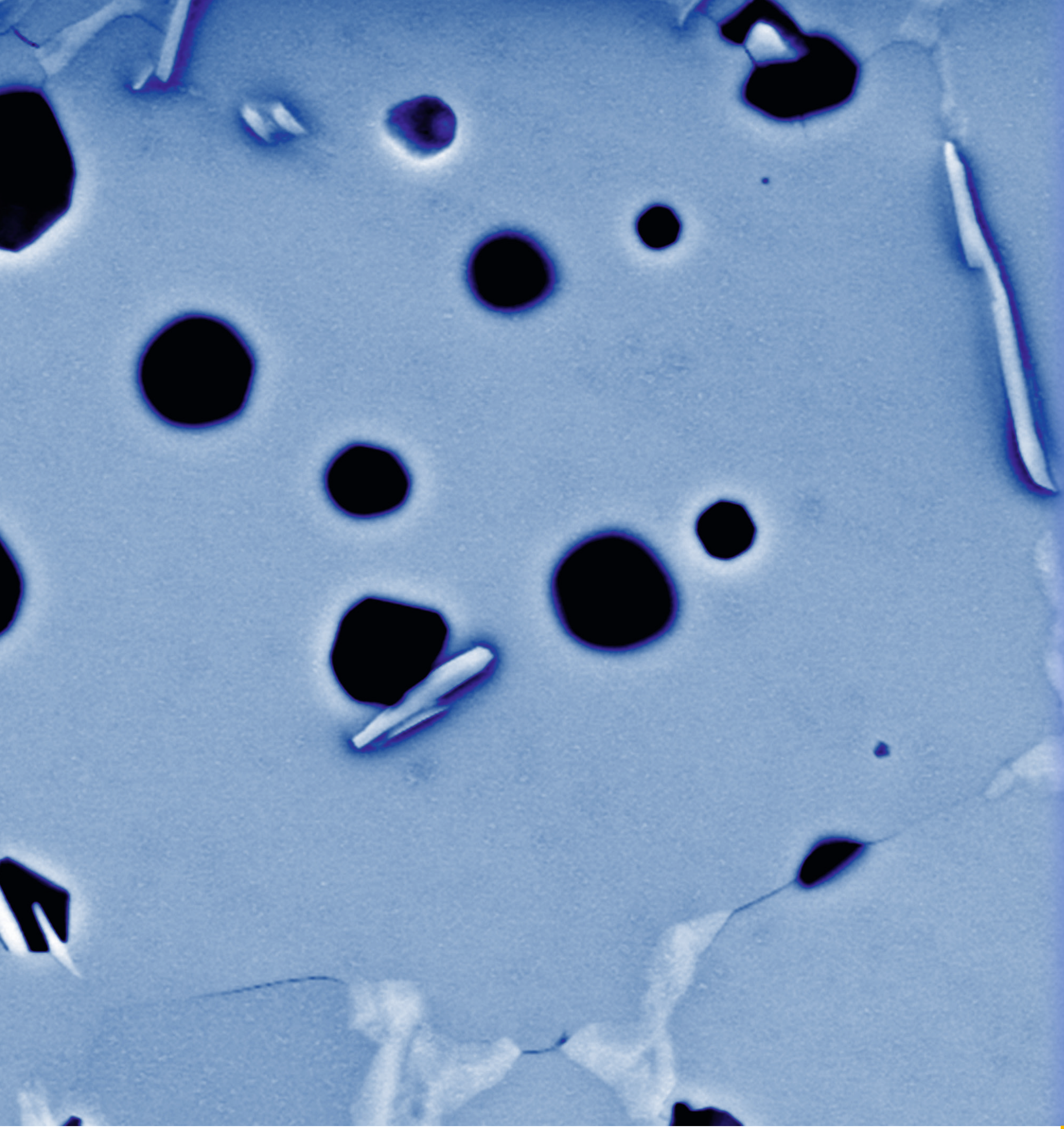

Energie & Umwelt / Energy & Environment
Band / Volume 194
ISBN 978-3-89336-916-4